

On the Mechanical Modeling, Visco-Elasticity and Application of Aerographite, a 3D Carbon Nano-Material

Dissertation

zur Erlangung des akademischen Grades
Doktor der Ingenieurwissenschaften
(Dr.-Ing.)
der Technischen Fakultät
der Christian-Albrechts-Universität zu Kiel

Arnim Schuchardt
Kiel
2014

1. Gutachter: Prof. Dr. Rainer Adelung
2. Gutachter: Prof. Dr. Franz Faupel
Datum der mündlichen Prüfung: 17.06.2015
Zum Druck genehmigt: 17.06.2015

Abstract

A three dimensional carbon network material of seamless interconnected and hollow tubes, featuring a graphitic structure and an extremely low density has been designed and fabricated in cm^3 volumes. The synthesis of this foam like material, named Aerographite, is based on highly-porous three dimensional networks from zinc oxide (ZnO) which are utilized as sacrificial templates in a chemical vapor deposition (CVD) process. Such type of ZnO templates are produced by the flame transport synthesis (FTS) and allow free control over the template pore size, porosity and structure sizes. By consequent minimization of the applied carbon masses and tailored template porosity of 97 %, the density of Aerographite was reduced to $180 \mu g/cm^3$ which had broken the record for lightest solid and remains up to date among the lightest materials in literature.

The challenge to measure the mechanical response of super light materials has been tackled by a self built mechanical test set-up for an automated cyclic stress strain measurement. Highest specific moduli of $E/\rho^2 = 0.46 \cdot 10^6 Pa/(kg/m^3)^2$ respectively $E/\rho^3 = 2.6 \cdot 10^6 Pa/(kg/m^3)^3$ under tensile stress has been revealed. The microscopic deformation mechanisms of Aerographite networks are identified by detailed in situ studies in the scanning electron microscope and an analytical model is established to interpret the elastic properties of the bulk Aerographite. Further, the visco elastic properties of Aerographite are discussed and based on the findings in the in situ experiments, a first theory for the visco-elastic mechanisms in Aerographite is introduced.

Finally the functional application of Aerographite as electrode material is demonstrated by the construction of two prototypes: an electrical double-layer capacitor equipped with Aerographite electrodes and a rechargeable lithium-sulfur battery with sulfur infiltrated Aerographite cathode. The capacity fading of the lithium-sulfur battery has been studied by cyclic voltammetry and the specific capacity of the electrical double-layer capacitor was measured.

Kurzfassung

In dieser Arbeit wird ein vollkommen neuartiges hoch poröses Kohlenstoffnetzwerkmaterial vorgestellt das aus nahtlos verbundenen, graphitischen Röhrchen von wenigen Mikrometern Durchmesser besteht. Die Synthese dieses hochporösen Graphitnetzwerks namens Aerographite basiert im wesentlichen auf einem hoch porösen dreidimensional vernetzen Opfertemplat aus Zinkoxid (ZnO) welches durch einen chemischen Gasphasen Abscheidungsprozess zu Aerographite umgewandelt wird. Dieser Prozess wurde in Kooperation mit der Technischen Universität Hamburg-Harburg eigens auf die Synthese von Aerographite angepasst und ermöglicht durch die Zufuhr von Wasserstoff das Entfernen des Zinkoxid Opfertemplates.

Die Synthese der ZnO Netzwerktemplate erfolgt durch die eigens entwickelte Flammensportsynthese welche es ermöglicht die Porengröße, die Porösität und den Vernetzungsgrad der ZnO Netzwerktemplate genau zu kontrollieren. Durch eine gezielte Verringerung der Kohlenstoffmenge und die Steigerung der Porösität der ZnO Netzwerktemplate auf 97% kann eine hierarchische Variante von Aerographite mit einer minimalen Dichte von $180 \mu g/cm^3$ synthetisiert werden. Dies macht Aerographite zu einem der leichtesten mikroporösen Festköpermateriale nach derzeitigem stand der Literatur.

Die mechanische Charakterisierung von Aerographite Netzwerken erfolgt in einem eigens für diesen Zweck konstruierten Mechanikmessstand für die automatisierte Messung von druck und zug-spannungs Zyklen. Die mikroskopischen Deformationsmechanismen der Aerographite Netzwerke werden in mechanischen in-situ Experimenten im Rasterelektronenmikroskop untersucht. Hierauf aufbauend wird ein analytisches Modell für die elastischen Eigenschaften von Aerographite hergeleitet und mit den mechanischen Messungen des Volumenmaterials verglichen. Basierend auf den Erkenntnissen aus den In-Situ Experimenten wird der intrinsische Mechanismus für die viskoelastischen Eigenschaften von Aerographite diskutiert.

Die funktionale Anwendung von Aerographite als Elektrodenmaterial wird anhand von zwei Prototypen demonstriert. Es wird der Prototyp eines Doppelschichtkondensators mit Aerographite Elektroden vorgestellt und eine Schwefelinfiltrierte Aerographite Kathode für einen Lithium-Schwefel Akkumulator präsentiert.

Contents

Introduction	1
I. Theory	5
1. Crystal Structure and Electrical Properties of Graphite	7
1.1. Crystal Structure	7
1.2. Electronic Structure and Conductivity	8
1.3. Glass-Like Carbon	9
2. Tetrapodal Zinc Oxide	11
3. Mechanical Aspects of Cellular Materials	15
3.1. The Young's Modulus-Density Chart	15
3.2. Bending- and Stretch-Dominated Networks	19
3.3. Modeling of Visco-Elastic Material Properties	22
3.4. Van der Waals Forces	26
4. Electrochemical Devices	29
4.1. Electrical Double-Layer Capacitor	29
4.2. Lithium-Sulfur Battery	31
II. Experimental	33
5. Synthesis of Aerographite	35
5.1. Flame Transport Synthesis of Zinc Oxide	35
5.2. Post Annealing of Zinc Oxide Tetrapod Networks	36
5.3. Conversion of Sacrificial Zinc Oxide Templates by Modified Chemical Vapor Deposition	38
6. Characterization Methods	43
6.1. Mechanical Characterization Setup	43
6.2. Mechanical In Situ Experiments of Aerographite	46
6.3. Electrical In Situ Experiments	48
7. Aerographite Electrodes	51
7.1. Electrical Double-Layer Capacitor with Aerographite Electrodes . . .	51

7.2. Lithium Battery with Sulfur Infiltrated Aerographite Cathode	52
III. Results and Discussion	55
8. Overview of the Basic Physical Properties of Aerographite	57
9. Microscopic Morphology and Structure of Aerographite	59
9.1. Aerographite Variants	59
9.2. Atomic Structure of Aerographite	62
10. Mechanical In Situ Experiments of Aerographite	67
10.1. In Situ Deflection of Individual Aerographite Tetrapod Arms	67
10.2. Elastic Model for Aerographite Networks	72
11. Mechanical Properties of Bulk Aerographite	83
11.1. Cyclic Stiffening of Aerographite	88
11.2. Visco-elastic Behavior of Aerographite	89
11.3. Model for the Visco-elastic Mechanisms in Aerographite	90
12. Electrical Properties of Aerographite	99
12.1. Electrical Conductivity of Aerographite Bulk Samples	99
12.2. Electrical In Situ Experiments at single Aerographite Structures . .	102
13. Aerographite Electrodes	105
13.1. Specific Surface Area of Aerographite	105
13.2. Electrical Double-Layer Capacitor with Aerographite Electrodes . .	106
13.3. Sulfur-infiltrated-Aerographite-Cathodes for Lithium Batteries . .	107
Conclusion and Outlook	111
Bibliography	115
Danksagung	123
List of Publications	125
Appendix	129
Eidesstattliche Erklärung	135

Introduction

The allotropy of carbon, particularly represented by variations in hybridization states and crystallographic symmetries, enables the development of functional materials with sophisticated morphologies including graphene [1], carbon nanotubes [2,3] (CNTs), carbon nanoscrolls [4, 5], fullerenes [6], aerogels [7] and nano-foams [8]. In a plethora of technical applications and fundamental researches, the strong relation between the morphology and the physical properties of the respective material has been proven [1, 9, 10]. A well known example for this fundamental relation between the atomic structure and physical properties is graphene which possesses a two dimensional (2D) planar honeycomb lattice of sp^2 hybridized carbon atoms and exhibits highest electrical conductivities due to its linear electronic dispersion relation [10, 11]. A one dimensional (1D) allotrope of carbon is represented by carbon nanotubes which show outstanding mechanical performance due to their structure. The walls of CNTs consist of a single or multiple layers of graphene and CNTs exhibit a tensile strength of up to 63 GPa [12] (multiwalled CNTs) and a Young's modulus in the terapascal (TPa) range [13–15].

However, the physical properties of these 1D and 2D structures are typically limited to the nano- and micro-scale which strongly inhibits the utilization in technical devices. For instance the tensile strength of carbon nanotubes is limited to 3 GPa [16] if they are assembled to a macroscopic rope [17–19] and the electrical conductivity of graphene is limited by the applied substrates [20]. The challenging aspect, is the utilization of these remarkable physical properties on a macroscopic scale namely in real life functional devices. Furthermore, for an improved integration, it is also advantageous to synthesize larger sample volumes. Normally this requires the assembly of 1D and 2D structures to larger three dimensional (3D) structures to

achieve space filling. This means, the synthesis of macroscopic 3D interconnected carbon nano materials is favorable because it enables the direct integration into devices.

Already a number of synthesis approaches for growth of macroscopic 3D carbon nano materials have recently been reported in literature [21–27]. However, almost all of these synthesis approaches are based on the wet chemical assembly of graphene oxide nano-flakes and subsequent freeze-drying. This method has a number of drawbacks and is typically limited to the synthesis of sheet like microstructures because of the utilized precursor materials. Another problem of this method is the subsequent removal of the solvent by a freeze-drying process step which can result in strong deformations of the grown 3D structure [24, 28]. Also other synthesis approaches by CVD growth of carbon on sacrificial nickel templates have been presented but were limited to commercially available nickel templates and not free standing without polymer backbone [29, 30]. For this reason it is necessary to develop new synthesis methods which allow the direct growth of 3D interconnected carbon nano materials instead of their assembly from microscopic 1D or 2D building units and enables the free control of their micro-structural morphology.

The major aim of this work was the development of a novel 3D carbon nano material with a highly porous network structure from hollow graphitic tubes called Aerographite [31]. This was achieved by a new synthesis method which is based on the chemical vapor deposition (CVD) of carbon on the surface of a highly porous sacrificial 3D network template from zinc oxide (ZnO). The ZnO network template is removed during the CVD process by the supply of hydrogen gas which enables the synthesis of a 3D network of hollow graphitic tubes. These tubes possess a micro-scale diameter and a nanoscopic thickness ($\approx 15\text{ nm}$) like thin multiwall carbon nanotubes (MWCNTs).

The required templates were produced by the so called flame transport synthesis (FTS). This method, for the growth of complex and interconnected 3D ZnO networks was developed in the group for Functional Nanomaterials at Kiel univer-

sity [32,33]. Due to their high porosity, open pore structure, mechanical stability and large volumes of up to 100 cm^3 these ZnO networks represent an ideal choice as template material.

In order to achieve the desired mechanical properties of bulk Aerographite, it was a major task to transfer the morphology of the ZnO templates to the completed Aerographite networks. A further aim was the synthesis of Aerographite variants with highest porosity respectively lowest density for the application as electrode material.

Beyond the synthesis, the mechanical properties of bulk Aerographite were of special interest. It was expected, that due to its unique morphology, Aerographite exhibits novel mechanical properties. Therefore it was the aim to identify the intrinsic deformation mechanisms of Aerographite by detailed *in situ* experiments and to derive a model for the description of the elastic properties of bulk Aerographite. With respect to the mechanical properties of highly porous Aerographite it was a further task to examine the relation between Young's modulus and density. This required the development of new experimental equipment to perform stress strain tests with the required accuracy.

In order to judge the applicability of Aerographite as electrode material, it was the aim to examine its utilization as cathode material, such as in a lithium-sulfur battery and in an electrical double-layer capacitor.

This thesis is composed of the following three parts: In Part I, the basic theoretical aspects, required for the discussion part, are introduced. In part II, the synthesis of Aerographite, the applied measurement methods are discussed. In part III, the experimental results are presented and discussed and an analytical model for the elastic properties of Aerographite is derived.

Part I.

Theory

1. Crystal Structure and Electrical Properties of Graphite

Aerographite consists of a network of microscopic tubes of carbon. For the most Aerographite variants the walls of these tubes possess a graphitic structure. In this chapter the crystal structure and the electronic structure of graphite are discussed.

1.1. Crystal Structure

The element carbon is allotropic and can occur as diamond, graphite, graphene or fullerene due to different hybridization states of s and p orbitals of the valence electrons of carbon, like the tetrahedral sp^3 hybridization in diamond or the trigonal sp^2 hybridization in graphite and graphene. As a result, diamond forms a three-dimensional covalently bonded crystal structure and graphite consists of hexagonal sp^2 hybridized layers of graphene. The carbon atoms in the graphene layers are covalently bonded (binding energy 4.3 eV) while the adjacent layers are held together by van der Waals forces (binding energy 70 meV) which is the reason for easy slide of the graphene sheets. The delocalized Π -orbitals lead to high electrical and thermal conductivity along the layers, respectively low conductivities perpendicular to the layers, resulting in a strong anisotropy of graphite. [34, 35] The stacking sequence of the hexagonal layers in graphite is ABA [36, 37] with an inter planar distance of 3.35 \AA to the adjacent layers. Within the layers the carbon atoms are arranged in a honeycomb lattice with an in-plane nearest neighbor distance of 1.42 \AA . The crystal structure can be described by a primitive hexagonal unit cell with the lattice constants $c = 6.71\text{ \AA}$ and $a = 2.46\text{ \AA}$ as illustrated in Figure 1.1. The crystal

structure belongs to the space group $P6_3/mmc$. Instead of the ABA stacking sequence, graphite can also occur in the stacking sequence ABC which results in a rhombohedral crystal structure [38–40].

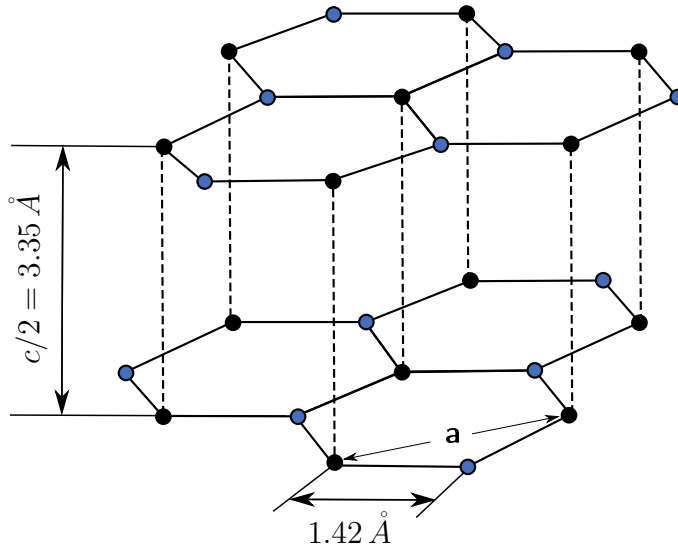


Figure 1.1: Schematic drawing of the crystal structure of graphite. The hexagonal layers exhibit the stacking sequence ABA with the lattice constants of $c = 6.71 \text{ \AA}$ and $a = 2.46 \text{ \AA}$. The carbon atoms which are indicated in black have neighbors directly above and below in the adjacent layers while the blue indicated carbon atoms have neighbors directly above and below in a distance of $c = 6.71 \text{ \AA}$.

1.2. Electronic Structure and Conductivity

The electron configuration of carbon is $1s^2 2s^2 2p^2$. In graphite, the $2s$, $2p_x$ and $2p_y$ electrons form three sp^2 hybrid orbitals which form σ -bonds. Perpendicular to the layers, the $2p_z$ electrons form delocalized Π orbitals which stabilize the in-plane bonding and contribute to the electrical and thermal conductivity by the high mobility of the Π -electrons.

Graphite has 4 atoms per unit cell with 4 valence electrons each. This leads to the formation of 16 energy bands not counting the spin. There are 12 σ -bands (6 bonding and 6 antibonding) and 4 Π -bands (2 bonding and 2 antibonding). The

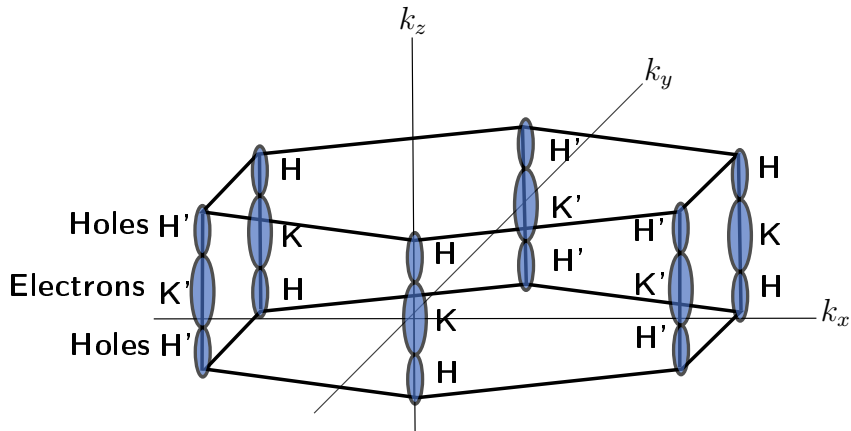


Figure 1.2: Illustration of the first Brillouin zone of Graphite. The Fermi surfaces of the electrons and the holes (indicated in blue) are located in the regions close to the edges HKH and H'K'H' of the Brillouin Zone. The overlap of the upper Π -bands along the Brillouin zone edges HKH and H'K'H' makes graphite a semi metal.

band gap for the σ -bands is about 5 eV. Figure 1.2 shows the first Brillouin zone of graphite. The Fermi surfaces of the electrons and the holes are located in the regions close to the edges HKH and H'K'H' of the Brillouin Zone. The overlap of the upper Π -bands along the Brillouin zone edges HKH and H'K'H' makes graphite a semi metal. [41–43] Table 1.1 shows the electrical conductivities (σ_a, σ_c), the mobilities (μ_a, μ_c) and the electron density (n) for pyrolytic graphite. The index a denotes the in plane conductivity / mobility and c the conductivity / mobility perpendicular to the planes. Due to the technological difficulties to measure the intrinsic c-axis conductivity the actual value of the ratio of σ_a/σ_c is still under discussion.

1.3. Glass-Like Carbon

Glass-like carbon is a class of non-graphitizable carbon which is produced by a series of heat treatments of organic precursors [44, 45]. According to the IUPAC recommendations for the terminology of carbon as a solid [46], glass-like carbon, is an "agranular non-graphitizable carbon with a very high isotropy of its structural and physical properties and with a very low permeability for liquids and

Table 1.1: Electrical conductivities (σ_a, σ_c), mobilities (μ_a, μ_c) and the electron density (n) of pyrolytic graphite (data from [34]).

		300 K	77.5 K	4.2 K
σ_a	($10^4 S/cm$)	2.26	3.87	33.2
σ_c	(S/cm)	5.9	3.3	3.8
μ_a	($10^4 cm^2/Vs$)	1.24	5.75	7.0
μ_c	(cm^2/Vs)	3.3	5.0	8.0
n	($10^{18} cm^{-3}$)	11.3	4.2	3.0

gases". A model for the structure of glass-like carbon was developed by Jenkins and Kawamura [47]. They assumed, that glass-like carbon consists of fibrils which are very narrow, curved and twisted ribbons of graphitic carbon. This model has been widely accepted but did not explain some of the properties of glass-like carbon. The model suggested conjoined micropores and a relatively high proportion of edge atoms which is a contradiction to the high chemical stability and the low gas permeability of glass-like carbon. Detailed high resolution transmission electron microscopy (HRTEM) studies have revealed the presence of many, apparently fullerene-like structure elements in glass-like carbon [48]. These can be multi-layered sheets which are warped by the incorporation of 5 and 7 fold rings in the graphitic layers.

2. Tetrapodal Zinc Oxide

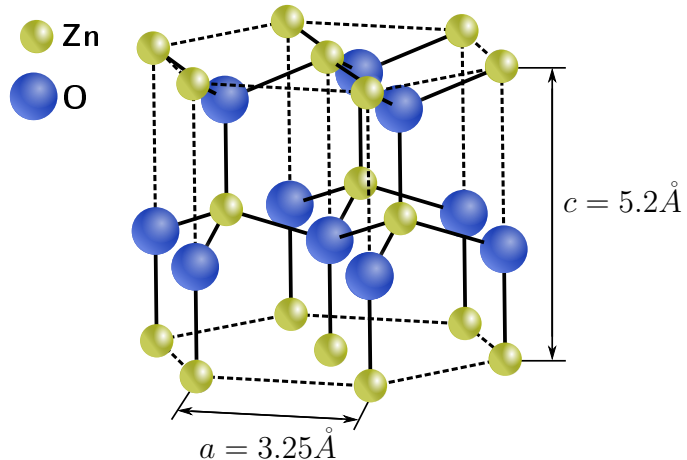


Figure 2.1: Wurtzite-type crystal structure of zinc oxide.

In order to explain the morphology of Aerographite it is crucial to discuss about the atomic structure of zinc oxide (ZnO) because it is utilized as sacrificial template material in the synthesis of Aerographite. ZnO occurs in three different crystal structures namely the cubic sodium chloride structure, the cubic zincblende structure and the hexagonal wurtzite structure (displayed in Figure 2.1) which belongs to the space group $P6_3mc$. Under ambient conditions the wurtzite structure is thermodynamically stable and thus the most common structure. [49, 50]

By oxidizing zinc in air, the self assembled growth of ZnO tetrapods can occur (see Figure 5.3) [32,33]. Until now, several growth models were developed to explain the self assembly to ZnO tetrapods. The exact growth mechanism of the ZnO tetrapods is still under discussion, but all proposed models describe the growth mechanism of the ZnO tetrapods out of a seed nucleus [51, 52]. Iwanaga *et al.* introduced a octahedral twin model which is based on the idea that the central nucleus is an octahedral multiple inversion twin made up of eight-trigonal pyramidal crystals

with $\{0001\}$ basal planes and three $\{11\bar{2}2\}$ twin planes [53].

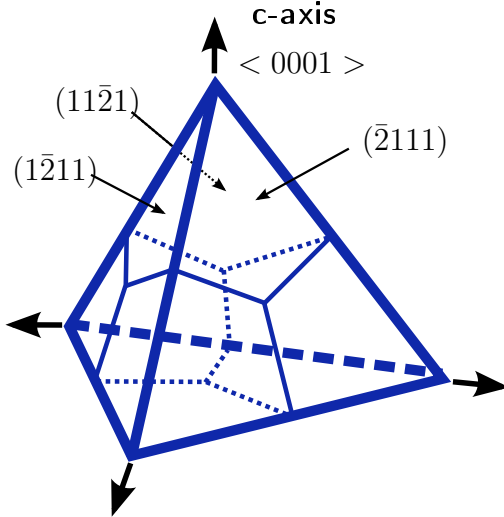


Figure 2.2: Schematic drawing of the tetrahedral nucleus in the center of the tetrapods proposed by Ronning [54]. The tetrahedral nucleus consists of four equivalent grains with triangular dipyramidal shape. The c-axis of the hexagonal grains is parallel to the apexes of the tetrahedron.

Based on detailed TEM studies, Ronning introduced a different model of the tetrapod center core [54]. In this model the central core of the tetrapod consists of four grains of hexagonal structure which are directly related to the four arms of the tetrapod. For the growth of the tetrapods, zinc clusters of less than 20 atoms get oxidized and form spheroid structures built from Zn_3O_3 hexagons and Zn_2O_2 rhombi. These spheroids grow by the condensation of additional Zn and O atoms until they become unstable and collapse towards nanoparticles of the more stable bulk crystal structure. The reason for this phase transition is the minimization of the formation energy of different surfaces, the grain-boundary interface energy and the volume energy.

In wurtzite ZnO, the (0001) -Zn and the $(000\bar{1})$ -O surfaces have the highest surface energy of 4 J/m^2 resulting from their polar character [54]. Therefore a morphology with suppressed (0001) polar surfaces of the nanoparticles is favorable. Ronning suggested that the atomic cluster collapses into a tetrahedron which consists out of four equivalent grains with triangular dipyramidal shape (see Figure 2.2). The

c-axis of the hexagonal grains is parallel to the apexes of the tetrahedron. From the energetic point of view the proposed geometry is favorable because it posses the minimal ratio between grain boundary areas and surface areas in comparison to other multiple-grain arrangements.

The four arms of the tetrapod start to grow when the four microscopic ZnO grains overgrow the tetrahedral nucleus because of the fast growth of the hexagonal ZnO along the c-axis direction. The aspect ratio of the tetrapod arms depends on the growth rate in the c-axis direction compared to with the $(11\bar{2}1)$ surfaces.

3. Mechanical Aspects of Cellular Materials

In this chapter a number of theoretical aspects for the mechanical properties of Aerographite will be discussed. Aerographite possesses a comparatively high Young's modulus with respect to its low density. To evaluate this material properties and to compare it with other cellular and noncellular materials, the Young's modulus-density chart (introduced by Michael F. Ashby [55]) will be discussed in particular. Furthermore, the deformation mechanisms and differences of bending and stretch dominated networks will be discussed. To analyze and discuss the results from Aerographite bulk measurements, the theoretical background of visco-elasticity and Van der Waals forces are introduced in this chapter.

3.1. The Young's Modulus-Density Chart

For the construction of a lightweight beam, which possesses a minimum deflection if subjected to bending moments, a material with a high Young's modulus and a low density is required. To achieve the smallest deflection with the lowest mass of the beam, the ratio of the Young's modulus and the density has to be maximized. For the simple bending case of the beam illustrated in Figure 3.1 the second moment of area I is given by *equation (3.1)* where w denotes the width and h the height.

$$I = \frac{wh^3}{12} \quad (3.1)$$

The deflection of the beam in the direction of the applied force is calculated by *equation (3.2)* where F denotes the force, L the length, E the Young's modulus and

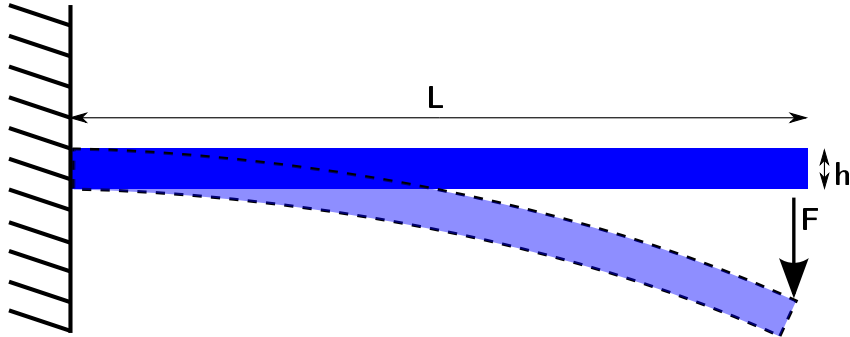


Figure 3.1: Schematic drawing of a free standing beam which is subjected to a bending moment by an external force F . The deflection is indicated by the dashed contour and scales with the second moment of area of the beam and the Young's modulus of the utilized material. If the bending moment is caused by the weight of the beam itself, the merit index $k = \sqrt[3]{E}/\rho$ of the material becomes important for the minimization of the deflection. The same holds if the mass of the beam has to be minimized for a given deflection.

I the second moment of area.

$$\delta = \frac{FL^3}{3EI} \quad (3.2)$$

By inserting *equation (3.1)* into *equation (3.2)* δ can be expressed by *equation (3.3)*.

$$\delta = \frac{4FL^3}{Ewh^3} \quad (3.3)$$

The volume of the beam multiplied with the density ρ of the selected material gives the total mass m like shown in *equation (3.4)*.

$$m = Lwh\rho \quad (3.4)$$

Hence, the deflection of the beam can be expressed as in *equation (3.5)* if the height h is a free parameter.

$$\delta = \left(\frac{4FL^6w^2}{m^3} \right) \left(\frac{\rho^3}{E} \right) \quad (3.5)$$

The first part just dependents on the geometry and the total mass of the beam and the second part of *equation (3.5)* is a material dependent parameter. To achieve the minimum deflection of a beam with fixed mass and free height, the merit index $k = \sqrt[3]{E}/\rho$ has to be maximized. This merit index depends only on the utilized

material while the other parameters in *equation (3.5)* are engineering ones which determine the shape and mass of the beam. [56]

$$k = \frac{\sqrt[3]{E}}{\rho} \quad (3.6)$$

This merit index (*equation (3.6)*) emphasizes the importance of a low density material, to minimize the mass of a beam for a given deflection or to minimize the deflection of a beam with fixed mass. For example Balsa wood performs very well in this kind of application due to the very small density ($40 - 340 \text{ kg/m}^3$) [57] and the comparatively high Young's modulus (see Figure 3.2).

A comparison of materials with different merit index k is presented in the material selection chart in Figure 3.2 which is also known as Ashby map / diagram. In the Ashby map the logarithm of the density is plotted versus the logarithm of the Young's modulus. In the double logarithmic plot one achieves a linear relation between the Young's modulus E , density ρ and merit index k which gets obvious by reformulating *equation (3.6)* to *equation (3.7)* and can be represented as a straight line in Figure 3.2 [55, 59, 60].

$$\log(E) = 3\log(\rho) + 3\log(k) \quad (3.7)$$

The slope is given by the exponent of the Young's modulus in *equation (3.6)* and the intercept with the y axis is given by the term $3\log(k)$. In this material selection map, all materials of the same merit index k , can be found on a straight line. All materials above this line provide a higher merit index, meaning the ratio $\sqrt[3]{E}/\rho$ is higher than for the materials below the line. This makes the Ashby map a valuable tool for the material selection if a high specific stiffness is required [55, 59, 60].

If a beam of fixed mass, height and free width is exposed to bending moments, the deflection gets minimized if the merit index k_2 (*equation (3.8)*) is maximized.

$$k_2 = \frac{E}{\rho} \quad (3.8)$$

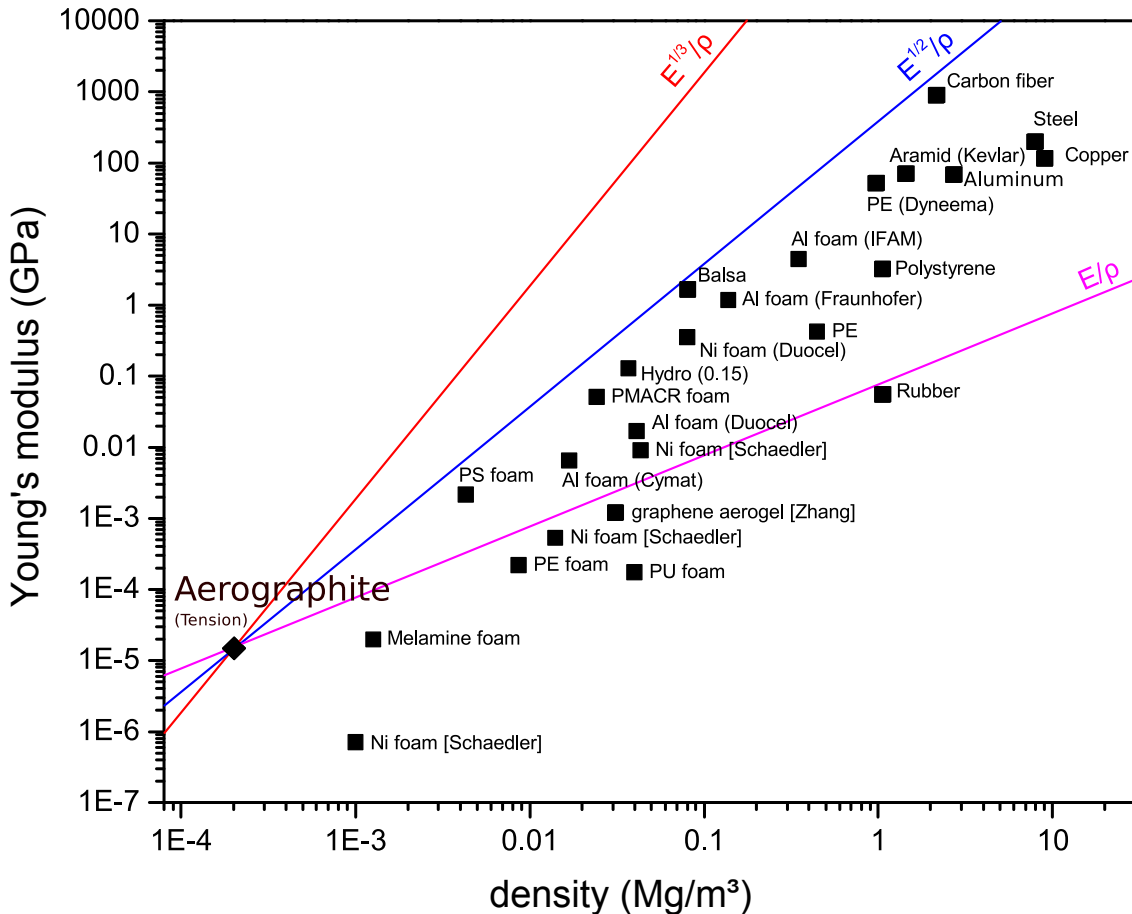


Figure 3.2: Young's modulus-density chart which includes a huge variety of materials of different material classes [22, 23, 58]. The colored lines indicate the merit indices according to equation 3.6, 3.8 and 3.9. All materials which lay in the diagram on the same line exhibit the same merit index. The merit index $k = \sqrt[3]{E}/\rho$ is essential for the construction of a free standing beam, which possesses minimum deflection caused by its own weight.

The merit index k_3 (equation (3.9)) determines the deflection of a beam, with fixed cross sectional area and mass. The guidelines for k_2 and k_3 are also displayed in Figure 3.2. These guidelines just differ by their slope in the material selection chart because the exponent in the formula of the individual merit index differs.

$$k_3 = \frac{\sqrt{E}}{\rho} \quad (3.9)$$

3.2. Bending- and Stretch-Dominated Networks

When a porous network material is mechanically loaded, two different deformation mechanisms occur depending mainly on the geometry of the network. The deformation of the unit cells of the network can be either bending- or stretch-dominated and this has a strong influence on the mechanical performance of the networks and their position in the Young's modulus-density chart.

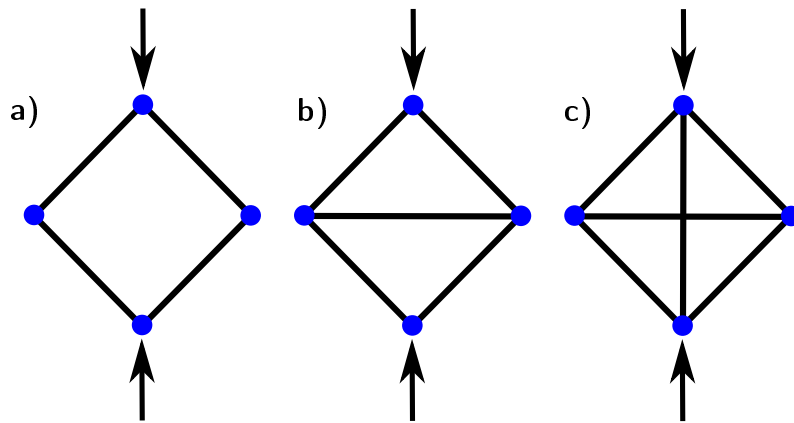


Figure 3.3: Overview for three different cases of the Maxwell stability criterion for the unit cell of a two dimensional network. The arrows indicate an external mechanical load. a) Example of a bending-dominated network: It can withstand the external force only by the bending of the junctions (indicated in blue color) and can bear small forces without collapsing. b) Example of a stretch-dominated network: The strut in the center carries tension and increases the stiffness significantly. The increase in stiffness caused by the bent junctions is very small in comparison to the contribution of the strut in the center. c) This unit cell is over-constrained. If one of the two struts in the center is under compression, the perpendicular one will be under tension. The unit cell can be in a state of self-stress, even in the absence of some external load.

To identify, if the deformation mechanism of a lattice is either bending- or stretch-dominated, it is necessary to introduce the Maxwell stability criterion [61]. The Maxwell criterion for the idealized cell of a two dimensional network, which consists of b struts and j frictionless junctions, as depicted in Figure 3.3, is given by equation (3.10). For the three dimensional case the Maxwell criterion is given by equation (3.11). If the Maxwell criterion is fulfilled, the network is statically and

kinematically determinate and can not be folded [55].

$$M = b - 2j + 3 = 0 \quad (3.10)$$

$$M = b - 3j + 6 = 0 \quad (3.11)$$

For the case $M < 0$, the cell is not rigid and can be "folded". When the unit cell is subjected to load, it will start to deform by the bending of the junctions. Networks which consist of such unit cells are categorized as bending-dominated networks.

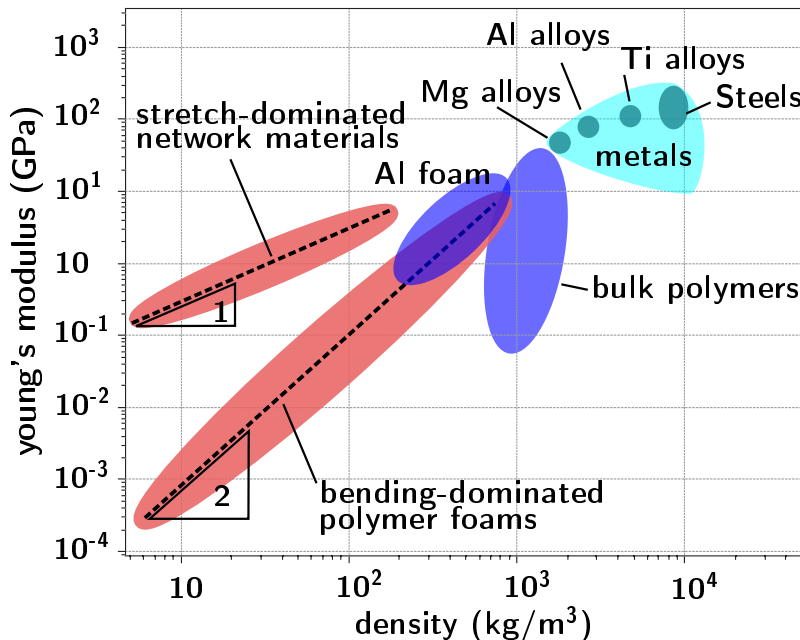


Figure 3.4: Young's modulus density chart for porous and bulk materials. The red areas indicate the regions where either bending- or stretch-dominated network materials can be found. The stretch-dominated networks possess higher structural efficiency than the bending-dominated networks which is indicated by the different slopes in the diagram. The stretch dominated networks lie along a line with slope = 1, while the bending dominated ones lie along a line with slope = 2.

For the case $M \geq 0$, the cell behaves completely different. If some external load is applied, its struts will experience tensile and compressive forces and the contribution from the bent junctions has just some minor influence because the load is almost carried exclusively by the struts. These kind of networks are categorized as stretch-

dominated networks and possess a higher structural efficiency than the bending-dominated networks. The difference in the structural efficiency is very pronounced in the Young's modulus-density chart. The bending-dominated networks lie along a line of slope 2 while the stretch-dominated networks are located along a line of slope 1, as shown in Figure 3.4.

$$b - 3j + 6 = s - m \quad (3.12)$$

Equation 3.10 and 3.11 are the necessary conditions for rigidity, but not in general the sufficient conditions because they do not consider the states of self-stress and of mechanisms in the network [62]. Equation 3.12 represents a generalization of the Maxwell condition in 3D, where s and m denote the states of self-stress and mechanisms respectively [63]. Figure 3.5 shows the schematic stress/strain curve

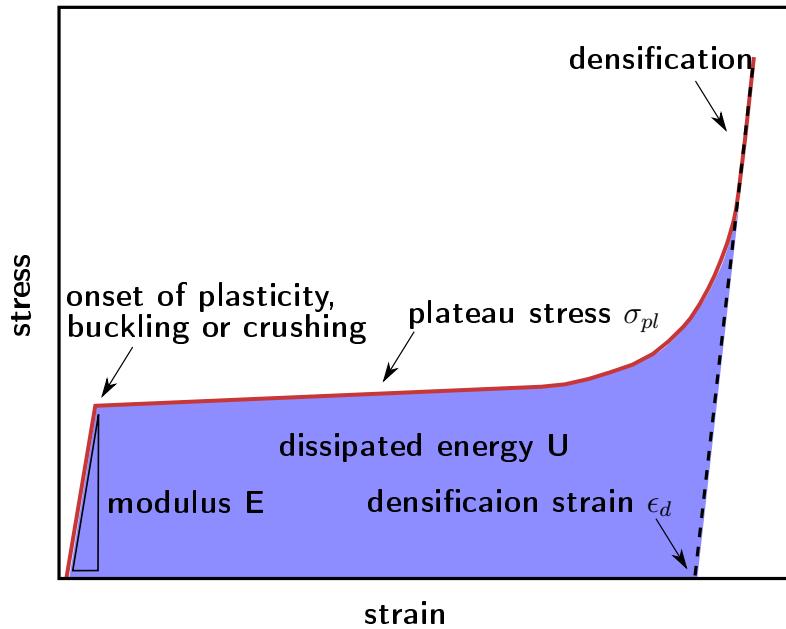


Figure 3.5: Schematic stress/strain curve of a bending-dominated network material under compression. The network shows linear elastic response up to the elastic limit. If the elastic limit is overcome, the junctions of the unit cells start to yield for either by buckling or fracturing. For further compression the stress remains nearly constant at the plateau stress σ_{pl} until the opposing sides of the unit cells impinge each other and the stress increases rapidly in the so called densification regime.

of a bending-dominated network under compression. The network exhibits a linear elastic response until the junctions of the unit cells start to yield either by buckling or fracturing. With further compression the stress stays nearly constant at the plateau stress σ_{pl} . For even stronger compression the network gets densified and the opposing sides of the unit cells impinge each other. This results in a rapid increase of the stress in the so called densification region [59, 64].

3.3. Modeling of Visco-Elastic Material Properties

Purely elastic materials can be described by Hooke's law of linear elasticity according to *equation* (3.13) where σ denotes the stress, ϵ the strain and E the Young's modulus.

$$\sigma = E\epsilon \quad (3.13)$$

The viscous motion of a Newtonian fluid can be described by *equation* (3.14) where η denotes the viscosity, $d\epsilon/dt$ denotes the strain rate and σ the stress. A Newtonian fluid is characterized by a linear relationship between stress and strain rate.

$$\sigma = \eta \frac{d\epsilon}{dt} \quad (3.14)$$

The term visco-elasticity is used for materials which exhibit both, elastic and viscous characteristics, during deformation. The difference between a visco-elastic material and a purely elastic material is the time dependence of the mechanical response. When a linear elastic material is loaded at constant strain rate, the stress will increase linearly with a slope according to the Young's modulus (see Figure 3.6(a)). By overcoming the yield stress, the material starts to deform plastically but this threshold is independent of the strain rate. The stress response of a linear visco-elastic material loaded at constant strain rate is illustrated in Figure 3.6(b). The curve shape of the linear visco-elastic material is related to the time dependence of the viscous properties of the material and depends on the strain rate [65]. For Visco-elastic materials creep can occur, which means that the strain increases while

the stress is held constant. The case of decreasing stress in a visco-elastic material which is held at constant strain is denoted as relaxation.

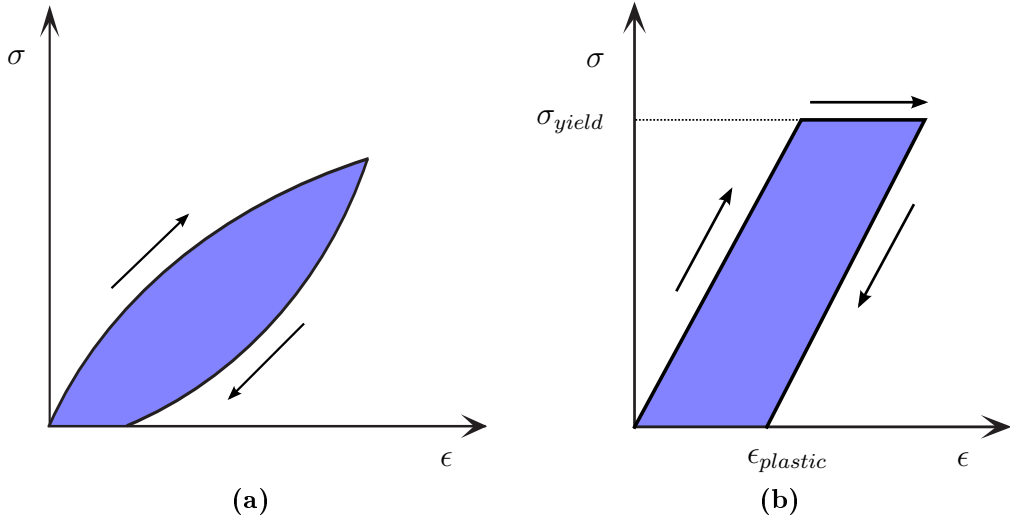


Figure 3.6: a) Schematic representation of a linear visco-elastic material loaded with a constant strain rate. b) Schematic representation of an ideal linear elastic-plastic material which is loaded up to the yield stress.

Visco-elasticity can be observed in various materials with very different causal mechanisms. For metals, visco-elastic behavior is normally just observable, at high stresses, high temperatures or at long time scales. In metals, mechanisms like dislocation movement, twinning, grain boundary slip or atomic diffusion (at high temperatures) can cause a viscous material behavior [66].

Many synthetic polymers which are not highly cross linked show visco-elasticity as well. In polymers, the most relevant mechanism for visco-elasticity is a rearrangement of the molecular chain conformations with respect to the applied stress [67]. However, the free movement of the polymer chains is inhibited by covalent cross links or chain entanglements and secondary bonds. The presence and length of side groups at the backbone also hinders the movement of the polymer chains. With increasing temperature weak secondary bonds between the molecular chains become unstable which strongly affects the chain mobility. The increased mobility of the chains results in an accelerated reorientation of the chain conformation. Hence, the

polymer possesses a smaller viscosity and the visco-elastic behavior becomes more dominant.

The mechanical response of a visco-elastic material can basically be modeled by a mechanical equivalent circuit of springs and dashpots which are representative for the elastic (energy conserving) and viscous (energy dissipative) components of the material. In the following, the three most important models [65–69] will be discussed in detail.

Maxwell Model

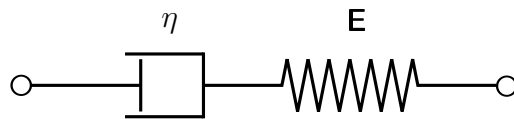


Figure 3.7: Schematic representation of a Maxwell model.

The Maxwell model consists of a serial connection of a dashpot with viscosity η and a spring of elastic constant E like depicted in Figure 3.7. The total strain is the sum of the strains from the dashpot and the spring. The change of the strain with respect to time is described by *equation (3.15)* where σ denotes the stress, ϵ the strain, η the viscosity and E the elastic constant.

$$\frac{d\epsilon}{dt} = \frac{d\epsilon_{dashpot}}{dt} + \frac{d\epsilon_{spring}}{dt} = \frac{\sigma}{\eta} + \frac{1}{E} \frac{d\sigma}{dt} \quad (3.15)$$

With $\tau = \eta/E$ the equation can be rewritten to *equation (3.16)*.

$$E \frac{d\epsilon}{dt} = \frac{d\sigma}{dt} + \frac{\sigma}{\tau} \quad (3.16)$$

If a constant stress is applied, this model predicts an instant strain response by the spring element. As long as the stress is applied, the strain will increase linear with time, due to the dashpot element. For the case of a fixed strain the model predicts an exponential stress decay which is actually in good accordance to the real behavior of many polymers. [67]

Kelvin-Voigt Model

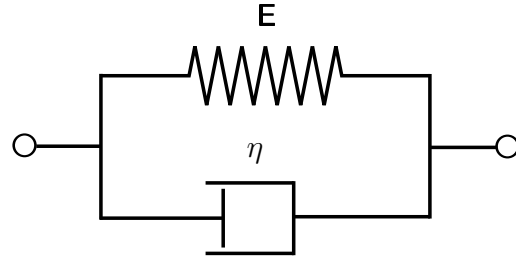


Figure 3.8: Schematic representation of a Kelvin-Voigt model.

The Kelvin-Voigt model consists of a parallel connection of a dashpot and a spring element, like depicted in Figure 3.8. The dashpot and the spring experience the same strain and therefore the total stress is the sum of the stresses in the dashpot and the spring element like given by equation (3.17).

$$\sigma(t) = E\epsilon(t) + \eta \frac{d\epsilon(t)}{dt} \quad (3.17)$$

If constant stress is applied, the strain approaches asymptotically the value of σ/E with a decreasing strain rate. It can not model the instantaneous strain response which is attributed to the elastic properties of the material.

Standard Linear Solid Model

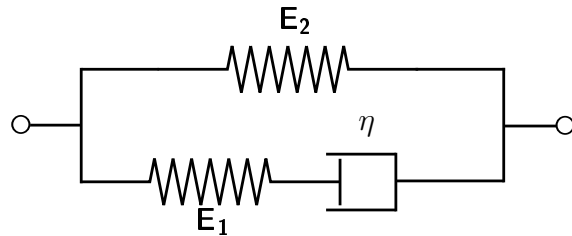


Figure 3.9: Schematic representation of the standard linear solid model.

The standard linear solid model is a more realistic approach for the modeling of visco-elastic material behavior. It consists of a parallel connection of a Maxwell element and a spring element like depicted in Figure 3.9. This means, for the side

with the Maxwell element again *equation* (3.16) holds with $\tau = \eta/E_1$.

$$E_1 \frac{d\epsilon}{dt} = \frac{d\sigma_1}{dt} + \frac{\sigma_1}{\tau} \quad (3.18)$$

The spring side is described by *equation* (3.19).

$$\frac{d\sigma_2}{dt} = E_2 \frac{d\epsilon}{dt} \quad (3.19)$$

The total stress which acts on the standard linear solid model is the sum of the individual stresses given by *equation* (3.20).

$$\frac{d\epsilon(t)}{dt} = (E_1 + E_2)^{-1} \left(\frac{d\sigma(t)}{dt} + \frac{E_1}{\eta} \sigma(t) - \frac{E_1 E_2}{\eta} \epsilon(t) \right) \quad (3.20)$$

The standard linear solid model combines the exponential stress relaxation of the Maxwell model and with the creep behavior of the Kelvin-Voigt model which has been discussed above. Also it will react with an instant elastic deformation if a step like stress is applied. [65–69]

3.4. Van der Waals Forces

Van der Waals (VdW) forces, named after the Dutch scientist Johannes Diderik van der Waals [70], are weak interaction forces between atoms or molecules which are even present in noble gas atoms. In contrast to ionic or covalent binding forces, Van der Waals forces are relatively weak with a potential energy which decays with the sixth power of the separation distance between the atoms or molecules. Van der Waals forces are the origin of the attractive energy part in the Lennard Jones potential (negative part of *equation* (3.23)) and basically the term van der Waals force can be divided in the following forces:

- the Keesom forces which are the forces between two permanent dipoles
- the Debye forces which are the forces between a permanent dipole and the corresponding induced dipole

- the London dispersion forces which occur between a instantaneous dipole and a corresponding induced dipole [71]

In between non-polar molecules or atoms the London dispersion forces are the reason for the attractive interaction. Neutral atoms exhibit no permanent dipole moment according to equation *equation (3.21)* where d denotes the dipole moment and ψ the wave function.

$$\langle d \rangle = -e \int \psi^* x \psi dV = 0 \quad (3.21)$$

However, the spatial distribution of the electron density in the atom / molecule exhibits temporary fluctuations. The electron probability density in an atom is not always symmetric with respect to the atomic nucleus. Due to the uncertainty principle in quantum mechanics the center of the electronic charge distribution does not always coincide with the positively charged atomic nucleus, leading to the formation of an instantaneous dipole moment. This instantaneous dipole moment can induces a second dipole moment in a neighboring atom/molecule resulting in an attractive force between the instantaneous and the induced dipole, the reason for the London dispersion forces [72–75].

$$U_{VdW} = -C_6/R^6 \propto d_{ind}E_{inst} \quad (3.22)$$

The electrical field of the instantaneous dipole decays with $E_{inst} \propto 1/R^3$ and it induces a dipole moment of $d_{ind} \propto 1/R^3$ in the neighboring atom. [76, 77] The VdW potential (*equation (3.22)*) represents the attractive part of the Lennard-Jones potential in *equation (3.23)* while the repulsive part of the Lennard-Jones potential originates from to the Pauli principle and the corresponding energy increase when electron shells of the atoms start to overlap.

$$U_{LJ} = \frac{C_{12}}{R^{12}} - \frac{C_6}{R^6} \quad (3.23)$$

4. Electrochemical Devices

Due to the high specific surface area and the electrical conductivity Aerographite is a promising candidate for the application as electrode material. Therefore, in this chapter the theoretical aspects of the lithium-sulfur battery and the electrical double-layer capacitor will be discussed because prototypes of these devices were built with Aerographite electrodes and tested.

4.1. Electrical Double-Layer Capacitor

An electrical double-layer capacitors (EDLC) represents a special type of capacitor which utilizes an electrical double-layer to achieve huge capacities. The so called Helmholtz double-layer, named after Hermann von Helmholtz who described it first [78], forms at the electrode/electrolyte interfaces when a bias voltage is applied to the EDLC. Figure 4.1 presents a simplified schematic of an EDLC.

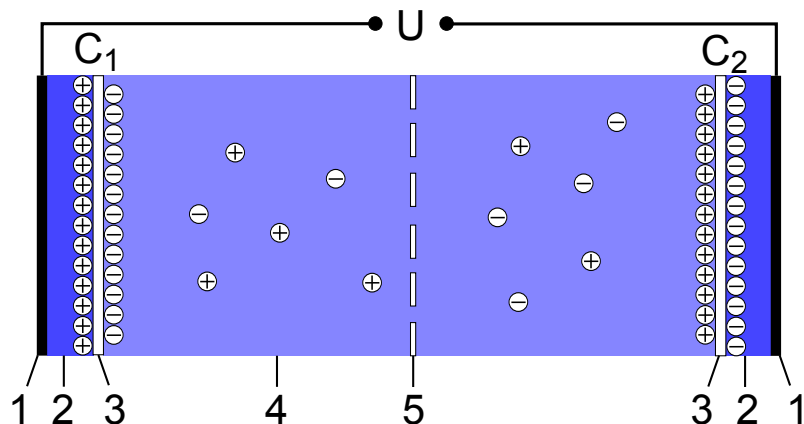


Figure 4.1: Schematic setup of an biased electrical double-layer capacitor (EDLC): 1) current collector 2) polarized electrodes 3) Helmholtz double-layer 4) electrolyte 5) separator

In the case of an applied bias voltage between the electrodes, the electrodes become

polarized by the electrical field and attract ions from the electrolyte. One electrode exhibits a positive surface charge and attracts anions from the electrolyte (left side of Figure 4.1) and the opposing electrode exhibits a negative surface charge and attracts cations from the electrolyte (right side of Figure 4.1) [79]. In between the solvated ions and the surface of the electrode a layer of polarized solvent molecules from the electrolyte inhibits a charge transfer which just occurs above a certain threshold bias voltage. The surface charge in the electrode and the opposing adjacent layer of ions in electrolyte is denoted as Helmholtz double-layer and possesses a electrical capacity.

$$C = \epsilon_0 \epsilon_r \frac{A}{d} \quad (4.1)$$

The capacity C of the Helmholtz double-layer can be calculated analogous to a parallel plate capacitor and is given by *equation* (4.1). Here, A denotes the area of the double-layer and d the thickness of the double-layer which depends on the ion concentration in the electrolyte and ranges from $\approx 0.1 - 10 \text{ nm}$ [80]. The huge capacities of the latest EDLC are related to the very thin double-layer and the huge surface area of the porous electrodes [81]. To achieve high surface areas, normally activated or porous carbon electrodes with a specific surface areas reaching $\approx 3000 \text{ m}^2/\text{g}$ are applied [79].

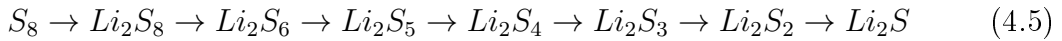
The two electrodes of the EDLC represent a serial connection of two individual capacitors. Hence, the total capacity of the EDLC is given by *equation* (4.2). For a symmetric EDLC with two electrodes of the same capacity meaning ($C_1 = C_2$) the total capacity equals one half of the capacity of a single electrode.

$$C_{total} = \frac{C_1 C_2}{C_1 + C_2} \quad (4.2)$$

The so called pseudo capacity denotes a second mechanism of EDLCs with advanced capacity. Here the application of a voltage induces faradaic currents from the oxidation and reduction of electroactive materials (e.g. RuO_2 , Co_3O_4 or IrO_2) [80,82].

4.2. Lithium-Sulfur Battery

The lithium-sulfur battery is a promising candidate for a rechargeable battery with a 3-5 times higher theoretical energy density than current lithium-ion batteries [83]. Due to technological issues namely the polysulfide shuttle [84] the cyclic stability of the current lithium-sulfur is very limited and there are no batteries commercially available at the moment. During the discharge of the lithium-sulfur battery, the lithium gets oxidized at the anode (*equation (4.3)*) and reacts with sulfur at the cathode where polysulfides are formed (*equation (4.4)*). *Equation (4.5)* shows the different transition states of the polysulfides until the complete discharge of a lithium-sulfur battery. During the charge and the discharge, of a lithium-sulfur battery, these polysulfides can coexist in different concentrations in the battery.



sulfur is an electrical insulator which implies that the electrical conductivity has to be increased for the utilization as cathode material. One solution for this problem is the application of sulfur-carbon composites with increased electrical conductivity and the option of a sulfur confinement to suppress the polysulfide shuttle [85]. A further technological challenge of the lithium-sulfur battery is the increasing volume of the cathode during the discharge. The Li_2S exhibits about twice the volume of elemental sulfur. This volumetric swelling induces mechanical stress in the cathode and can decrease the electrical conductivity because the carbon becomes detached from the sulfur. To overcome this problems, it is necessary to find an cathode material which is sufficiently conductive, inhibits the polysulfide shuttle and can withstand the strong volume changes during charge and discharge of the lithium-sulfur battery [86].

Part II.

Experimental

5. Synthesis of Aerographite

Since the discovery of Aerographite, already numerous different variants have been synthesized and examined [31]. The synthesis parameters and structures of all these Aerographite variants are discussed in more detail in the PhD thesis of Matthias Mecklenburg [87]. The synthesis of Aerographite is basically divided into two process steps. In the first step ZnO tetrapods are produced by the flame transport synthesis [32, 33] and are connected to 3D networks by compression and post annealing. In the second step of the Aerographite synthesis, a modified chemical vapor deposition (CVD) process is applied to the 3D ZnO network samples and they are converted into Aerographite. Evaporated toluene provides the carbon for the nucleation and growth of the enclosing graphitic shells, whilst the underlying ZnO network is reduced and removed by the gas flow of hydrogen. This means that the ZnO samples are applied as sacrificial templates in the CVD process.

5.1. Flame Transport Synthesis of Zinc Oxide

The ZnO tetrapods are produced by the so called flame transport synthesis (FTS) [32, 33]. In this method a ceramic crucible (volume $\approx 60\text{ cm}^3$) is filled with 2/1 ratio of Polyvinylbutyral (PVB) and zinc powder with a grain size of $\leq 10\text{ }\mu\text{m}$. This crucible is placed in a Nabertherm LE2/11 muffle furnace (see Figure 5.1) and heated within 15 min to 900°C . The oxygen from the ambient atmosphere inside the furnace leads to the combustion of the powder mixture which ignites at ≈ 600 to 700°C . In the flame above the crucible, zinc vapor gets oxidized and grows mainly in the shape of tetrapods by self-assembly, as described in chapter 2 [32, 52–54, 88]. The growing tetrapods are transported by the convection in the flame until they

fall on the catcher substrate. The length of the arms of these tetrapods normally ranges from 5 to $50\text{ }\mu\text{m}$ and the diameter of the arms ranges from 1 to $5\text{ }\mu\text{m}$. The aspect ratio, morphology and size of the tetrapods dependents mainly on the traveling time of the tetrapods and the partial pressures of zinc and oxygen in the flame. After cooling the furnace down to room temperature, the ZnO tetrapods can be harvested from the catcher substrate and the crucible. Subsequently the ZnO tetrapods are combined to network templates by compression and annealing. Detailed descriptions, studies and analysis of the FTS can be found in the PhD thesis of Ingo Paulowicz [89].

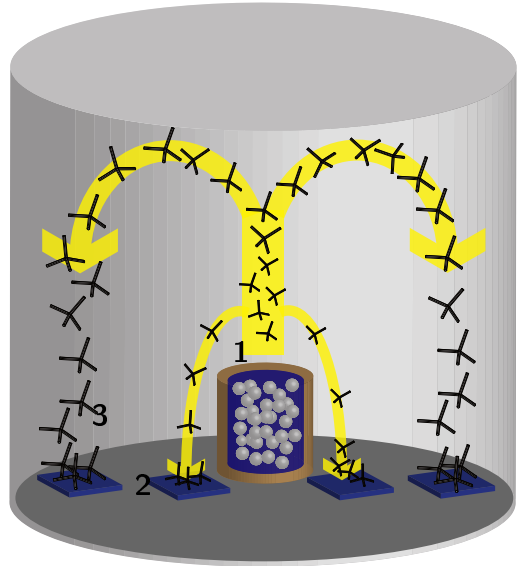


Figure 5.1: Schematic representation of the applied flame transport synthesis for the fabrication of tetrapodal zinc oxide: 1) crucible with zinc PVB powder mixture 2) catcher substrates 3) grown zinc oxide tetrapods

5.2. Post Annealing of Zinc Oxide Tetrapod Networks

The ZnO tetrapods are filled into self designed stainless steel pistons and compressed into cylindrical ceramic molds made from aluminium oxide (Friatec Degus-

sit). These molds are annealed in a Nabertherm L3/12 muffle furnace for 5 hours at 1150°C . After the annealing step the ZnO tetrapods are interconnected in a free standing 3D network (Figure 5.3) and the samples can be pressed out of the ceramic molds as shown in Figure 5.2.

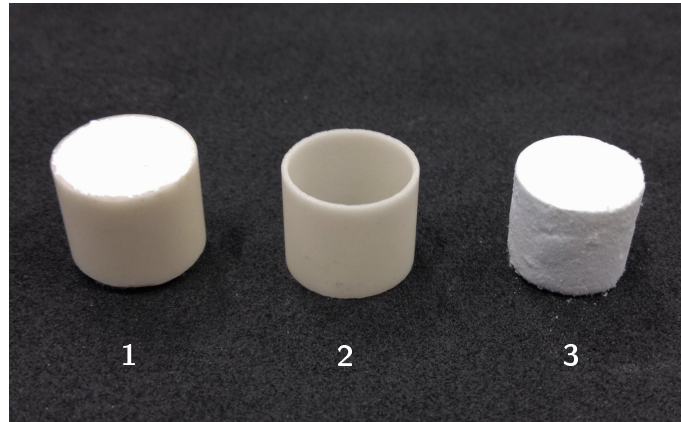


Figure 5.2: Photograpgh of the 1 cm^3 ZnO templates: 1) ZnO network template in the ceramic mold for the post annealing step 2) empty ceramic mold 3) finished 1 cm^3 ZnO template

The applied densities of the ZnO network templates reached from 0.2 g/cm^3 to 0.3 g/cm^3 resulting in a porosity of $\approx 97\%$. In order to avoid ZnO residuals inside the Aerographite after the conversion of the templates in the chemical vapor deposition (CVD), it is advantageous to apply ZnO templates with a density below 0.3 g/cm^3 . Hereby the total mass of the ZnO, which has to be removed during the conversion, is smaller. For the mechanical experiments cylindrical samples of 11 mm diameter and 10.5 mm height were produced resulting in a sample volume of 1 cm^3 .

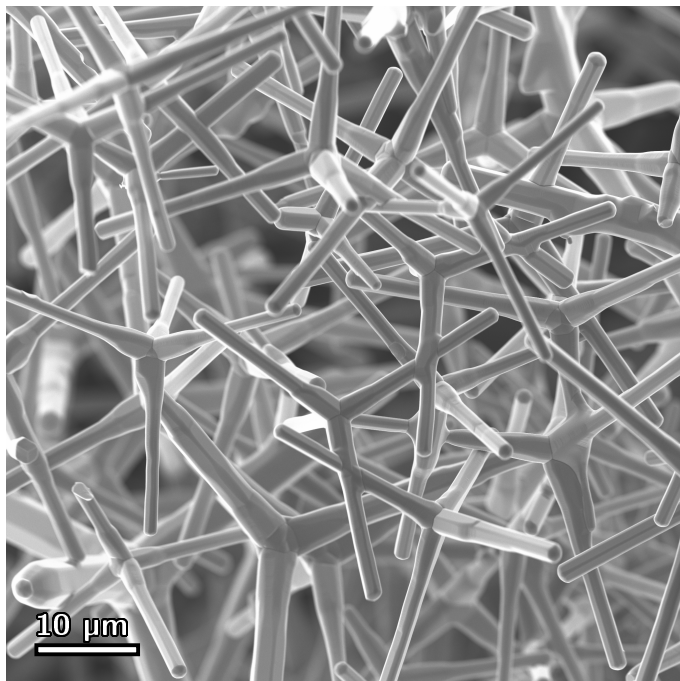


Figure 5.3: SEM micrograph of a ZnO tetrapod network employed as sacrificial template in the CVD synthesis of Aerographite.

5.3. Conversion of Sacrificial Zinc Oxide Templates by Modified Chemical Vapor Deposition

The conversion of the sacrificial ZnO templates to Aerographite is conducted in a CVD reactor with a two zone split tube furnace (quartz tube; *length* = 1300 mm; *diameter* = 110 mm) (schematically depicted in Figure 5.4).

The ZnO templates are placed on a silicon wafer in the high temperature zone of a tube furnace. For the synthesis of Aerographite with closed graphitic shells and hollow tubes the CVD parameters depicted in Figure 5.5 are applied [31]: At a constant temperature of 200 °C in the injection zone and 760 °C in the main zone, an Argon gas flow of 0.2 l/min (at atmospheric pressure) is applied for 15 min. Subsequently, the injection of toluene (99 % Alfa Aesar) at 5.5 ml/h (for 1 g of ZnO template mass) is initialized and a hydrogen gas flow of 0.06 l/min is applied. The

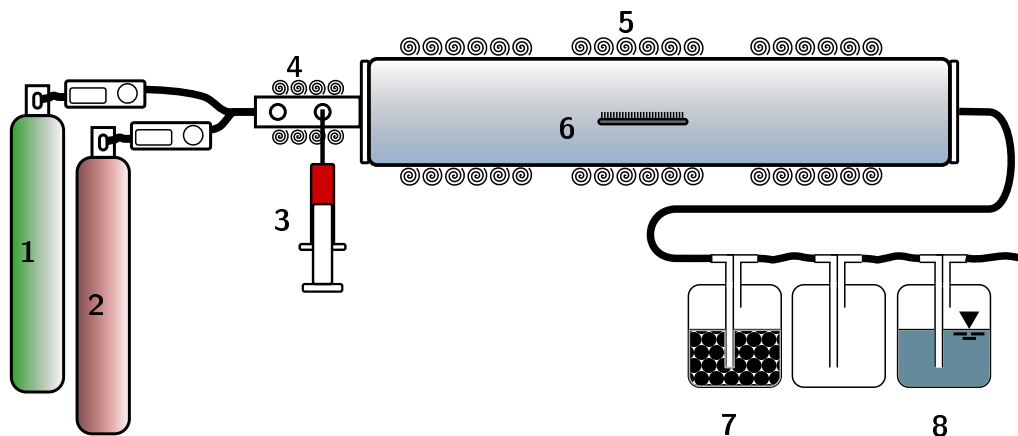
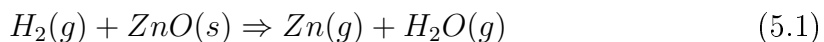


Figure 5.4: Schematic setup of the CVD reactor: 1) Argon gas supply with gas flow controller 2) Hydrogen gas supply with gas flow controller 3) Toluene injection pump 4) Toluene evaporation unit 5) tube furnace 6) quartz glass tube (with Silicon wafer for the sample support) 7) activated carbon (exhaust gas system) 8) silicone oil (exhaust gas system)

cracking products of the evaporated toluene provide the required carbon for the growth of Aerographite. The toluene injection is maintained for 60 min until it is stopped. For the next 60 min the toluene injection is stopped while the Argon and hydrogen gas flows are maintained and the temperature is increased to 900 °C. Subsequently a second injection of toluene with 5.5 ml/h is started for 120 min at 760 °C. For the second toluene injection the Argon gas flow is stopped and a hydrogen gas flow of 0.06 l/min is applied. The last step of the CVD synthesis is a rinsing with pure Argon at 0.6 l/min until the reactor is cooled down. These process parameters are optimized for a CVD synthesis with a maximum mass of 2 g of the ZnO templates.



The cracking products from the supplied toluene provide the carbon for the growth of the graphitic walls while the sacrificial ZnO network template is decomposed by the supplied hydrogen gas to zinc vapor and water according to equation (5.1). [90] The growth of the graphitic layers during the conversion process follows almost ex-

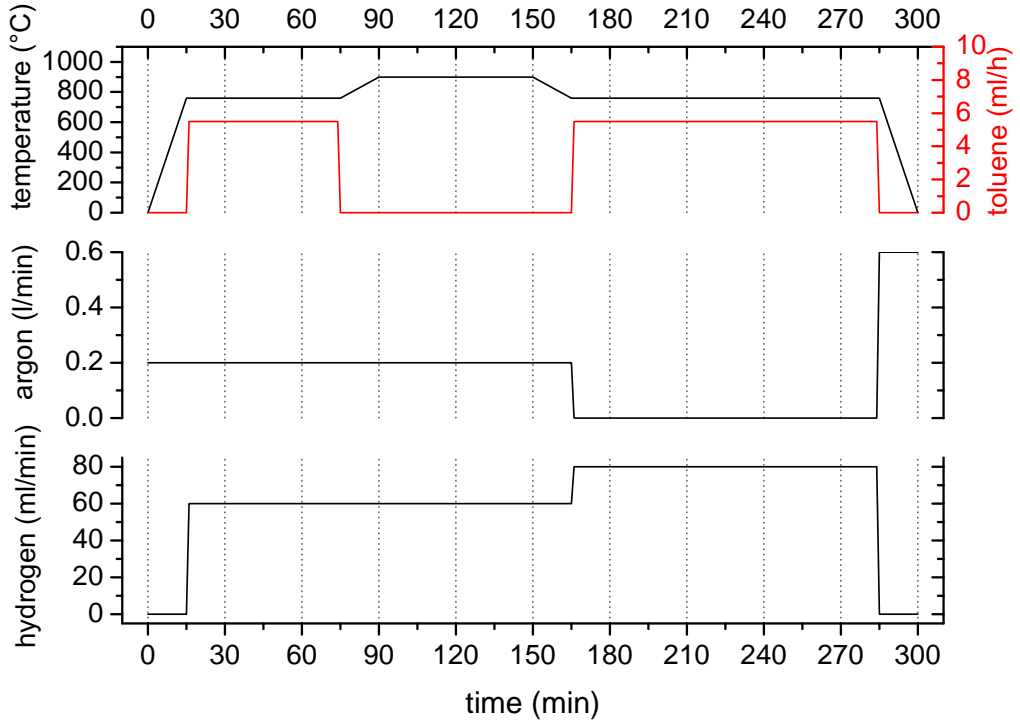


Figure 5.5: Generic temperature profile, toluene injection rate, Argon flux and hydrogen flux for the CVD synthesis of Aerographite with hollow tubes and closed walls. The displayed toluene injection rate corresponds to a ZnO mass of 1 g in the CVD reactor.

actly the template structure which means that Aerographite is an exact mimicry of the ZnO template architecture depicted in Figure 5.6(d). In Figure 5.6 an overview of the different conversion states during the synthesis of Aerographite is shown.

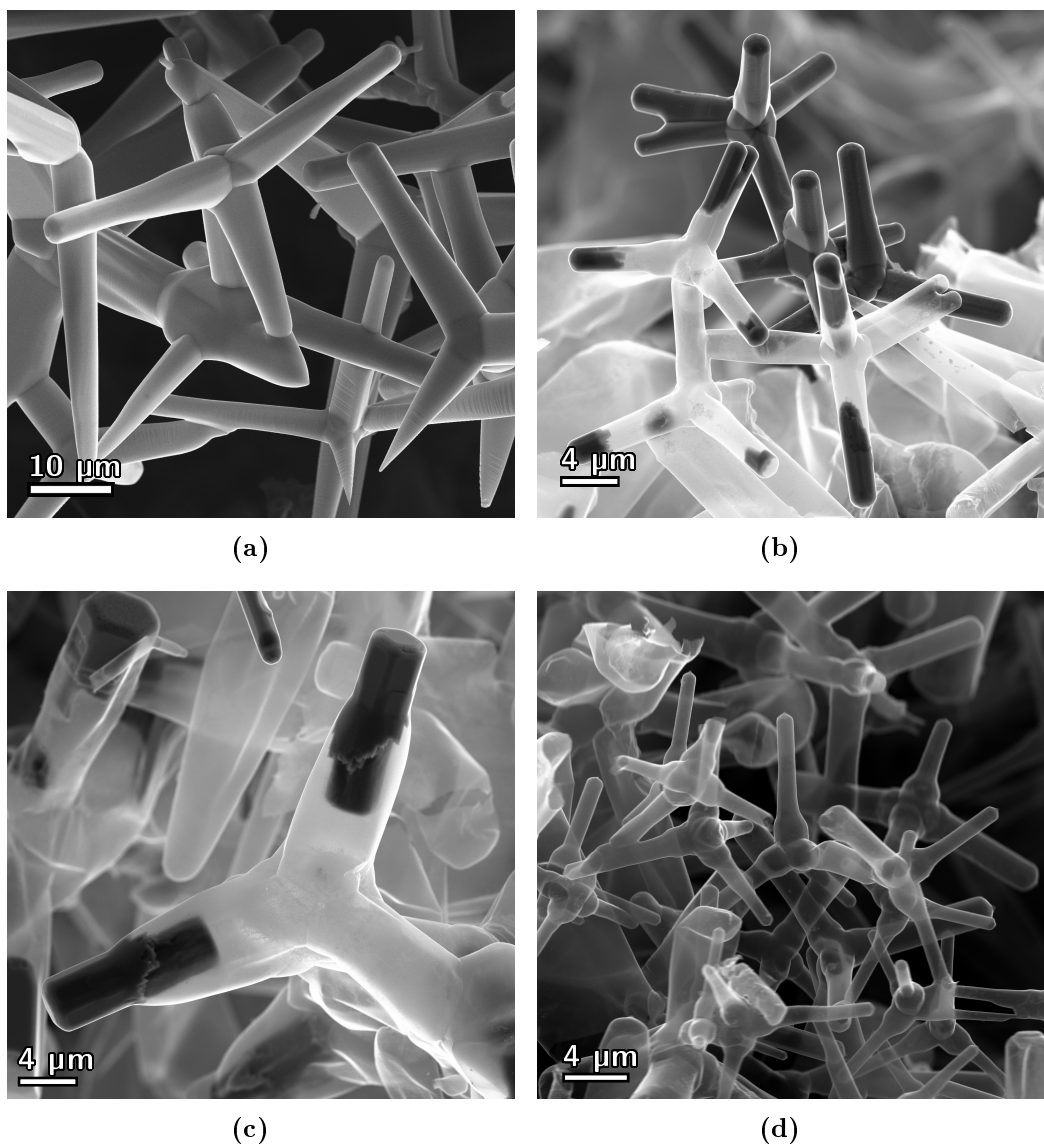


Figure 5.6: SEM micrographs from the conversion states during the synthesis of Aerographite: a) Virgin ZnO tetrapod template produced by the flame transport synthesis. b) Partially converted Aerographite with residual ZnO inside the graphitic tubes. c) Partially converted Aerographite with residual ZnO crystals inside the graphitic tubes. d) Finished Aerographite after the complete removal of the underlying ZnO network.

6. Characterization Methods

For the bulk and in situ measurements at Aerographite a number of new methods were developed and applied. These newly developed methods are introduced and discussed in this chapter.

6.1. Mechanical Characterization Setup

To perform tensile and compression tests at Aerographite bulk samples, it was necessary to develop a completely new testing setup. There were no mechanical testing machines commercially available in the market which allowed the measurement of the forces and deformations with the required accuracy for such a soft material like Aerographite. Therefore the design, construction, machining, assembling and calibration of a mechanical-test setup for the cyclic compressive and tensile deformation of Aerographite bulk samples, was realized.

This setup consists of a *Maerzhaeuser Wetzlar HS 6.3* micro manipulator which is driven by a stepper motor, a *Kern PLE 310-3N* precision balance, a *Keithley 6400* source-meter and is controlled by a self written *LabView* program. In this setup the Aerographite sample is placed in between the micro manipulator and the precision balance. The micro manipulator deforms the sample while the balance measures the generated force and the source-meter records the electrical resistance of the sample. For vibration damping the whole setup was placed on a very rigid aluminum plate in a box filled with sand which was mounted on a vibration isolated table. In Figure 6.1 a photograph of the setup is shown.

For a compression or tensile test the LabView program controls the micro manipulator, which deforms the sample by an user defined step size. Subsequently the

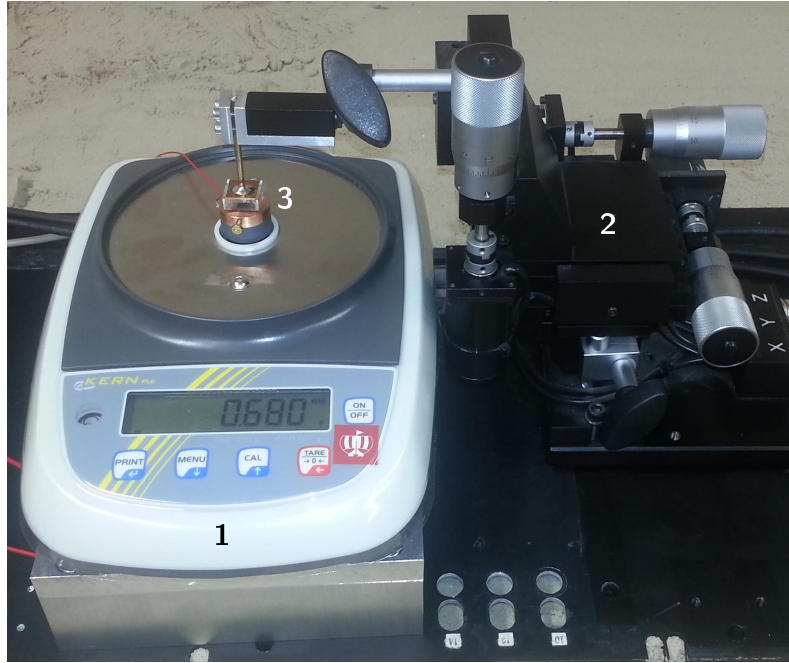


Figure 6.1: Photograph of the utilized mechanical test setup: 1) precision balance 2) micro manipulator 3) mechanical/electrical contacts

program waits until an user defined settling time has been elapsed and afterwards records the generated force by the precision balance. This procedure repeats until a user defined maximum deformation is reached and the direction of the deformation steps is inverted until the manipulator comes back to the original height of the sample. This deformation cycle can be repeated for several hundreds of cycles to examine some long term change in the mechanical behavior of the sample. In addition to this, the LabView program can record the applied voltage, the current and the resistance of the sample for each deformation step by the connected source-meter. The program allows it to record a complete current/voltage curve for each deformation step. Alternatively, the program records the resistance for a constant bias voltage. This allows it to monitor the change in the sample resistance depending on the deformation state and the number of deformation cycles. A screenshot of the developed LabView program is shown in Figure 13.6 in the appendix.

Due to the delay of the analog-to-digital converter of the utilized balance, it was necessary to include a settling time in the measurement program. After the de-

formation of the sample by the micro manipulator the program pauses for a user defined settling time until the balance reaches a stable equilibrium state and reads out the detected force from the balance. This ensures, that the balance reaches its equilibrium state. Therefore, in all performed experiments this settling time was set to a value of 4 s . The only exception are the experiments in chapter 11.2 for the strain rate dependence of visco-elasticity.

The accuracy of the mechanical setup was validated by a number of calibration measurements with a set of 8 springs from *Febrotec* with four different spring constants, ranging from 0.033 N/mm to 0.25 N/mm . The spring constants have been chosen accordingly to the modulus of Aerographite, to validate the setup for the same regime. Table 6.1 displays the measured spring constants and the deviation from the spring constants denoted by the manufacturer.

Table 6.1: Validation data for the mechanical setup for bulk measurements.
Eight springs with four different spring constants were measured.

spring constant (N/mm)	0.033	0.075	0.155	0.25
measurement at spring 1	0.0315	0.0672	0.145	0.244
measurement at spring 2	0.0300	0.0695	0.142	0.246
difference	0.0015	0.0023	0.003	0.002
average	0.0308	0.0684	0.1435	0.245
deviation from spring constant	6.7%	8.8%	7.4%	2%

The force/displacement curves showed a typical linear elastic behavior like expected from a spring. The maximum error was determined with 8.8% for the second softest spring and decreased to 2% for the strongest spring. In consideration of the manufacturer error it can be expected that the real measurement error of the setup is much smaller than the examples which are listed up in table 6.1. It is significant that all measurements resulted in a smaller spring constant than the manufacturer data. This indicates an systematic error of either the setup or even of the spring constant claimed by the manufacturer. Further, the measurements

indicate a smaller percentage error for higher spring constants. In conclusion the validation measurements revealed a maximum error of $\approx 9\%$. For stiffer samples the error is significantly smaller.

The minimum settling delay, which has to elapse before the force from the precision balance is read out, was determined with 4 s . This is attributed to the analog/digital converter in the balance, which requires a settling time until it reaches steady state. This means, a step size of $5\text{ }\mu\text{m}$ results in an effective strain rate of $1.25\text{ }\mu\text{m/s}$ and for $10\text{ }\mu\text{m}$ step size the effective strain rate measures $2.5\text{ }\mu\text{m/s}$ respectively.

6.2. Mechanical In Situ Experiments of Aerographite

To study the mechanical and electrical properties of individual Aerographite structures and to explain the electrical and mechanical results from the bulk measurements, mechanical in situ measurements with the scanning electron microscope were conducted together with the University of Riga in Latvia.

The used *Hitachi S-4800* SEM was equipped with a custom made sample holder with four piezo driven nano-manipulators (see Figure 6.2). Each manipulator could move in x, y and z direction. The manipulators consisted of three linear *SmarAct SLC-1720* positioners and provided a x, y and z working space of $12\text{ mm} \times 12\text{ mm} \times 12\text{ mm}$. In addition to this, the sample can be rotated relative to the manipulators by a piezoelectric stage. The manipulators were controlled by a *SmarAct HCU-3DM* control unit.

For the different in situ experiments the manipulators were either equipped with edged gold tips or some very soft, atomic force microscopy (AFM) cantilevers of the type *Olympus BL-RC-150VB* (spring constant from 2.9 to 50 pN/nm). By an electrical throughput the gold tips were connected to an Keithley 6430 sub-femtoamp sourcemeter.

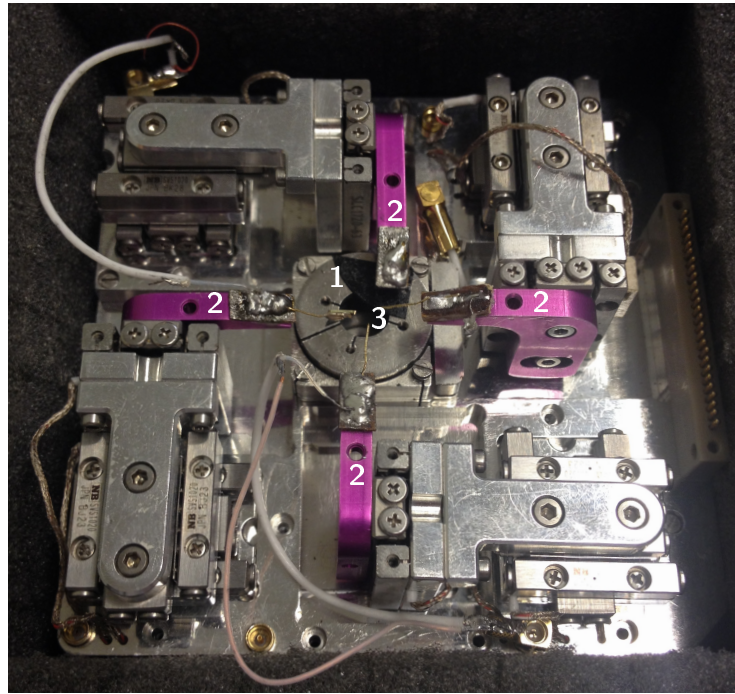


Figure 6.2: Photograph of the SEM sample holder which has been utilized for the mechanical *in situ* experiments: 1) rotatable sample stage 2) piezo driven nano manipulator arm 3) gold tips for the mechanical and electrical contacts

The applied Aerographite samples were prepared in three different ways:

- Aerographite structures were glued to the gold tip with conductive silver epoxy *cw 2400* from *Chemtronics*
- Aerographite structures were glued on a silicon wafer with conductive silver epoxy *cw 2400* from *Chemtronics*
- Aerographite structures were placed on a silicon wafer and got stuck there by Van-der-Waals forces

In order to study the stiffness of individual Aerographite tetrapod arms, a number of separated and freely accessible tetrapods were bent by an AFM cantilever. For this purpose only tetrapods firmly bound to the substrate were selected and tested. This means, tetrapods with three arms bound to the substrate and one arm pointing straight up, were measured. By moving the tip of the AFM cantilever

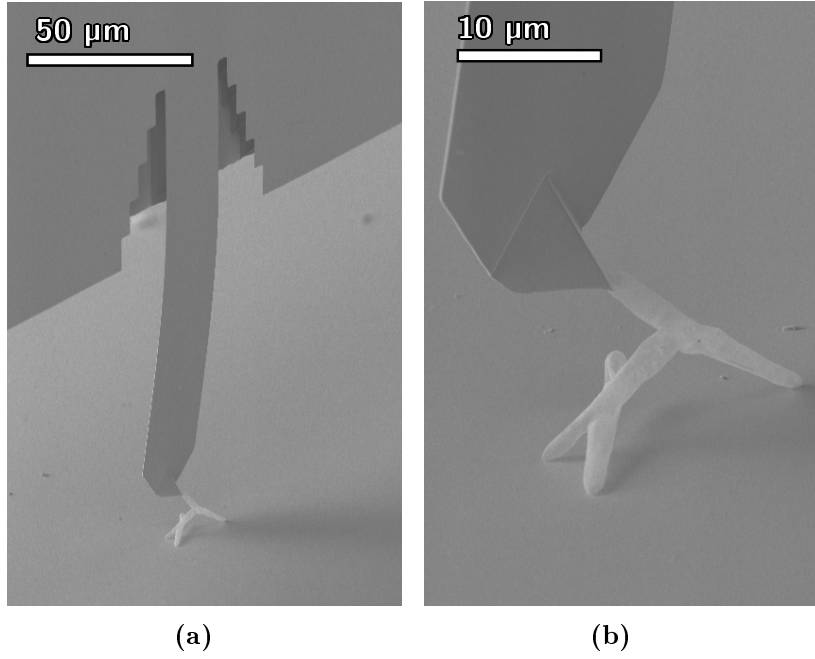


Figure 6.3: SEM micrograph of an Aerographite tetrapod placed on a silicon wafer and bent by an AFM cantilever (atomic force microscopy). From the deflection of the cantilever the acting force was calculated and also the applied torque at the tetrapod arm. Due to the low acceleration voltage of 3 keV does the Aerographite tetrapod appear nontransparent in the SEM despite its hollow nature.

against the tetrapod one arm was bent while the deflection of the cantilever was recorded in a video. From each of these bending experiments a series of SEM micrographs and a video was taken. From the video, a set of single frames was extracted and the deflection of the AFM cantilever and the tetrapod arm was measured by the use of the software *ImageJ*.

6.3. Electrical In Situ Experiments

For the electrical experiments at individual Aerographite structures, single tubes were mounted in between two gold tips by the following method. First, one Gold tip was dipped in conductive epoxy and subsequently it was poked in an Aerographite network. After this procedure, a bunch of tubes and tetrapods adhered to the tip

and the prepared gold tip was mounted to one of the nano-manipulators. Inside the SEM, a clean gold tip was approached with the second nano-manipulator to one of the Aerographite rods from the bunch and an electrical measurement was conducted. By the application of a high current density of about 10^3 A/mm^2 a very solid contact establishes and the Aerographite tube can be pulled out from the conductive epoxy. Subsequently, the tube was contacted with the third manipulator with a second clean gold tip. By this method, it was possible to establish an electrical contact with a Gold tip on both sides of the Aerographite tube without the conductive epoxy (see Figure 12.3).

7. Aerographite Electrodes

In the following chapter it is described how an electrical double-layer capacitor with Aerographite electrodes and a lithium-sulfur battery with a Aerographite cathode were constructed.

7.1. Electrical Double-Layer Capacitor with Aerographite Electrodes

To demonstrate the applicability of Aerographite as an electrode material, an electrical double-layer capacitor (EDLC) with Aerographite electrodes was built up and measured. The capacitor was built up with two Aerographite electrodes with 1.1 cm^3 volume and 30 mg mass each. The Aerographite electrodes were mounted in small cages made from aluminum foil which acted as current collector and kept the Aerographite in place. These electrodes where dipped into a beaker with 50 ml of 1 molar solution of tetraethylammonium-tetrafluoroborate in acetonitrile as electrolyte. A separator membrane, to prevent some short circuit, was not necessary because the electrodes where not in touch with each other.

In Figure 7.1 the electrical circuit for measurement of the capacity is depicted. The EDLC was modeled by an equivalent circuit, consisting of the capacity C_{EDLC} , a parallel resistor R_p and a serial resistor R_s . The EDLC was charged with a 1.6 V battery and discharged by an resistor $R_{\text{discharge}}$ while the voltage decay was measured by an digital oscilloscope (Agilent DSO 1002A). In order to determine the capacity and the serial resistance and the parallel resistance from the equivalent circuit, the experiment was carried out with two different resistors of $R_1 = 1 \text{ K}\Omega$ and $R_2 = 3.3 \text{ K}\Omega$ and without the discharge resistor. Equation 7.1 describes the

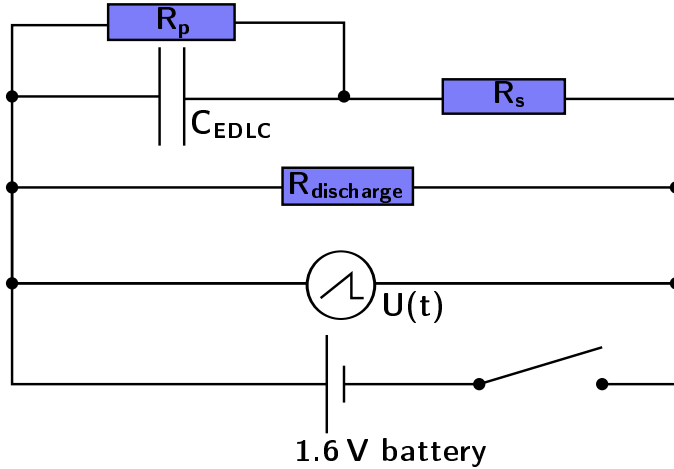


Figure 7.1: Electrical circuit of the experimental setup for the electrical double-layer capacitor measurements. The EDLC was modeled by an equivalent circuit consisting of a capacity C_{EDLC} , a parallel resistor R_p and a serial resistor R_s .

voltage decay during the discharge of the EDLC where τ denotes the time constant which is given by *equation (7.2)*. In *equation (7.2)* C denotes the capacity of the EDLC.

$$U_C(t) = U_0 e^{-t/\tau} \quad (7.1)$$

$$\tau = RC = \left(\frac{1}{R_i + R_{discharge}} + \frac{1}{R_p} \right)^{-1} C \quad (7.2)$$

The discharge measurements of the EDLC were fitted by an exponential decay function according to *equation (7.1)* to determine the time constant τ for different discharge resistors. By applying *equation (7.2)* it was possible to determine the capacity C of the EDLC.

7.2. Lithium Battery with Sulfur Infiltrated Aerographite Cathode

To increase the electrical conductivity of sulfur for the utilization as cathode material, a composite from Aerographite and sulfur was prepared. Sulfur was heated inside a small aluminum mold to a temperature of $125^\circ C$ until it was molten. Af-

terwards, the Aerographite samples with a diameter of 5.5 mm and a thickness of 0.8 mm were dipped in the liquid sulfur. The Aerographite network soaked up the sulfur immediately until it was completely infiltrated. The subsequent cooling to room temperature was conducted on a hotplate at a controlled cooling rate to avoid thermally induced stresses which could cause cracks in the cathode.

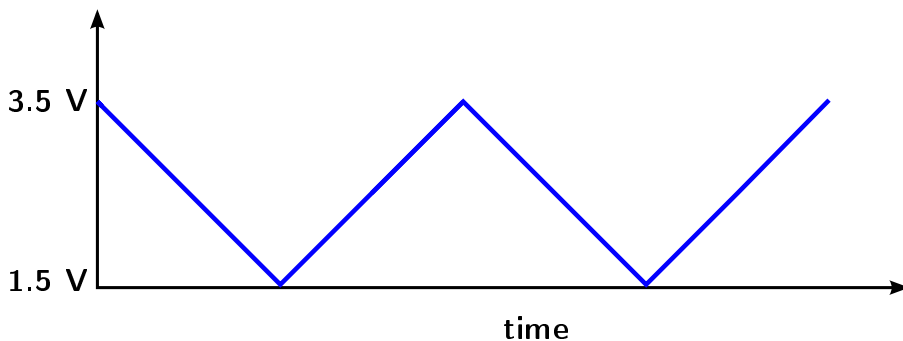


Figure 7.2: Voltage/time profile which is applied to the half cell during the cyclic voltammetry.

The as-prepared cathodes were mounted, inside a glove box with Argon inert gas atmosphere in stainless steel half cells. The anode was made from metallic lithium with a diameter of 10 mm and a thickness of 1 mm . The half cells were filled with 0.5 ml electrolyte of a 0.7 M solution of bis-(trifluoromethylsulfonyl)imide (LiTFSi) in dimethoxyethane (DME) which is a common electrolyte for lithium-sulfur batteries [91]. The glass fiber separator (Whatmann) between the cathode and anode has pore size of $0.7\text{ }\mu\text{m}$ and a thickness of $435\text{ }\mu\text{m}$.

The open circuit voltage of the half cell measured 2.7 V (at room temperature). The as-prepared half cell were subjected to cyclic voltammetry. With the help of the cyclic voltammetry it is possible to analyze the intercalation, alloying and reversibility of electrode processes of unknown half cells. During the cyclic voltammetry, the half cell is connected to a potentiostat which applies a triangular voltage profile (see Figure 7.2) to the half cell and simultaneously measures the current. The cyclic voltammetry was conducted at a sweep rate of 0.1 mV/s in a voltage range from 1.5 V to 3.5 V . The applied sweep rate is sufficiently slow for small sample sizes to maintain equilibrium processes at the electrodes.

Part III.

Results and Discussion

8. Overview of the Basic Physical Properties of Aerographite

Aerographite, discovered in 2012 [31,87], is a 3D network of seamless interconnected microscopic graphitic tubes with nanoscopic wall thickness. Aerographite exhibits an extremely low density ($0.18 - 50 \text{ mg/cm}^3$), super hydrophobicity, electrical conductivity ($0.2 - 37 \text{ S/m}$), is optically opaque and black. Because of its hierarchical network design it is mechanically flexible, can be reversibly compressed, and has an extremely low Poisson ratio. The low density of Aerographite and its relatively high Young's modulus of 15 kPa (at a density of $180 \mu\text{g}$) result in a specific modulus of $E/\rho^2 = 0.46 \cdot 10^6 \text{ Pa}/(\text{kg/m}^3)^2$ respectively $E/\rho^3 = 2.6 \cdot 10^6 \text{ Pa}/(\text{kg/m}^3)^3$ which is the highest value among all known materials. [31]

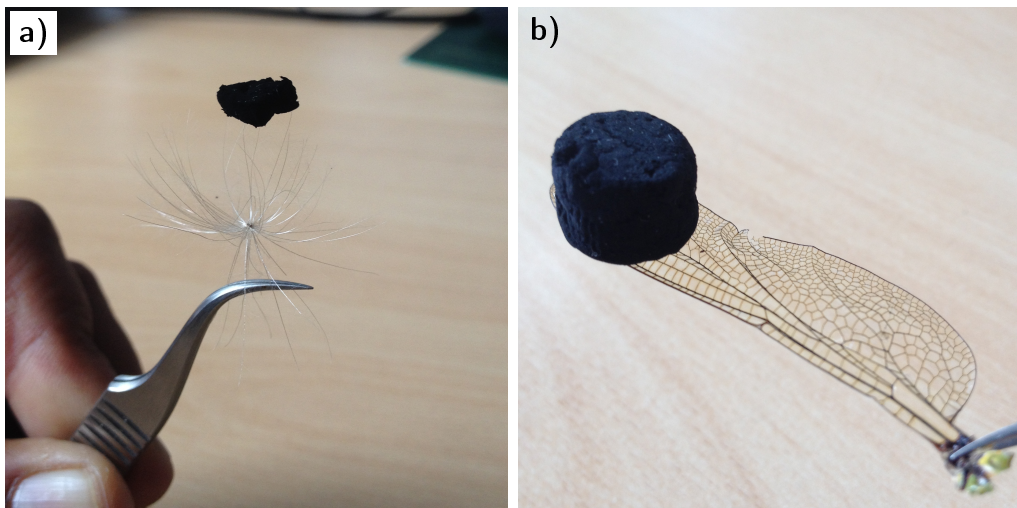


Figure 8.1: a) Photograph from a piece of ultra lightweight Aerographite (density 0.6 mg/cm^3) on top of a very fragile plant seed. b) Photograph of a 2 cm^3 cylinder of Aerographite on top of the wing of a dragonfly. In this photograph the contour of the sample is better recognizable due to dust particles on the surface.

The quality of this number gets more obvious by a look on the Ashby material selection map in Figure 3.2. In this material selection map various materials are compared with respect to their density and Young's modulus according to the merit indexes from equation 3.6, 3.8 and 3.9.

9. Microscopic Morphology and Structure of Aerographite

The different synthesis parameters like template density, toluene injection rate and hydrogen gas supply allow the fabrication of numerous variants of Aerographite [31, 87]. However, within the scope of this thesis, just the two main variants of Aerographite namely the closed shell variant and the hollow framework variant were studied in the mechanically experiments. The, the morphology, hybridization and structure of these two variants will be discussed in this chapter. The relation between the synthesis parameters and the structure of Aerographite as well as the growth mechanism are discussed in detail in the PhD thesis of Matthias Mecklenburg [87].

9.1. Aerographite Variants

Figure 9.1 shows a set of SEM micrographs of the closed shell variant of Aerographite. This variant of Aerographite is made up by a network of seamless interconnected tubes and tetrapods with closed walls (see Figure 9.1(c)). Note, that the numerous junctions between the tubes and tetrapods, which are adopted from the shape of the sacrificial ZnO template, are an exception for carbon nanotubes (CNTs) [92](see Figure 9.1(b)). The density of this closed shell variant goes down to 1 mg/cm^3 which is already below the density of the lightest reported aerogels [21, 22, 29, 93]. The individual tubes, possess a wall thickness of about 15 nm and a diameter of 1 to $5\text{ }\mu\text{m}$.

The second variant, which was mechanically tested, is the so called hollow frame-

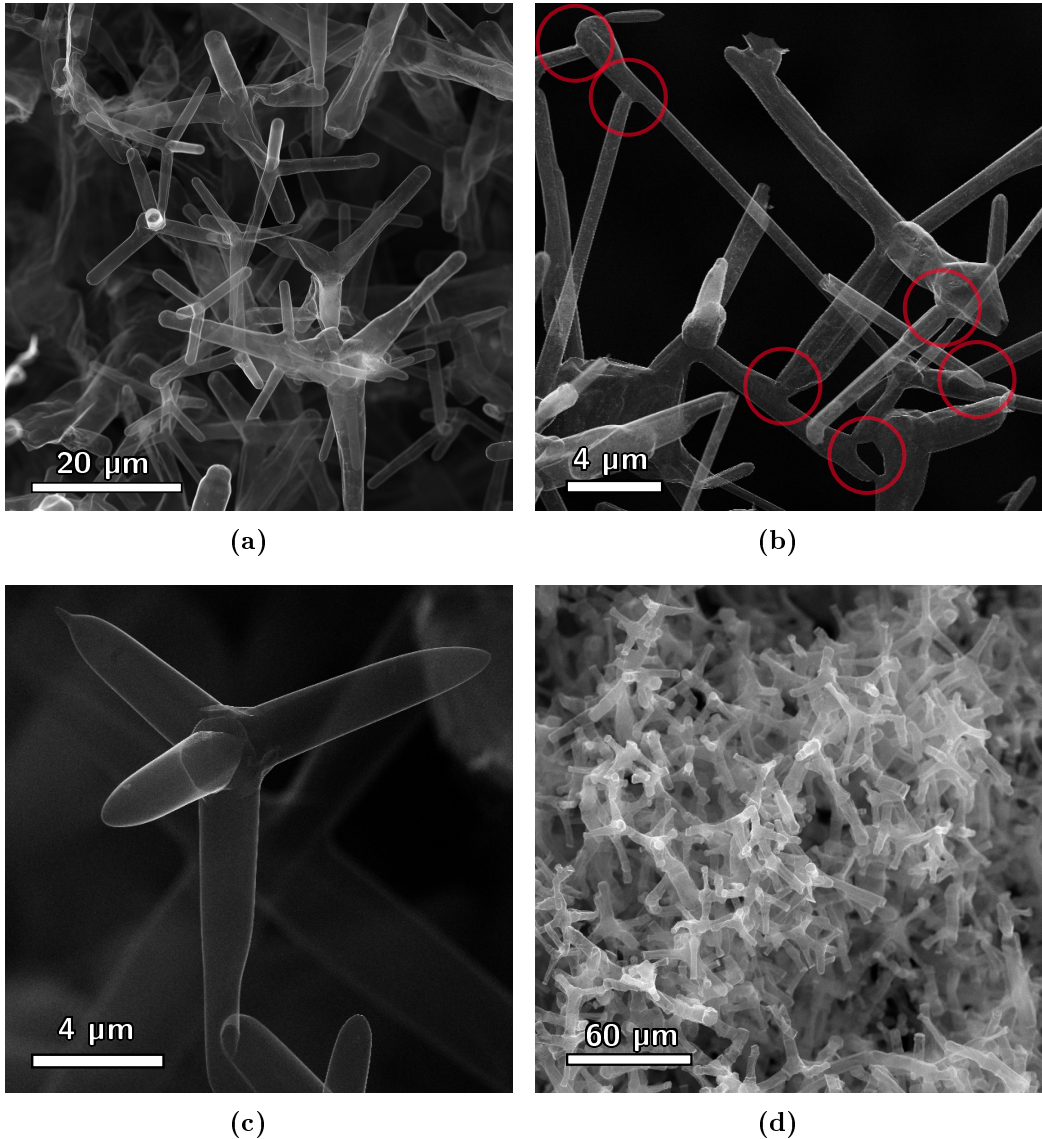


Figure 9.1: SEM micrographs of the closed shell variant of Aerographite. a) Tetrapod network of the closed shell variant of Aerographite. b) Magnified view on the seamless junctions in the tetrapod network (indicated by red circles). The network junctions are adopted from the sacrificial ZnO template. c) Single hollow Aerographite tetrapod with closed surface. d) Tetrapod network with low aspect ratio of the individual tetrapods.

work variant which is depicted in Figure 9.2. For this variant, the amount of provided carbon was drastically reduced during the synthesis by a smaller toluene injection rate, resulting in open/porous walls. Figure 9.2(c) and 9.2(d) show the

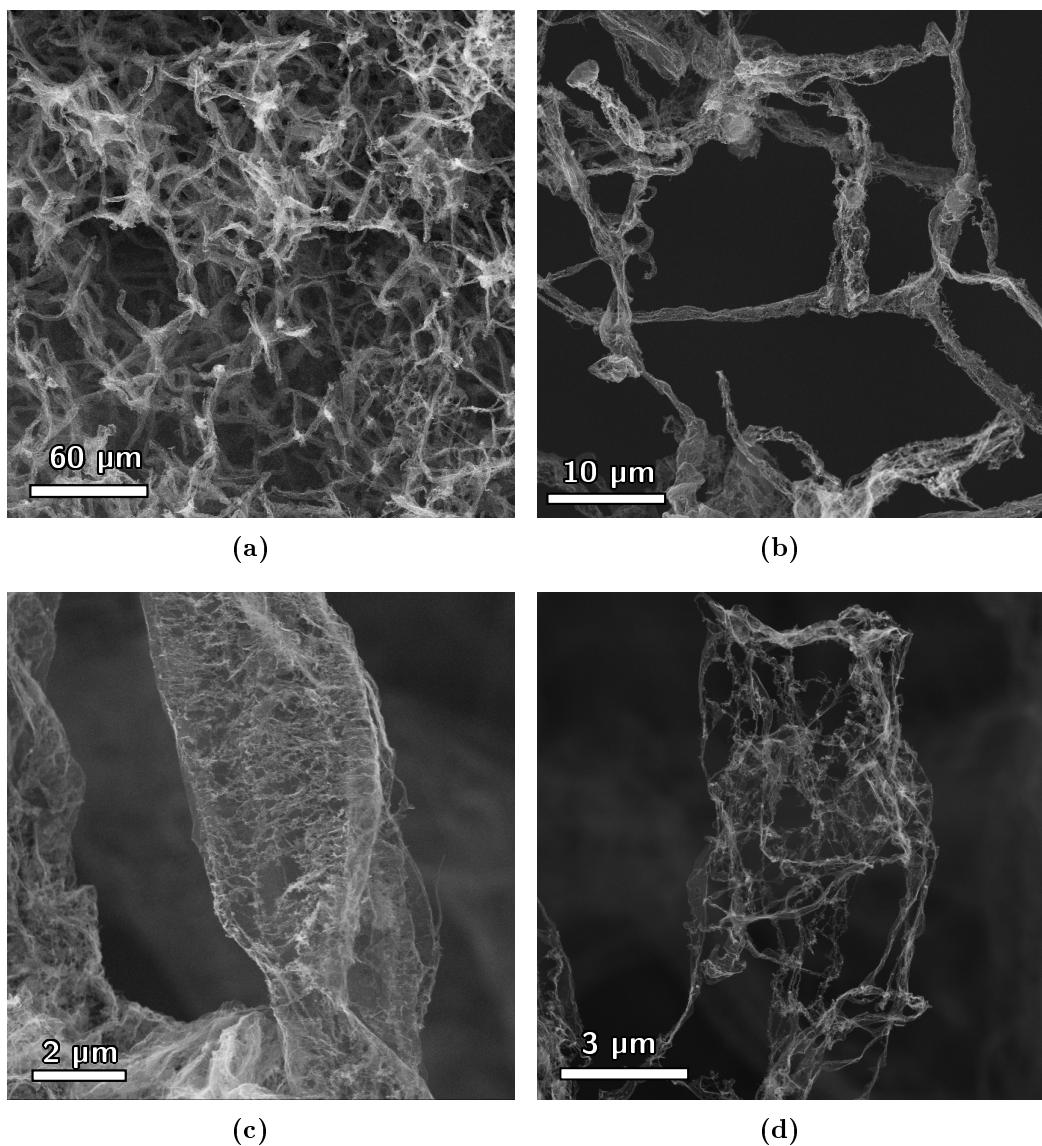


Figure 9.2: SEM micrographs of the hollow framework variant of Aerographite. a) Network of the hollow framework variant. The shape of the distorted tetrapods is still recognizable. b) Magnified view on highly porous network. c),d) The open and porous structure of the individual tubes consists of carbon ribbons.

hierarchical network of this variant which is made up by a hollow framework of ribbons. These ribbons consist of a transition state of mostly sp^2 hybridized carbon and glass-like carbon [31] which is in consistence with the electrical conductivity of the hollow framework variant.

The density of this variant goes down to $180 \mu\text{g}/\text{cm}^3$ which means, that the hollow framework variant is the second lightest solid cellular material known in literature [26]. Further, it is also possible to synthesize variants, with a filling of the tubes, from amorphous carbon [31] but these variants are beyond the scope of this thesis.

9.2. Atomic Structure of Aerographite

The tunable and decisive parameters for the synthesis of Aerographite are the temperature profile and the toluene injection rate in the CVD process as well as the chemical purity of the employed ZnO templates and atmosphere of the CVD reactor. The presence of impurities in the CVD process can catalyze the growth of amorphous carbon which suppresses the formation of Aerographite because the provided carbon is consumed by the growth of the amorphous carbon.

Figure 9.3(a) shows a bright field TEM image and Figure 9.3(b) the corresponding selected area electron diffraction (SAED) pattern of the closed shell variant of Aerographite (synthesis parameters in Figure 5.5). The SAED pattern exhibits diffuse rings with the respective d-values of 2.1 nm , 1.2 nm and 1.07 nm . These experimental d-values match the reference values of graphite with the space group $P6_3/mmc$ and can be assigned to the miller indices (100) , (110) and (020) , respectively [36]. In general, the presence of the diffuse rings in the SAED pattern indicates a polycrystalline nature of the material. However, a complete polycrystalline character can be excluded due to the absence of the 002 Bragg reflection in Figure 9.3(b), which possesses the highest expected intensity according to the kinematic theory [36]. The observed set of Bragg reflections suggest only one viewing direction, namely the $[001]$ zone axis. This indicates a parallel alignment of the graphitic layers along the $[001]$ zone axis with an individual rotation of the layers similar to turbostratic graphite [40, 94–96]. This is verified by a simulated SAED pattern of graphitic layers rotated perpendicular to the $[001]$ zone axis (see right side of Figure 9.3(b)). Figure 13.3 shows the X-ray diffraction (XRD) pattern of

the closed shell variant of Aerographite. The XRD pattern shows the 002, the 100 and the 110 peak which again confirms the graphitic structure of the closed shell variant. The 002 reflection was also observed in the SAED pattern but exclusively at the edges of the tubes because of the fulfilled Bragg reflection condition.

A comparison between an experimentally obtained EELS spectrum for the closed shell Aerographite with a graphite reference spectrum [97] is demonstrated in Figure 9.4a. Within the experimental data two pronounced peaks can be identified, coinciding with the π^* and σ^* peaks from the reference spectrum and occurring due to the sp^2 hybridization of carbon.

For the π^* peak intensity and the fine structure a considerable deviation between the two data sets is present. As the fine structure of EEL spectra is sensitive to the specimen thickness it can be suggested that the information, shown within the reference spectrum, is obliterated due to this thickness effect. This assumption is supported by the strongly pronounced hump beyond the σ^* peak, which is a typical indication for a high thickness. Note, in the case of EELS term 'high thickness' can already been used starting from 40 nm. [98]

The same comprehensive study is performed for the hollow framework variant of Aerographite, see Figure 9.3(c)c, d and Figure 9.4b. For the structural analysis, electron diffraction is carried out on a representative region depicted in Figure 9.3(c)c. The corresponding SAED pattern exhibits only diffuse intensities correlating with a purely amorphous structure. This finding is in good agreement with the EEL spectrum obtained from the same area (Figure 9.4b) which shows only the π^* peak as typical characteristic of amorphous carbon.

The hollow framework variant of Aerographite possesses an electrical conductivity of 0.2 S/m (see chapter 12.1), therefore it can be assumed that a high percentage of the carbon is sp^2 hybridized. It can be speculated, that the atomic structure of the hollow framework variant is made up by a transition state of amorphous carbon and glass like carbon [31].

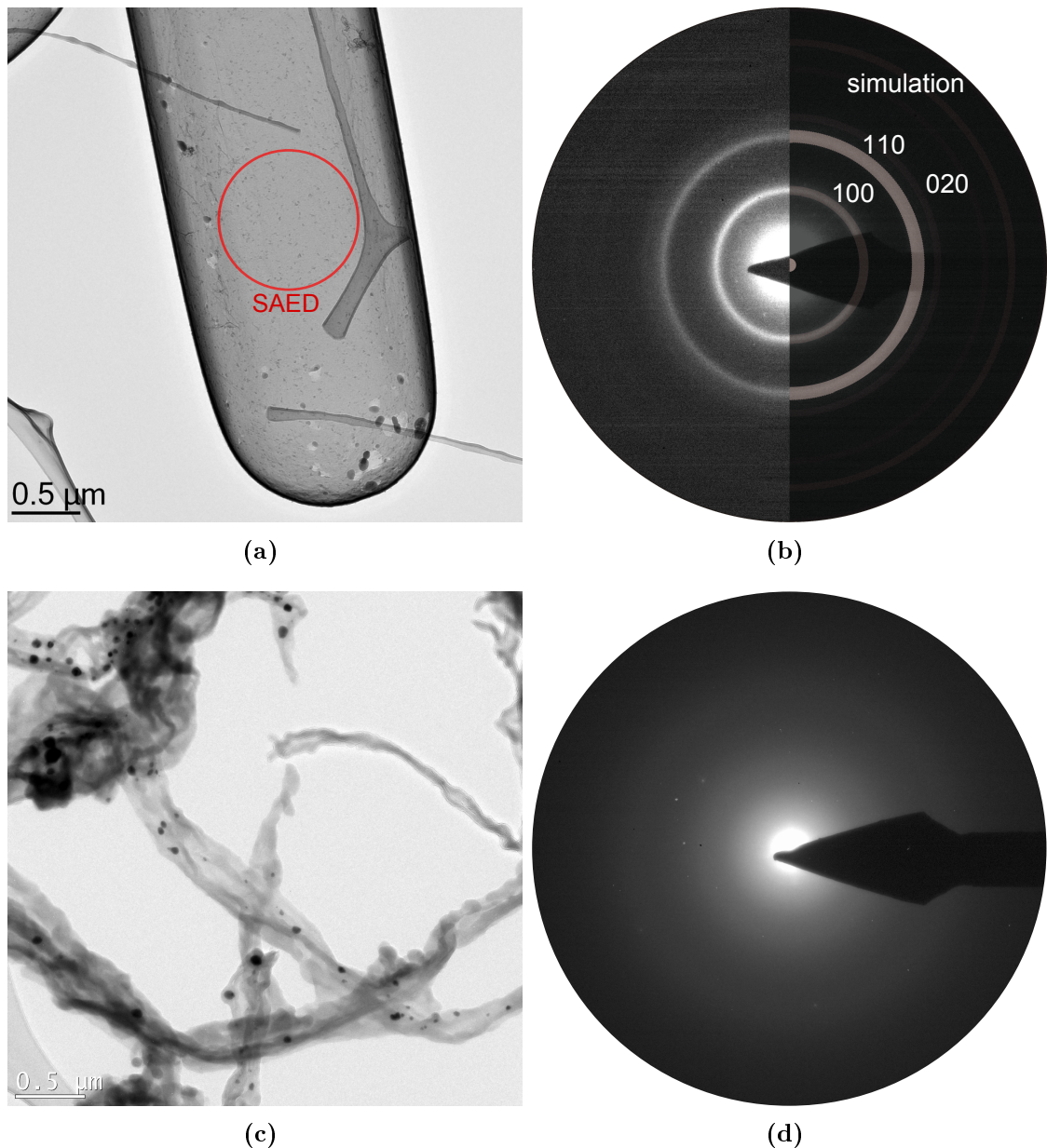


Figure 9.3: a) TEM bright field image of an Aerographite tube with closed walls. The selected area electron diffraction (SAED) was performed at the marked position. b) SAED pattern of the closed shell variant of Aerographite. The right side of the image shows the corresponding simulation for graphitic layers rotated perpendicular to the [001] zone axis. c) TEM bright field image of the hollow framework variant of Aerographite. d) SAED pattern of the hollow framework variant of Aerographite.

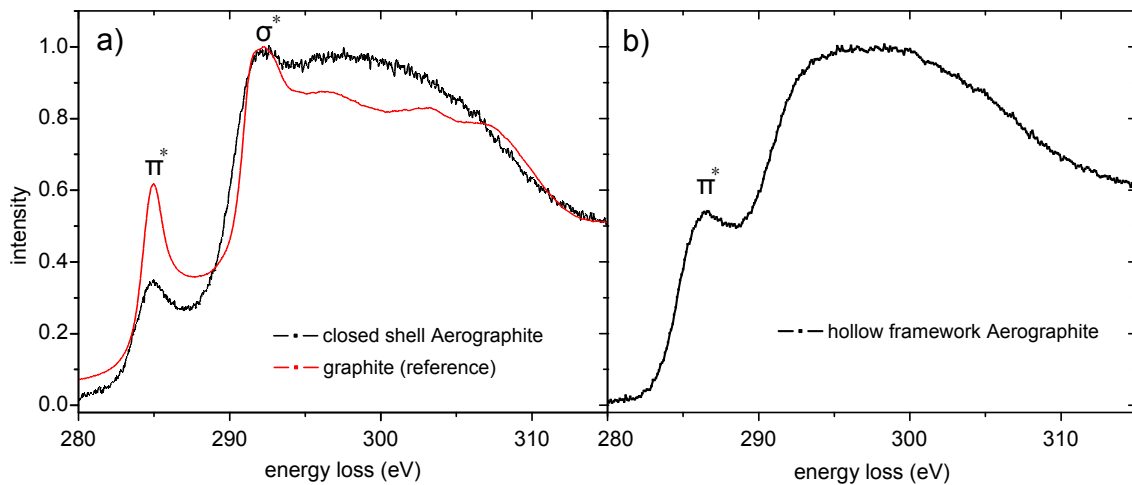


Figure 9.4: a) Electron energy loss spectrum of the closed shell variant of Aerographite. The red spectrum is a reference spectrum for graphite [97]. b) Electron energy loss spectrum of the hollow framework variant of Aerographite.

10. Mechanical In Situ Experiments of Aerographite

In this chapter the experimental results from the mechanical in situ measurements of individual Aerographite structures are discussed. The experimental techniques for this measurements are discussed in 6.2. On the basis of this results, an elastic model for the stress strain response of Aerographite bulk networks is derived and compared with the experimental data from the compression tests of Aerographite bulk networks.

10.1. In Situ Deflection of Individual Aerographite Tetrapod Arms

The tetrapod arms were bent by an atomic force microscope (AFM) cantilever which deflection was measured. For the evaluation of this data it was necessary to determine the real arm length and deflection of the cantilever because in the recorded images just the projection of both is visible. Therefore the tilting angle of the tetrapod arm and the cantilever with respect to the optical axis of the SEM was calculated.

For the AFM cantilever the total length is known and the tilting angle was determined by *equation (10.1)* where L_{total} denotes the total length of the cantilever and $L_{projected}$ denotes the projected length of the cantilever which is visible in the SEM micrograph.

$$\alpha = \arcsin\left(\frac{L_{projected}}{L_{total}}\right) \quad (10.1)$$

The same formula holds for the tilting angle of the tetrapod arm but in this case it was necessary to determine the total length of the tetrapod arm first. In order to determine this length, a series of SEM micrographs with different tilting angles of the SEM stage was recorded. By plotting the projected length of the tetrapod arm against the tilting angle of the stage and the application of a sinusoidal curve fit, the total arm length was determined. Subsequently the angle of the AFM cantilever relative to the tetrapod arm and the torque which acted on the tetrapod arm was calculated. The torque τ is the vector product of the displacement vector \vec{r} and the force vector \vec{F} (see *equation* (10.2)).

$$\tau = |\vec{r}| |\vec{F}| \sin(\theta) \quad (10.2)$$

In the calculations, the displacement vector \vec{r} was defined as the connection line between the basis at the tetrapod junction and the contact point with the AFM cantilever tip. This means, the torque is supposed to attack at the point where the tetrapod arm is attached to the junction and not at the center of the tetrapod. The reason for this data evaluation was the observation, that the tetrapod junction gets distorted during the bending.

Figure 10.1(a) shows an example of the experimental setup of a tetrapod and the approached AFM cantilever. Figure 10.1(b) depicts the corresponding measurement of the applied torque during the deflection of the tetrapod arm. With increasing deflection of the tetrapod arm the torque increases almost linear which is supported by the observed deformation behavior. It was observed, that the tetrapod arm was very rigid while the junction of the tetrapod was deformed. This means the deflection of the arm is mainly caused by the deformation of the junction while the bending of the arm is not as pronounced.

A second example for the slight bending of an Aerographite tetrapod arm is presented in Figure 10.2. This measurement indicates some slight decrease in the stiffness because the slope of the graph gets smaller with increasing deflection angle. This effect can be related to the onset of some buckling of the tetrapod arm at

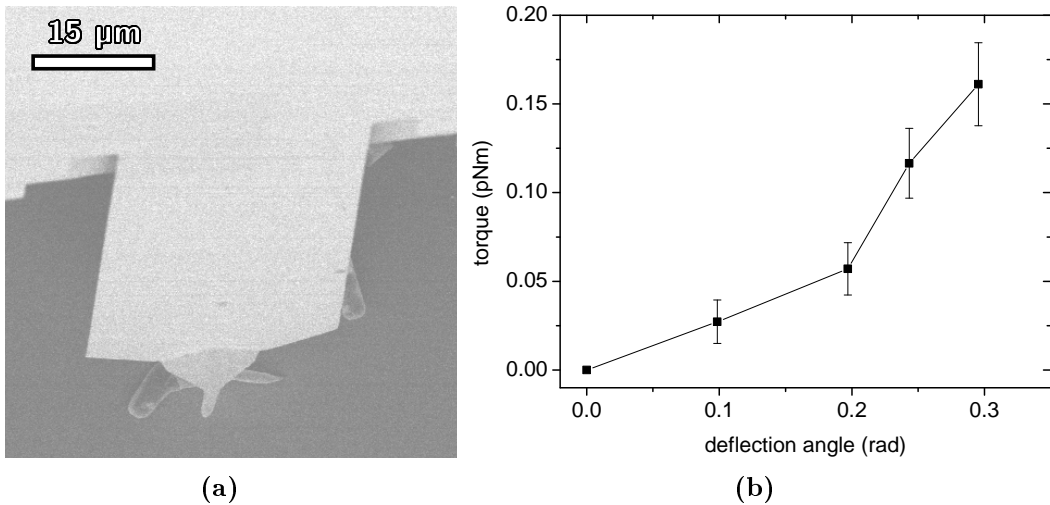


Figure 10.1: a) SEM micrograph of an individual Aerographite tetrapod on a silicon wafer. The free standing arm of the tetrapod was bent by an AFM (atomic force microscopy) cantilever. b) From the deflection of the cantilever, the applied force and torque were calculated and plotted versus the deflection angle. The corresponding "spring constant" of the tetrapod arm is listed in table 10.1.

the junction. In the in situ experiments it was observed, that Aerographite tubes can be reversibly buckled without obvious damage (see chapter 11.3). When the arm or the junction starts to buckle, the stiffness is significantly lowered [99]. To examine this effect, the tetrapod in Figure 10.3 was deflected to a higher deflection angles of 0.6 rad . The curve shows some flattening for higher deflection angles which could be related to the buckling of either the arm or the junction. The linear bending and the buckling of the tetrapod junctions was also simulated by the finite element method(FEM) by Prof. Nicola Pugno from the University of Trento, Italy. This simulations showed good agreement with the experimentally observations and support the theory of buckling at the junctions. In comparison to the other bending experiments the curvature of the graph from Figure 10.1(b) represents an exception because it shows no "buckling". One explanation for this, is a ZnO filled tetrapod junction which prevents any buckling. This can be the case if the ZnO was not removed completely during the CVD process.

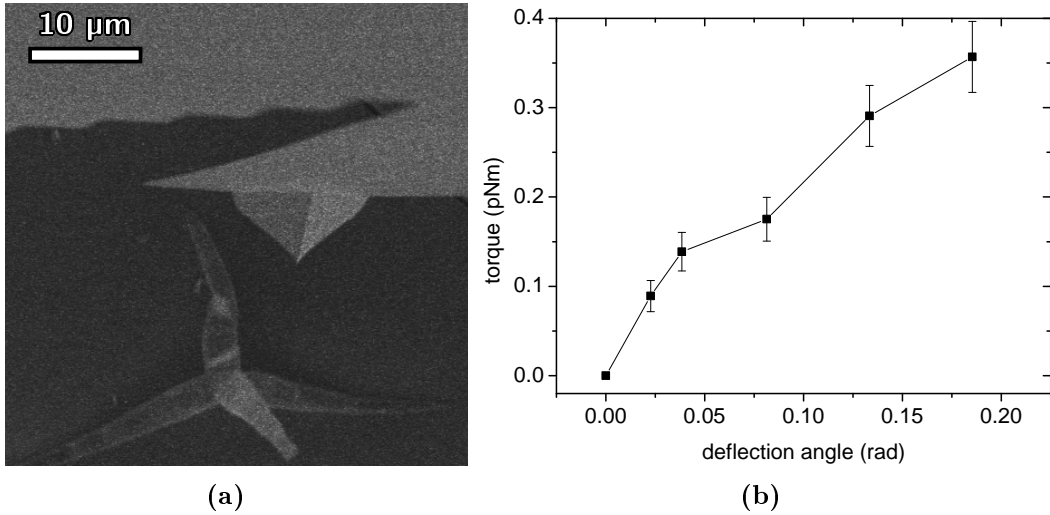


Figure 10.2: a) SEM micrograph of an individual Aerogel tetrapod on a silicon wafer. The free standing arm of the tetrapod was bent by an AFM (atomic force microscopy) cantilever. b) From the deflection of the cantilever, the applied force and torque were calculated and plotted versus the deflection angle. The corresponding "spring constant" of the tetrapod arm is listed in table 10.1.

The tetrapod in Figure 10.4 possesses a much higher stiffness as presented in table 10.1. This can be attributed to a higher wall thickness of the tetrapod arms and the junction which causes a higher stiffness. With increasing wall thickness also the tendency for buckling is smaller. However, it has to be considered that the stiffness can deviate depending upon the bending direction of the free standing arm with respect to the remaining tetrapod arms. This parameter was not studied in the in situ experiments because of the limited number of experiments.

During all performed bending experiments, the observed curvature of the tetrapod arms was negligibly small with respect to the distortion of the tetrapod junction. This means, that the tetrapod arm is significantly stiffer than the tetrapod junction. Consequently an applied torque causes a rotation of the tetrapod arms around their junctions.

This mechanism strongly influences the mechanical behavior of the Aerogel network when an external force is applied. The deformation of the entire network is

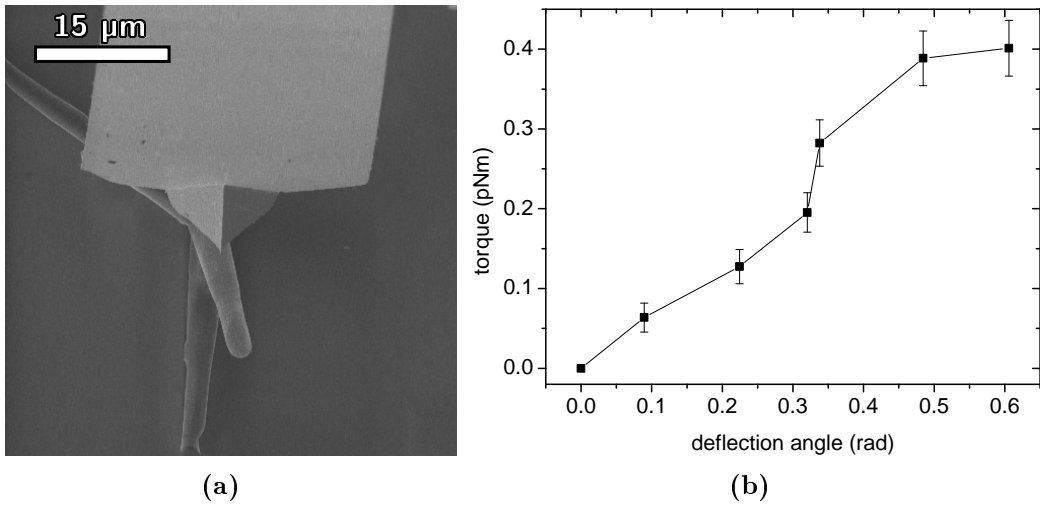


Figure 10.3: a) SEM micrograph of an individual Aerographite tetrapod on a silicon wafer. The free standing arm of the tetrapod was bent by an AFM (atomic force microscopy) cantilever. b) From the deflection of the cantilever, the applied force and torque were calculated and plotted versus the deflection angle. The corresponding "spring constant" of the tetrapod arm is listed in table 10.1.

Table 10.1: Torsion spring constants measured in the *in situ* experiments at single tetrapod arms.

figure	spring constant D (pNm/rad)	estimated wall thickness (nm)
10.1	0.5	15-20
10.2	1.8	15-20
10.3	0.7	15-20
10.4	25	higher than 20

realized by a rotation of the tetrapod arms around their junctions while the tetrapod arms behave relatively rigid. It can be expected that the contribution from the bending of the tetrapod arms is very small with respect to the rotation of the arms around their junctions. This assumption was supported by numerical simulations from Prof. Nicola Pugno from the University of Trento, Italy. This characteristic deformation behavior was also observed in the SEM for the indentation of an Aerographite network by a tungsten tip. Based on this observations the deformation of

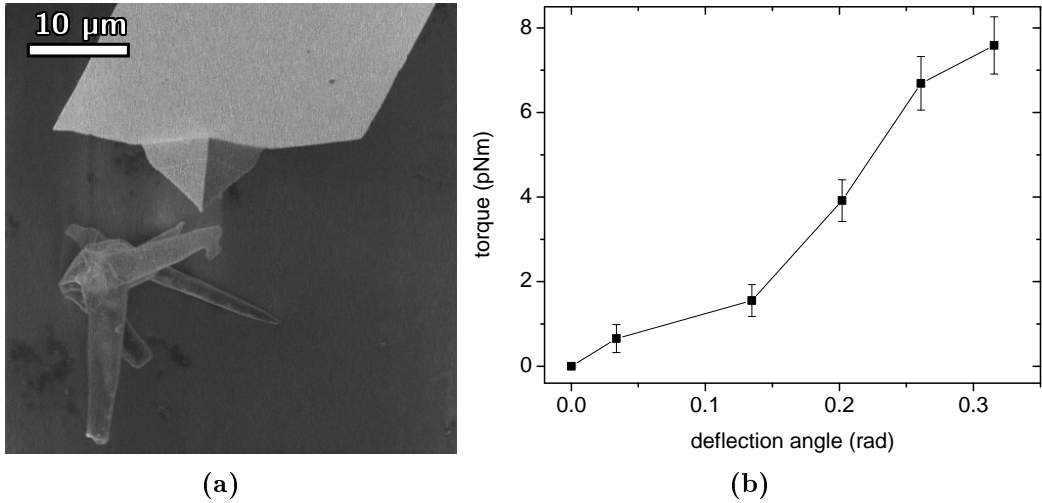


Figure 10.4: a) SEM micrograph of an individual Aerographite tetrapod on a silicon wafer. The free standing arm of the tetrapod was bent by an AFM (atomic force microscopy) cantilever. b) From the deflection of the cantilever, the applied force and torque were calculated and plotted versus the deflection angle. The corresponding "spring constant" of the tetrapod arm is listed in table 10.1.

Aerographite was modeled by an ensemble of torsion springs (tetrapod junctions) which are interconnected with rigid struts (tetrapod arms).

Table 10.1 gives an overview of the measured slopes of the torque/deflection curves according to *equation (10.3)* and the estimated wall thickness of the tetrapods. These experimental parameters find application as torsion spring constant D in the elastic model for the Aerographite networks in chapter 10.2.

10.2. Elastic Model for Aerographite Networks

On the basis of the results from the in situ bending experiments a theoretical mechanical model was derived. This model allows the calculation of the Aerographite bulk modulus from the stiffness of individual tetrapod junctions (measured in the in situ experiments) and the geometry of the tetrapods. The model is based on the assumption that the deformation of the Aerographite network is caused by a rotation of the tetrapod arms around their junctions while the tetrapod arms behave rela-

tively rigid. This appears reasonable for small densities and small to intermediate deformation regimes.

The model includes the following assumptions and simplifications:

- The bending of the tetrapod arms around their junctions is described by linear elastic behavior.
- There occurs no buckling of the tetrapod junctions or arms.
- The bending induced curvature of the tetrapod arms can be neglected.
- The densification effect of the network during compression can be neglected.

The spring constant D for the deflection of an individual tetrapod arm was determined by a linear curve fit of the torque in dependence of the deflection angle α (see *equation (10.3)*). An overview of the experimental results for the in situ bending tests at individual tetrapods is given in table 10.1.

$$D = \frac{\Delta\tau}{\Delta\alpha} \quad (10.3)$$

The torque which acts on the tetrapod arm can be calculated by *equation (10.2)*. The vector \vec{r} represents the orientation and length of the tetrapod arm while the vector \vec{F} represents the external force which attacks at the tip of the arm like depicted in Figure 10.5. The deflection angle $\Delta\alpha$ for the application of a certain torque is given by *equation (10.4)*.

$$\Delta\alpha = \frac{\tau}{D} \quad (10.4)$$

Combination of *equation (10.2)* and *equation (10.4)* results in *equation (10.5)*.

$$\Delta\alpha = \frac{1}{D} |\vec{r}| |\vec{F}| \sin(\alpha) \quad (10.5)$$

The height h of the triangle which is made up by the tetrapod arms, like depicted

in Figure 10.5 can be calculated by *equation* (10.6).

$$h = \cos(\alpha) |\vec{r}| \quad (10.6)$$

According to *equation* (10.6) does an angular change $\Delta\alpha$ of the tetrapod arm

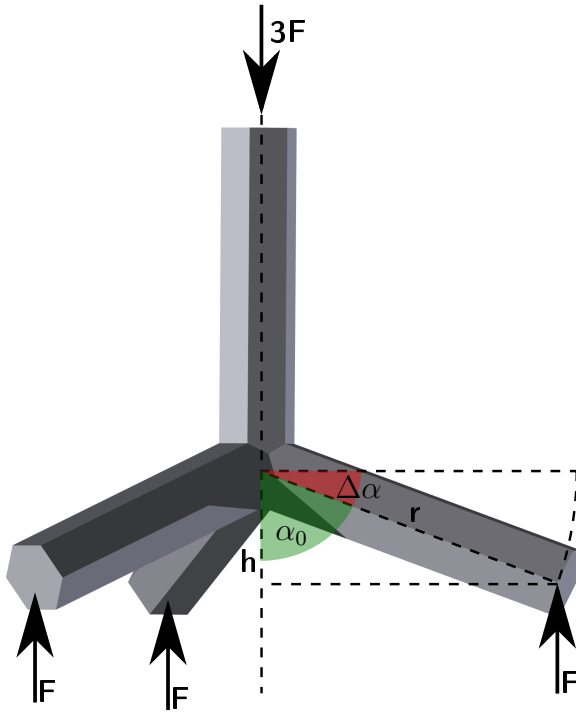


Figure 10.5: Schematic drawing of an Aerographite tetrapod under load. Due to the force $|\vec{F}|$ the tetrapod arm will get deflected by an angle $\Delta\alpha$ like indicated in the drawing. This leads to a change of the height h in the depicted triangle.

causes a change of the height Δh of the tetrapod which can be calculated by *equation* (10.7). h_0 denotes the initial height of the tetrapod and α_0 is the corresponding angle in the undeformed state.

$$\Delta h = h_0 - \cos(\alpha_0 + \Delta\alpha) |\vec{r}| \quad (10.7)$$

The normalized change in height ϵ of the tetrapod can be calculated by *equation* (10.8).

$$\epsilon = \frac{h_0 - \cos(\alpha_0 + \frac{1}{D} |\vec{r}| |\vec{F}| \sin(\alpha)) |\vec{r}|}{h_0} \quad (10.8)$$

By inserting *equation* (10.6) into *equation* (10.8) one gets *equation* (10.8).

$$\epsilon = 1 - \frac{\cos(\alpha_0 + \frac{1}{D}|\vec{r}| |\vec{F}| \sin(\alpha))}{\cos(\alpha_0)} \quad (10.9)$$

In the mechanical model, it is assumed that the externally applied force, is dis-

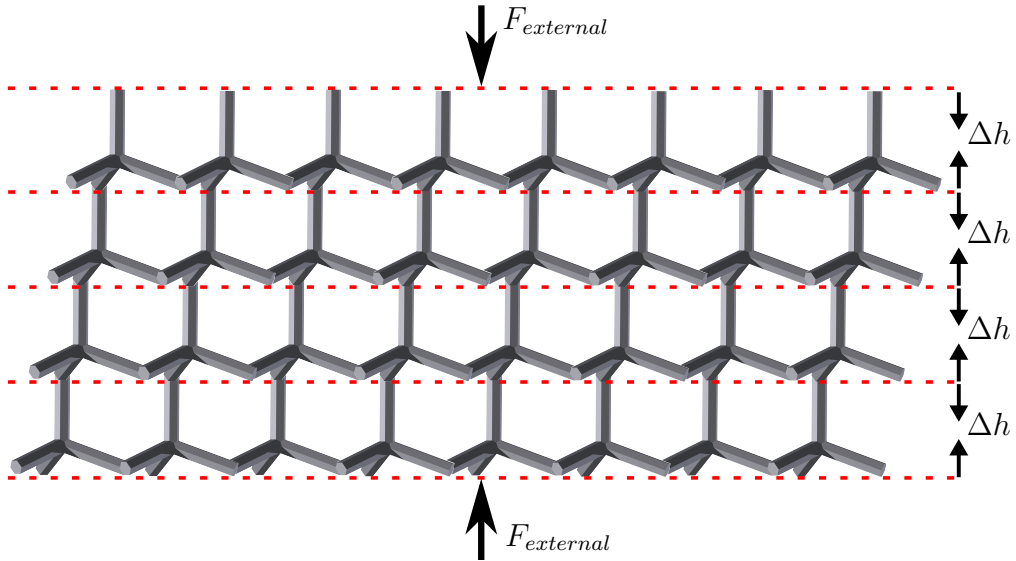


Figure 10.6: Schematic drawing of an Aerographite tetrapod network under some external load. The applied force is assumed to be distributed to a layer of tetrapods which gets compressed by a change Δh according to *equation* (10.7). Due to the serial arrangement of the individual layers, each layer experiences the same force and thus the same compression.

tributed to all tetrapods of a single layer of the Aerographite bulk sample. This means, that the Aerographite tetrapods are regarded as an ensemble of springs which are connected in parallel inside a single layer. These layers are all exposed to the same external force as they are assumed to be connected in a serial manner like depicted in Figure 10.6. Therefore, the force which acts on a single tetrapod is just the fraction of the externally applied force $|\vec{F}_{ext}|$ and the number of tetrapods in one layer of Aerographite like calculated in *equation* (10.10) where n denotes the number of tetrapod arms per area element a and A is the cross sectional area of the sample. The factor n determines how strong the tetrapods interleave in the

network and is named interleaving factor in the following.

$$|\vec{F}| = \frac{a|\vec{F}_{ext}|}{nA} \quad (10.10)$$

The area element a in *equation* (10.10) is just the triangular projection of a single tetrapod and is connected to the length of the tetrapod arm by *equation* (10.11).

$$a = \sqrt{3}(\cos(\frac{\alpha_0}{2})|\vec{r}|)^2 \quad (10.11)$$

By inserting *equation* (10.10) and *equation* (10.11) into *equation* (10.9) one obtains *equation* (10.12). The fraction of the external force F_{ext} and the cross sectional area A has been replaced by the compressive stress p .

$$\epsilon = 1 - \frac{\cos(\alpha_0 + p|\vec{r}|^3 \frac{1}{nD} \cos^2(\frac{\alpha_0}{2})\sqrt{3}\sin(\alpha))}{\cos(\alpha_0)} \quad (10.12)$$

By reformulating *equation* (10.12) one gets *equation* (10.13) the compressive stress p as a function of the deformation state.

$$p = \frac{nD(\arccos((1-\epsilon)\cos(\alpha_0)) - \alpha_0)}{|\vec{r}|^3 \cos^2(\frac{\alpha_0}{2})\sqrt{3}\sin(\alpha)} \quad (10.13)$$

The shape of the Aerographite tetrapods is adopted from the original ZnO template. The inter-arm angles of a ZnO tetrapod most often deviate from an ideal tetrapod due to mismatch in the tetrapod nucleus [88]. The real inter-arm angles of an ZnO tetrapod depend upon the way how the misfit strain in the nucleus is relaxed. This results in number of different sets of the inter-arm angles which can reach from 99° to 140.2° [88].

However, in the mechanical model exclusively one inter-arm angle is inserted and for reasons of simplification the angle between two tetrapod arms was assumed with 109.5° resulting in an angle α equal to 70.5° as depicted in Figure 10.5. A detailed study of the ZnO tetrapod arm angles is part of the PhD thesis from Ingo Paulowicz [89].

In the calculations for the mechanical model, the initial angle of α_0 was set to a

maximum value 70.5° or smaller. This includes the simplification that all tetrapods of one layer are oriented in the same direction with respect to the external applied force. In the real Aerographite samples the situation is more complex and the tetrapods are oriented randomly in the entire network. During the deformation of the tetrapods, the angle α will start from the initial angle α_0 and increases during compression. This causes an increase of the torque which is acting on the tetrapod arms. In the calculations this effect was described in an iterative manner and the angle change $\Delta\alpha$ was calculated by inserting the experimentally measured force in *equation (10.5)*.

The interleaving factor n is assumed to be equal to 3 or higher which is based on the assumption that each tetrapod contributes at least with 3 arms per area element to the stiffness. This means for $n > 3$, the tetrapods interleave in the network and there is more than one tetrapod present per area element.

The model does not consider any cross links between the arms of the tetrapods due to the assumption that the tetrapods of one layer do not interact during the deformation. In the real Aerographite network these crosslinks are present and will cause an additional reinforcement of the network which should result in a higher modulus of the bulk measurements than predicted by the mechanical model. As already mentioned, is the deflection of the tetrapod arms due to bending neglected in the model. This simplification appears valid under the geometric aspect of the tetrapod arms. The diameter of the tubes is very large with respect to the length of the tubes. This means that the tubes are very stiff and this explains why there was no bending observed in the in situ experiments.

A further limitation of the model will occur for very strong deformations of the network. Like discussed in chapter 11.2, by overcoming a certain maximum torque the tubes inside the Aerographite network start to buckle which causes a instantaneous loss of their stiffness. In the in situ experiments two different cases of buckling were observed, either the tetrapod arm started to buckle close to the tetrapod junction or even the junction itself buckled. In both cases the stiffness of the tetrapod arm will

be lowered instantly but due to the random angular distribution of the tetrapods, just a small percentage of the tetrapods will buckle. For strong deformations the ratio of buckled tetrapods will increase further more which can cause a deviation from the linear elastic behavior in the bulk measurements.

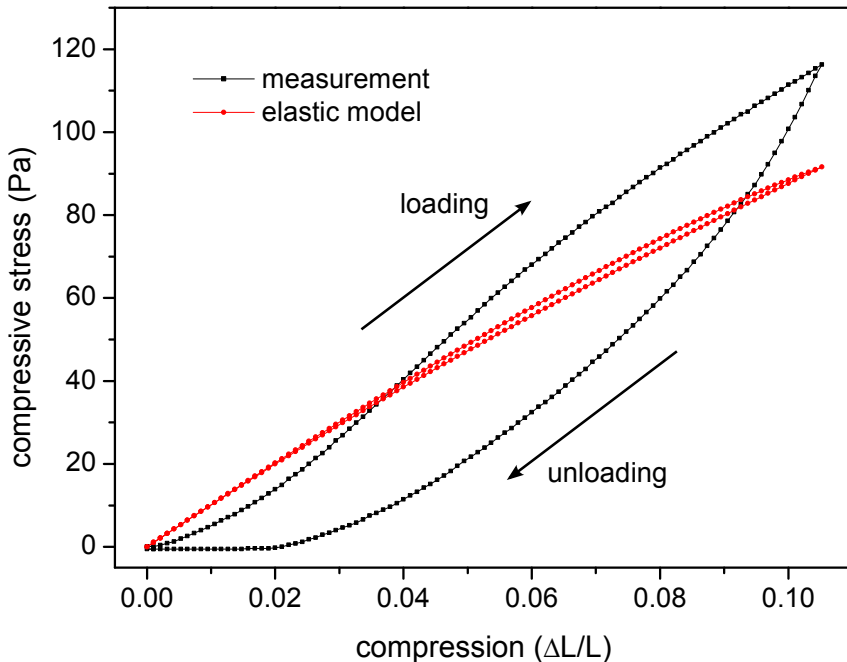


Figure 10.7: Compression measurements at a bulk Aerographite network with a density of 1.8 mg/cm^3 . The red curve indicates the compressive stress which was calculated by the elastic model with an initial angle of $\alpha_0 = 45^\circ$, a spring constant $D = 1.2 \text{ pNm/rad}$, a tetrapod interleaving factor of $n = 3$ and an effective tetrapod arm length of $|\vec{r}| = 15 \mu\text{m}$. The sample was from the same type of Aerographite as *in situ* measured for the spring constant.

Figure 10.7 shows the bulk measurement and the corresponding calculated stress of an Aerographite network with a density of 1.8 mg/cm^3 under compressive load. The calculation was carried out according to *equation (10.13)*. The parameters for the calculation of the stress were set to an initial angle of $\alpha_0 = 45^\circ$, a spring constant of $D = 1.2 \text{ pNm/rad}$ and a tetrapod interleaving factor of $n = 3$. For this type of Aerographite, the spring constant D was determined by the *in situ* measurements. In *equation (10.13)* it can be seen that the effective tetrapod arm length strongly influences the compressive stress for a given deformation. The effective length of

the tetrapod arms was set to $|\vec{r}| = 15 \mu\text{m}$ which is about half of the free length of the tetrapod arms (observed in the SEM). The reason for this is, the low probability that all tetrapod arms are just interconnected at their tips, due to their random distribution in the network. Up to 3.5% compression, the measured stress lies below the calculated stress. This deviation can be caused by the surface roughness of the sample which has to be flattened until a complete mechanical contact is established. With further compression, the measured stress overcomes the calculated ones. One explanation for this, is the compression induced increase in packing density of tetrapods resulting in higher stiffness which is not considered in the model. Further, it can be observed that for deformations above 6% the curvature of the measured stress changes and the modulus (slope of the graph) decreases. One explanation for this behavior could be some buckling of tetrapod arms or junctions which softens the network. The reversible buckling of Aerographite tubes is analyzed in chapter 11.3.

Figure 10.8 shows the compression test of an Aerographite network with a density of 3 mg/cm^3 . The red curve was calculated with an initial angle of $\alpha_0 = 45^\circ$, a spring constant of $D = 2.9 \text{ pNm/rad}$, a tetrapod interleaving factor of $n = 3$ and an effective tetrapod arm length of $|\vec{r}| = 15 \mu\text{m}$. The spring constant of $D = 2.9 \text{ pNm/rad}$ is higher than the experimental observed values (see 10.1) but this is reasonable because of the relatively high density of the network with 3 mg/cm^3 . A higher toluene injection rate during the CVD process of the Aerographite, results in thicker graphitic walls and thus in a higher network density. For thicker graphitic walls one can assume a higher stiffness of the tetrapod junctions resulting in a higher spring constant of the tetrapod arms.

For the applied parameters, the model coincides almost precisely with the experimental stress curve. For deformation states above 2% this sample showed the same flattening of the stress curve like the sample shown in Figure 10.7. In the model this is considered by the rotation of the tetrapod arms which leads to an increase of the applied torque. This results in a smaller modulus of the tetrapod network

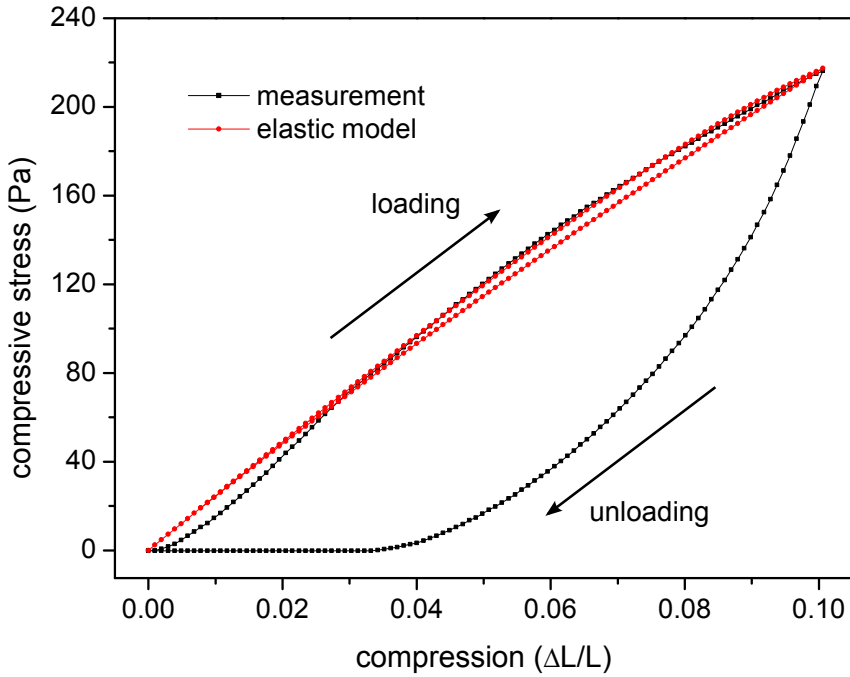


Figure 10.8: Compression measurements at a bulk Aerographite network with a density of 3 mg/cm^3 . The red curve indicates the compressive stress which was calculated by the elastic model with an initial angle of $\alpha_0 = 45^\circ$, a spring constant $D = 2.9 \text{ pNm/rad}$, a tetrapod interleaving factor of $n = 3$ and an effective tetrapod arm length of $|\vec{r}| = 15 \mu\text{m}$.

for higher deformation states. It can be speculated that a similar process occurs in the real Aerographite network.

It can be assumed, that for small compression states just a fraction of the tetrapod arms change their angular orientation in the network because not all tetrapod arms are connected or in touch. For stronger compressions the number of defected tetrapod arms will increase. For highly compressed networks the tetrapods arms are oriented perpendicular to the external force which maximizes the torque. This mechanism as well as the buckling of tetrapods makes the network softer. One mechanism which acts against this softening is the increasing packing density of the tetrapods by the compression. For strongly compressed networks this results in an steep increase of the stress in the densification region.

The biggest difference between the real tetrapod networks and the network geometry assumed in the elastic model, is the random orientation of the tetrapods in the real

network. It is important to mention, that the proposed elastic model is just an approximation for an idealized tetrapod network which does not match the tetrapod arrangement in the real Aerographite. However, the randomized orientation of the tetrapods is not considered in the model because the most important parameter is the stiffness of the tetrapod junctions which is orientation independent. The influence of the tetrapod randomization must be elaborated in future work.

The model proves the consistence of the data from the situ measurements with the results from mechanical bulk tests. The model just describes the elastic properties of Aerographite. For the plastic deformation or a visco-elastic contribution it is inappropriate. These properties are discussed in chapter 11.2. In the appendix the modeling of one more compression measurement is shown in Figure 13.4.

11. Mechanical Properties of Bulk Aerographite

In this chapter the mechanical properties of bulk networks of Aerographite are discussed. First, the characteristic stress response for strong compression states will be discussed and compared with an ideal bending dominated lattice. Further, the properties of the Aerographite hollow framework variant under tensile load and the position of Aerographite in the Ashby material selection map will be discussed. Also the cyclic stiffening and the visco-elasticity of Aerographite will be discussed.

In chapter 3.2 the characteristic behavior of an ideal bending-dominated lattice was discussed. At the beginning of the compression an ideal bending-dominated lattices shows a linear elastic response which is followed by a region of plastic deformation at constant stress (see Figure 3.5). The mechanism behind this behavior is the buckling or crushing of individual cells inside the network. With further compression, the stress increases rapidly because the lattice is strongly densified and the opposing sides of the unit cells start to impinge resulting in a steep increase of the stress in this region of the stress (compressive) strain curve.

Figure 11.1 shows a compression test of an Aerographite sample with a density of 2.2 mg/cm^3 up to 30 % compression. The stress response of the sample can be divided into 3 different regions which are separated by two points of inflection (indicated by the dashed line). This means the curvature of the stress curve changes twice during the compression (indicated in red and green). In the first region, the stress increases progressively, which can be explained by an increasing number of contact points between the surface of the sample and the mechanical contact area of

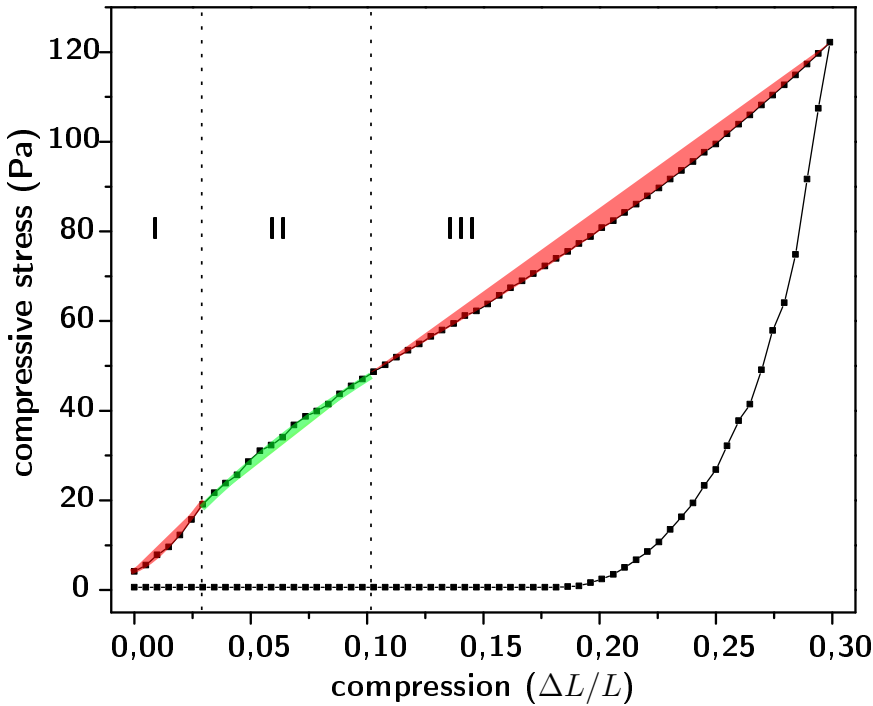


Figure 11.1: Compression test of an Aerographite sample with a density of 2.2 mg/cm^3 . The stress response of the sample can be divided into 3 different regions which are separated by two points of inflection (indicated by the dashed line). In the first region, the stress increases progressively due to an increase of the effective mechanical contact area. In the second region the onset of plasticity can be observed (buckling or crushing of tetrapods). In the third region the stress increases faster because of the densification of the network.

the setup. The surface roughness of the sample induces higher stresses at exposed tetrapod structures until they collapse and neighboring tetrapods approach the mechanical contact. This can explain the non linear shape of the stress/strain curve in the first region of Figure 11.1.

In region two, the slope gets smaller indicating the onset of plasticity of the network. There are probably two major contributions for the plastic deformation in the Aerographite network. First, plastic deformation can occur by buckling or crushing of tetrapods. Second, it was investigated in the in situ experiments that individual tetrapods adhere easily to each other by Van der Waals forces. This means, that with proceeded compression, additional network junctions can form which pin the network in the deformed state. In the mechanical measurements, this mechanism

can not be discriminated from the normal plastic deformation.

With further compression, the curvature changes again and the stress increases progressively in the third region. This indicates the onset of the densification stress like for an ideal bending-dominated lattice. In contrast to an exclusively bending dominated lattice the sample showed no stress plateau in the third region. This is not surprising in consideration of the random distribution of the tetrapods and other building elements (rods/struts and sheets) in the network. It is very unlikely, that the whole network consists exclusively out of bending dominated unit cells rather than mixture of bending and stretch dominated cells.

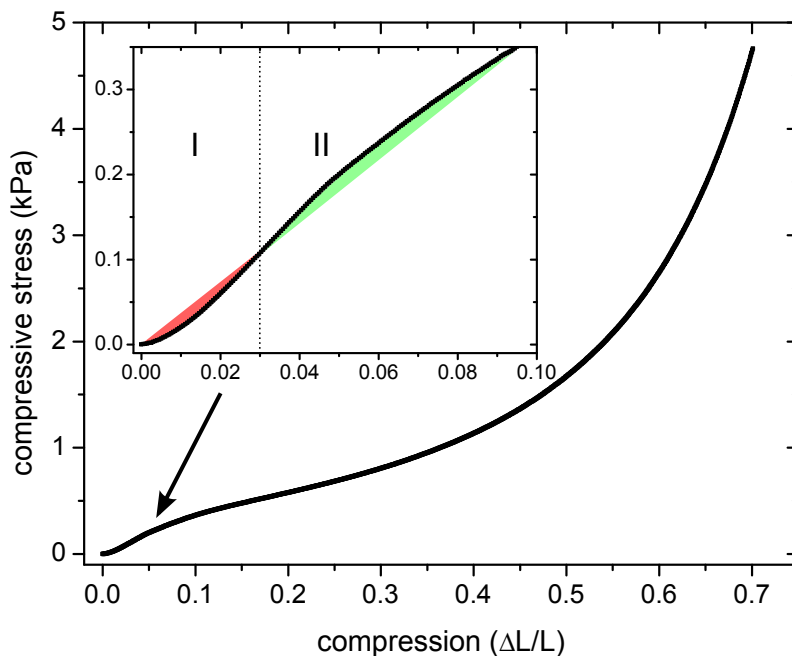


Figure 11.2: Compression test of an Aerographite network with a density of 3.84 mg/cm^3 density. The inset shows a magnified view of the deformation region up to 10 %.

To examine the stress increase in the densification region, a compression experiment of an Aerographite network of 3.84 mg/cm^3 density up to 70 % compression was conducted (shown in Figure 11.2). This measurement shows the same three characteristic deformations regions like discussed for Figure 11.1. The inset in Figure 11.2 shows a magnified of the deformation region one and two. In the densification

region the stress increased to a maximum value of 4.8 kPa for 70 % compression. The integral over the stress strain curve from 0 to 70 % compression gives a specific energy of 0.94 kJ/m^3 . In consideration of the sample volume of 0.7 cm^3 , this results in a absolute deformation energy of 0.66 mJ and with respect to the sample mass of 2.69 mg in 0.245 J/g deformation energy per sample mass. Figure 11.3 shows an ultimate compression test of an Aerographite sample (density of 2.86 mg/cm^3) up to 97 % compression where it reached a maximum compressive stress of 18 KPa .

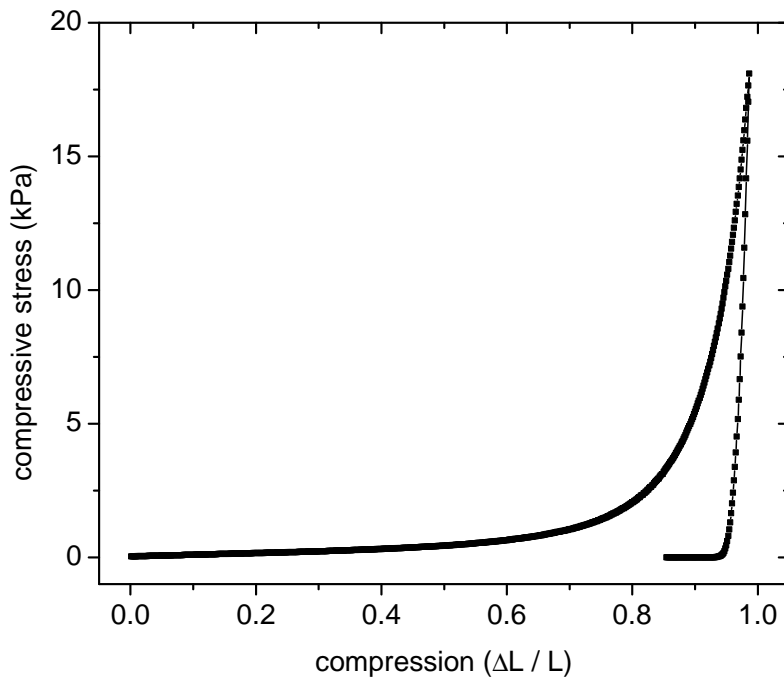


Figure 11.3: Ultimate compression test of an Aerographite sample of density = 2.86 mg/cm^3 showing a rapid increase of the compressive stress in the densification region starting at 60 % deformation.

The observed properties of Aerographite show similarities to the mechanical aspects of an exclusively bending dominated lattices. However, if a lattice is either bending- or stretch-dominated depends upon the number of joints, struts and states of self stress in the unit cells (see *equation (3.12)*). The Aerographite network consist of a broad distribution of tetrapods and other fragments (see Figure 9.1) what makes it very unlikely that the whole network consists exclusively out of bending- or stretch-dominated unit cells rather than a mixture of both types. Most likely the mechanical

response of Aerographite is a superposition of a bending and a stretch-dominated properties.

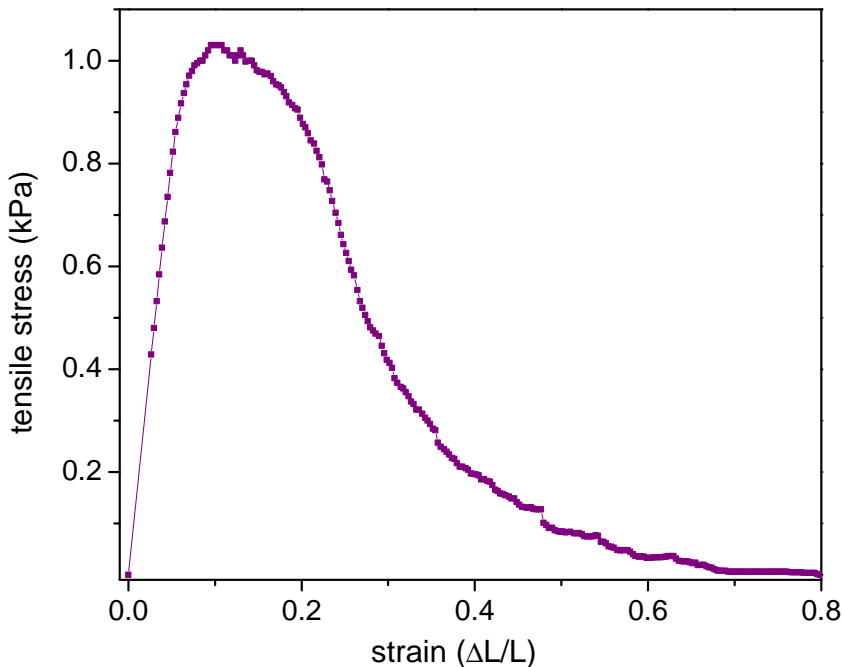


Figure 11.4: Tensile test of the hollow framework variant of Aerographite ($180 \mu\text{g}/\text{cm}^3$) until fracture. In the elastic regime the sample exhibits a Young's modulus of 15 kPa .

In Figure 11.4 a tensile fracture test of the hollow framework variant of Aerographite is shown. This variant ($\text{density} = 180 \mu\text{g}/\text{cm}^3$) exhibits a Young's modulus of 15 kPa and an ultimate tensile strength of 1 kPa . On the basis of this results the specific moduli of $E/\rho^2 = 0.46 \cdot 10^6 \text{ Pa}/(\text{kg}/\text{m}^3)^2$ and $E/\rho^3 = 2.6 \cdot 10^6 \text{ Pa}/(\text{kg}/\text{m}^3)^3$ were calculated and the data point in the Ashby material selection map in Figure 3.2 was entered. In the Ashby material selection map it can be seen that Aerographite, carbon fiber and Balsa wood lay all very close to the guideline for the the merit index \sqrt{E}/ρ from *equation (3.9)*. By applying the guideline for the merit index $k = \sqrt[3]{E}/\rho$ from *equation (3.6)* it can be seen that Aerographite is even superior to carbon fiber and Balsa wood. Of course Aerographite was not designed as engineering material. However, these number are very important for technological applications of Aerographite which require small masses to reduce acceleration induced forces.

This can be micro-electro-mechanical systems (MEMS) or electrode applications that should withstand vibrations or impacts. [31]

11.1. Cyclic Stiffening of Aerographite

During cyclic deformation experiments of Aerographite bulk samples it was observed that the developed stresses increased with the number of deformation cycles [31]. This effect was observed for cyclic compression and tensile tests. Figure 11.5 shows a cyclic tension/compression experiment of an Aerographite sample with a density of 14.65 mg/cm^3 over a number of 19 deformation cycles. The cyclic loading started with compression up to $\approx 4.2\%$ and subsequent the sample was strained to $\approx 4.7\%$. It can be seen that the maximum stress increases with the number of cycles but this trend comes to some saturation and cycle 15 and 19 are almost identical. The deformation cycles also indicate a certain energy dissipation as the envelope of these curves is a measure for the dissipated deformation work per unit volume (see also chapter 11.2).

For the explanation of the cyclic stiffening effect different microscopic mechanisms can be assumed. The deformation of the graphitic tubes inside the network can cause a crumpling of their surfaces what can cause the formation of wrinkles. Such wrinkles can make the individual tubes stiffer as they prevent the buckling of the tubes. It can be speculated, that this mechanism is similar to the increased stiffness of corrugated cardboard [100, 101] which is widely used in packaging industry.

A second mechanism could be related to the Van der Waals adhesion between individual tubes when they get attached during the deformation of the network. Such additional network junctions can increase the stiffness of the network when the deformation mechanism changes from bending to stretch dominated nature as discussed in chapter 3.2. The actual microscopic mechanism has to be elaborated in additional in situ experiments.

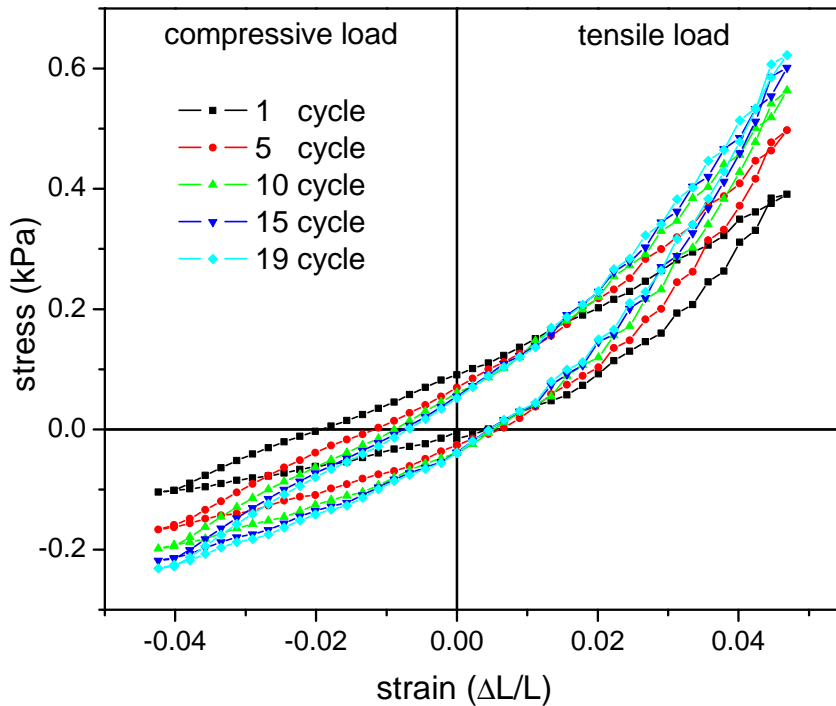


Figure 11.5: Cyclic compressive/tensile loading of an Aerographite sample with a density of 14.65 mg/cm^3 . For a number of 19 cycles the maximum tensile stress increased by 60 % and the maximum compressive stress increased by 120 %.

11.2. Visco-elastic Behavior of Aerographite

In this chapter, the visco-elastic properties of Aerographite will be discussed. The visco-elasticity of Aerographite is an surprising result and is normally not expected from such type of material. For this reason a first simple model for the microscopic mechanism of the visco-elasticity was introduced. The proposed model will be discussed in this chapter.

During the deformation of an Aerographite bulk sample in a compression or tensile cycle, it can be observed, that the stress/strain cycle exhibits a hysteresis. This hysteresis is also present for very small deformations which are purely elastic (see Figure 11.6). The area which is enclosed by the loading and unloading curve is a direct measure, for the energy per unit volume, which is dissipated during the deformation cycle and can be calculated by the help of equation 11.1 where E_{diss}

denotes the dissipated energy, V the volume of the sample, σ the stress and ϵ the strain [65].

$$\frac{E_{diss}}{V} = \oint \sigma d\epsilon \quad (11.1)$$

This means, for the reversible deformation of Aerographite a characteristic energy dissipation occurs. The dissipative part of the energy in the stress strain cycle is caused by the viscous properties of Aerographite. This is a typical phenomena for visco-elastic materials as discussed in 3.3.

A second experiment which proved the visco-elasticity of Aerographite was the strong compression ($\approx 85\%$) of a cylindrical sample of 1 cm^3 volume. Over a time scale from 5 to 10 days it can be observed, that the sample recovers to $\approx 70\%$ of the original height by a continuous expansion.

11.3. Model for the Visco-elastic Mechanisms in Aerographite

Visco-elasticity is a well known phenomena for a huge variety of polymers and other materials. In polymers, the most important causal mechanism for visco-elasticity is a change of the molecular chain conformation which is thermally activated. With respect to the differences in the atomic structure and morphology of Aerographite it is more likely that the visco-elastic mechanisms in Aerographite differs from this ones in polymers.

In literature the visco-elastic properties of arrays of vertically aligned carbon nanotubes (VA-CNTs) have been reported [102]. For the VA-CNT arrays it was suggested that the viscous creep during indentation is attributed to the complex microstructure and the helical shape of the CNTs. It was supposed, that the energy dissipation in the VA-CNTs is based on the same mechanism which causes the visco-elasticity of macroscopic helical springs [103]. Visco-elastic properties have

also been reported for carbon aerogels [26] but there has been no model, describing the intrinsic mechanisms, yet. The here proposed mechanism for the visco-elasticity of Aerographite, is related to the Van der Waals adhesion of individual Aerographite structures during the deformation.

When mechanical stress is applied to Aerographite, the conformation of the tubes and tetrapods in the network will change according to the stress distribution in the network. The change of the spatial position of neighboring tubes and tetrapods causes them to touch each other and consequently they get attached by Van der Waals forces. At the same time, other structures which are held in place by Van der Waals forces become detached. It can be expected, that during the deformation of the Aerographite network, constantly structure elements become attached and detached which can be regarded as some "internal friction". The strong adhesion between two Aerographite tubes was also observed during the SEM in situ experiments with the Aerographite networks. The time dependence of this process is related to the peeling processes which occur during the detachment of the VdW adhered structures. In the in situ experiments it was observed, that pre bent tubes which are adhered, snapped back to their original position after some delay. These experimental hints support the suggested mechanism for the visco-elasticity in Aerographite.

A second mechanism which can be attributed to the energy dissipation is the reversible buckling of Aerographite tubes and tetrapods. The reversible buckling of a single Aerographite tubes occurs with sufficiently high bending moments and is elaborated in detail at the end of this chapter. Further, also the slip and shear movement of tubes and tetrapods in the network can result in energy dissipation.

The measurement in Figure 11.6 was performed with a strain rate of $1.25 \mu/s$ at an Aerographite sample of ($3.1 mg/cm^3$) density. This strain rate was applied in almost all mechanical tests because of the settling time of the precision balance (see chapter 6.1). For small compressions (about 5 % compression) the onset of the stress/strain curve can deviated from the normal sample behavior. The samples

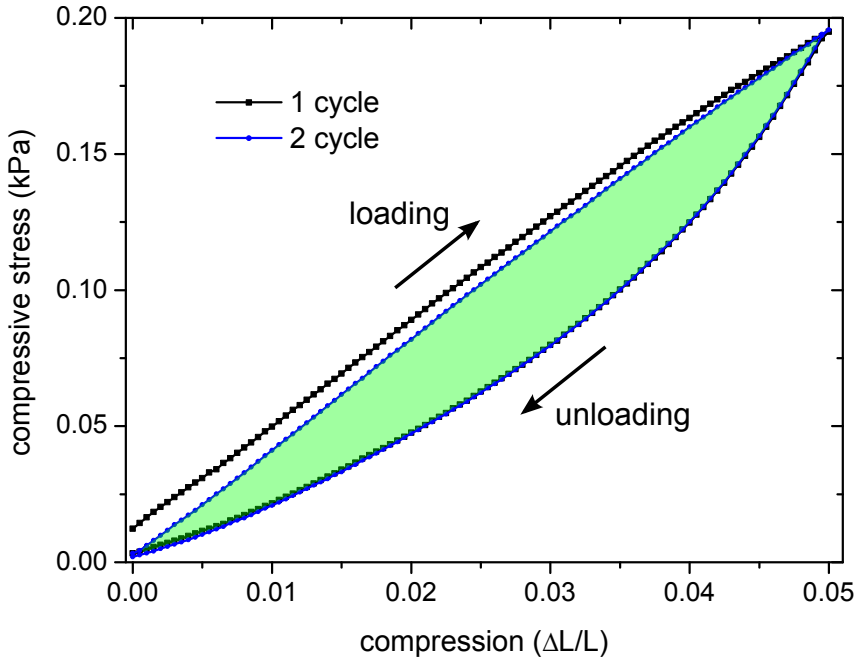


Figure 11.6: First (black) and second (blue) cycle of a compression test of an Aerographite network (density = 3.1 mg/cm^3). The area of the second deformation cycle (indicated in green color) corresponds to a dissipated energy per volume of 1.37 J/m^3 .

are not perfectly flat and therefore the mechanical contact area is smaller at the beginning of the compression test until the total area of the sample is in mechanical contact with setup. To avoid this effect, some slight preload can be applied to the sample before the first cycle is conducted.

For the measurement displayed in Figure 11.6 a preload of 12 Pa was applied. The first compression cycle exhibits a slight plastic deformation (indicated by the stress difference before and after the first cycle) while the second compression cycle is completely elastic. It can be speculated, that inside the virgin Aerographite sample some structures are adhered by VdW forces during the first deformation cycle causing the plastic deformation. This would explain why even for very small sample deformations, which are normally purely elastic, plastic deformation occurs. Both deformation cycles shows a significant hysteresis which is attributed to the visco-elasticity. To determine the energy dissipation of the second cycle, the integral according to equation (11.1) was calculated. The sample volume, the density, the

dissipated energy per unit volume, the total dissipated energy and specific energy for the second cycle are listed up in table 11.1.

Table 11.1: Characteristic energy dissipation for the visco-elastic hysteresis loops from the measurement in Figure 11.6 and Figure 11.7.

volume (cm ³)	density (mg/cm ³)	strain rate (μm/s)	E_{diss}/V (J/m ³)	E_{diss} (μJ)	specific energy (mJ/g)
0.866	3.108	1.25	1.37	1.189	0.442
0.93	1.82	0.80	0.21	0.195	0.151
0.93	1.82	1.25	0.27	0.246	0.146

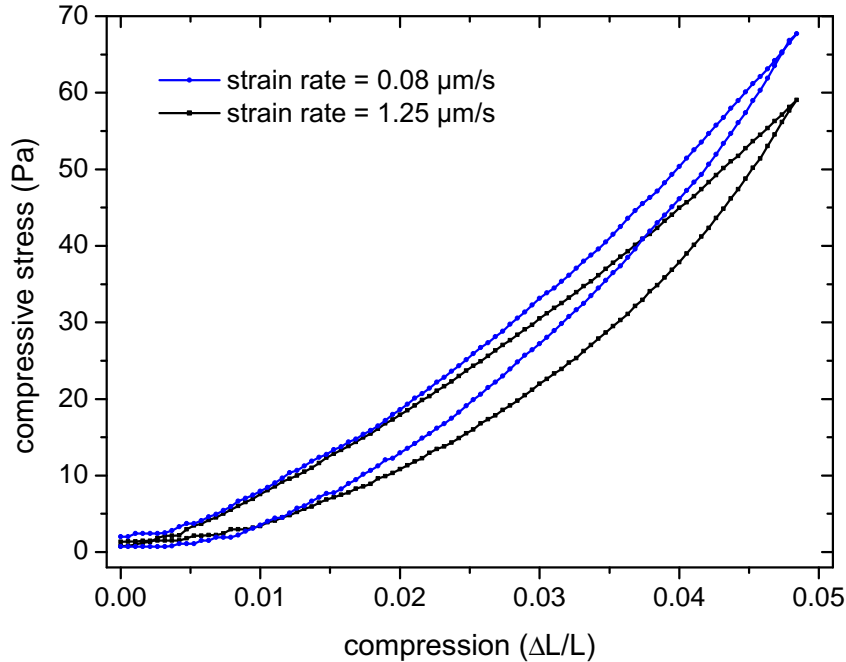


Figure 11.7: Compression test of an Aerographite network (density = 1.82 mg/cm³) for two different strain rates. The area of the fast deformation cycle with a strain rate of 1.25 μm/s is 1.27 times bigger than the area of the deformation cycle with 0.08 μm/s strain rate. This is related to the viscous properties of Aerographite which are strain rate dependent. The values of the energy dissipation for the first and second cycle can be found in table 11.1.

To prove the strain rate dependence of the visco-elastic properties of Aerographite the measurement depicted in Figure 11.7 was conducted at two different strain

rates ($0.8 \mu\text{m}/\text{s}$ and $1.25 \mu\text{m}/\text{s}$) to a maximum compression of 4.8 %. As presented in table 11.1 the dissipated energy for the strain rate of $1.25 \mu\text{m}/\text{s}$ is about 1.3 times higher than the for the slow deformation rate. This indicates the expected time dependence of the suggested intrinsic mechanisms behind the visco-elastic properties. Further, it is obvious that also the maximum compressive stress for both measurements differs. One explanation for this effect would be the cyclic stiffening of Aerographite discussed in chapter 11.1. However, it is more likely, that the difference in maximum stress is influenced by the strain rate rather than the cyclic stiffening. With respect to the difference of only one deformation cycle the difference in stress is to pronounced to be caused by the cyclic stiffening.

To identify the intrinsic mechanisms of the visco-elasticity in Aerographite, single tubes were bent inside the SEM until buckling occurred. Figure 11.8 shows a series of SEM micrographs which demonstrate the buckling of a single hollow tube of Aerographite which has been bent in between two gold tips. The experiments revealed, that the buckling is reversible without "visible" damage at the section of the tube which exhibited the flexure folding (see Figure 11.8c and Figure 11.8d). The same property has already been reported in literature for multiwalled carbon nanotubes (MWCNT). The repeated bending and buckling of MWCNTs without damage was reported by Falvo et al. [104] but in contrast to these carbon nanotubes the diameter of the examined Aerographite tubes is about three orders of magnitude bigger. However, these results indicate similarities between the elastic buckling of Aerographite tubes and MWCNTs.

The stiffness of a buckled cylindrical tube is dramatically decreased by the Brazier effect [99]. Hence, the stiffness of a buckled Aerographite tube is also drastically lowered in the buckled state. As a result, the spring constant D (defined in chapter 10.2) of the tube changes to lower values if the critical buckling stress is overcome. This was elaborated in the in situ bending test of the individual tetrapods (see also Figure 10.3). According to the model which was derived in 10.2, this results in a softening of the Aerographite network the more tubes and tetrapods buckle.

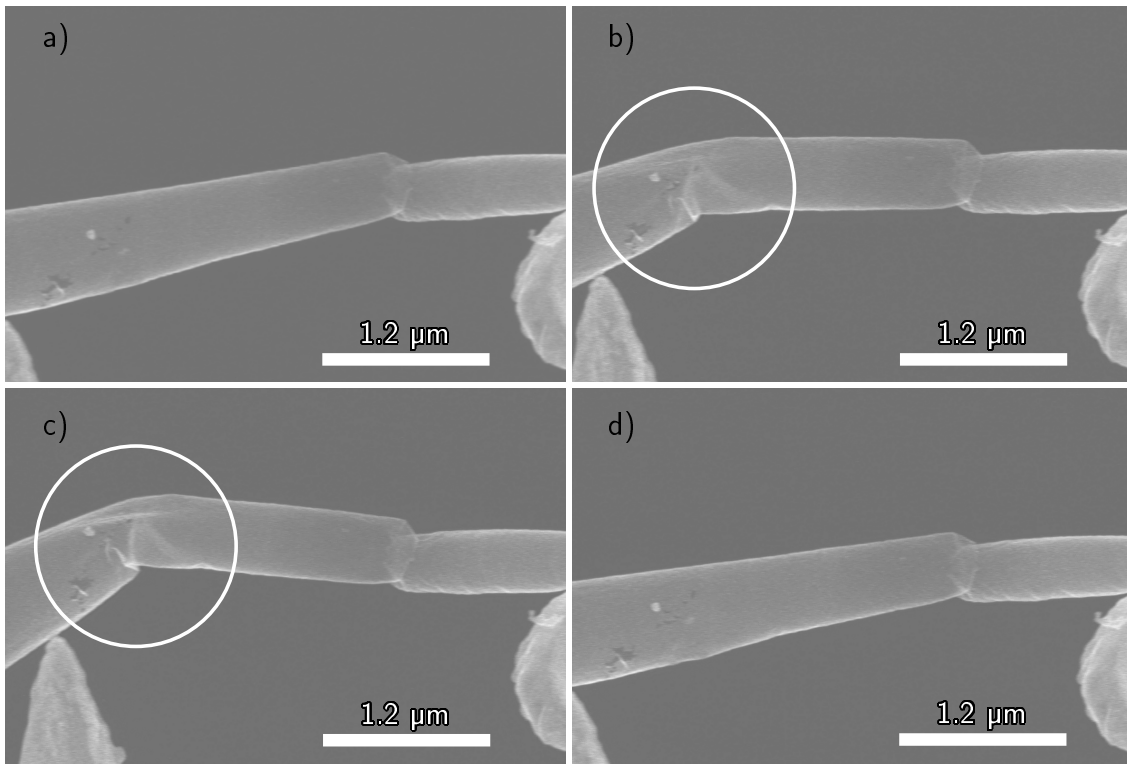


Figure 11.8: SEM micrograph series from the buckling of a single tube of Aerographite which was bent in between two Gold tips. a) Undeformed state b) The tube has started to buckle (position indicated by the circle). c) Heavily buckled (The stiffness of the tube is dramatically decreased due to buckling.) d) The tube recovered elastically to its original shape.

Figure 11.9 shows an schematic visco-elastic model for Aerographite which is based on the standard linear solid model. In contrast to the standard linear solid model, the spring constant of spring A in the model can exhibit a change from D_1 to D_2 with increasing number of buckled of Aerographite tubes/tetrapods. It can be assumed, that there will be no instant change from the unbuckled to the buckled state in the Aerographite network rather than a smooth transition because the buckling is a collective phenomena. The instant change from D_1 to D_2 as illustrated in Figure 11.7a represents the idealized case for an individual tube but is in accordance with in situ bending measurement displayed in Figure 10.3.

The spring B in the model represents those tetrapods which are not buckled. These can be tubes/tetrapods which purely experience tensile stress in the network. The

dashpot of viscosity η represents the dissipative deformation mechanisms in the Aerographite network like the peeling of tubes adhered by VdW forces. Depending on the strain rate, the stress in spring A varies and consequently the spring constant, if the threshold stress for the buckling is overcome. For low strain rates the dashpot will be strained and the stress in spring A is very small. For intermediate strain rates the stress in spring A will increase and it possesses spring constant D_1 . For high strain rates, there is less time for peeling of tubes/tetrapods adhered by VdW forces. Consequently a higher fraction of tubes/tetrapods exhibits bending or buckling and a softening of the network occurs. This would explain of the lower maximum stress which was observed for the higher strain rate in the measurement from Figure 11.7.

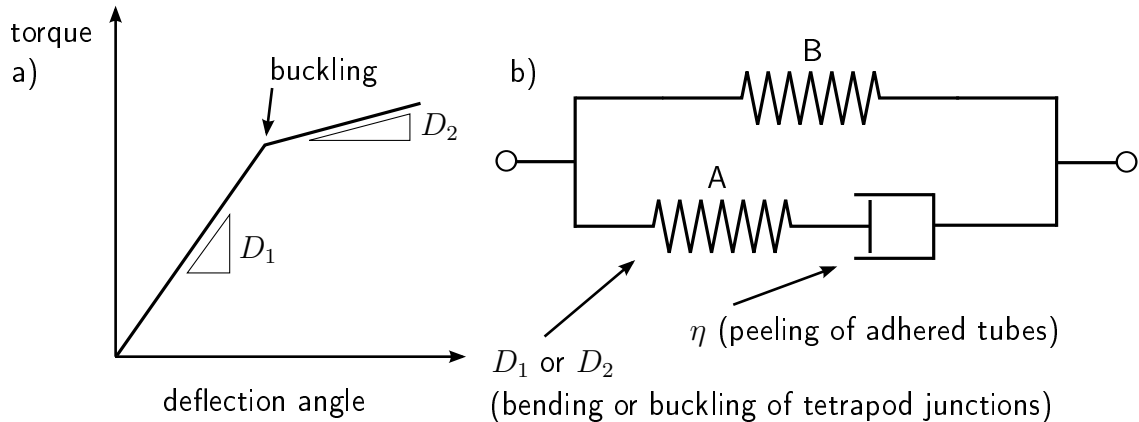


Figure 11.9: a) Schematic diagram for the spring constant of a single Aerographite tube. At a threshold of the applied torque the tube buckles and the spring constant (slope of the curve) drops instantly. b) Mechanical equivalent circuit for the visco-elastic properties of Aerographite. The spring constant of the spring A is variable from D_1 to D_2 and depends upon the applied strain.

To prove this model and to evaluate if the visco-elasticity of Aerographite is related to individual structures which are adhered by VdW forces, stress strain experiments at different temperatures have to be conducted in future work. The peeling of adhered structures should be accelerated at elevated temperatures because of the weak character of the VdW forces. The thermal energy at elevated temperatures can accelerate the separation of adhered tubes and tetrapods in the network. This means, at higher temperature the amount of the dissipated energy during a deformation

cycle should be smaller than at low temperatures. Further, the model predicts a relation between the pore size and the viscous properties of the network. For a smaller pore size the probability for the adhesion of tubes and tetrapods should increase, resulting in higher energy dissipation during deformation. For these kind of experiments it would be required to fabricate Aerographite networks with a very homogenous pore size.

12. Electrical Properties of Aerographite

In this chapter, the results from the electrical in situ experiments and bulk measurements of Aerographite are presented and discussed. Furthermore, the correlation between the conductivity of Aerographite and its porosity will be elaborated.

12.1. Electrical Conductivity of Aerographite Bulk Samples

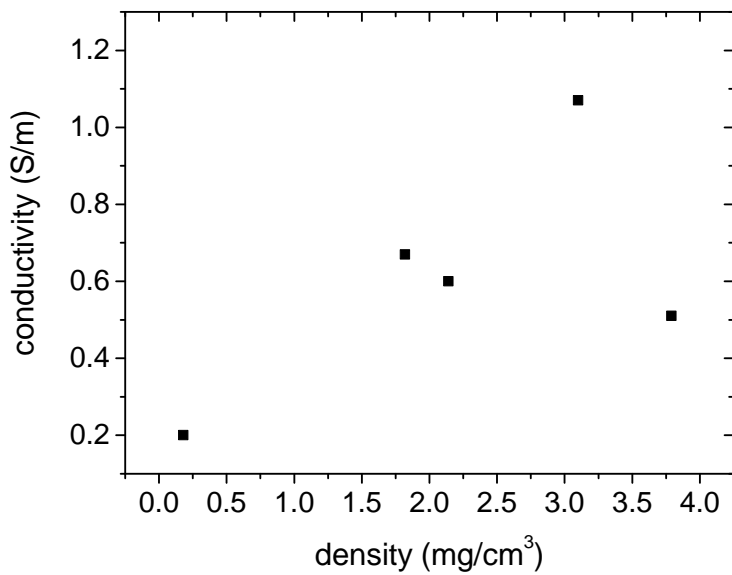


Figure 12.1: Electrical conductivity of different structural types of Aerographite versus their density.

The electrical measurements at the Aerographite bulk samples showed, that the contact preparation is an important parameter. Therefore, all measurements were

performed with Gold coated Copper contacts which have been cleaned by acetone and isopropyl alcohol. The bulk samples (volumes ranging from 1 to 2 cm³) showed typically ohmic behavior. Figure 12.1 shows an overview of the conductivity of different structure types of Aerographite versus the density (see also table 12.1).

To compare the electrical conductivity with other modifications of carbon, the porosity of the Aerographite network has to be considered. The porosity Φ is defined like shown in *equation* (12.1), where ρ denotes the density of the Aerographite network, ρ_0 denotes the density of Aerographite without pores, V_p denotes the volume of the pores in the network and V_s denotes the volume which is actually occupied by carbon.

$$\Phi = 1 - \frac{\rho}{\rho_0} = \frac{V_p}{V_p + V_s} \quad (12.1)$$

This means, that the effective cross sectional area of the network is smaller than the cross sectional area of the porous sample. The geometry corrected conductivity of Aerographite without pores can be calculated by *equation* (12.2) were A_{eff} denotes the effective cross sectional area, l the length and R the resistance of the sample.

$$\sigma_{gc} = \frac{l}{RA_{eff}} = \frac{l}{RA(1 - \Phi)} \quad (12.2)$$

Due to the difficulties of the measurement of the nonporous Aerographite density ρ_0 , the density was assumed with 2.26 g/cm³ which corresponds to the density of ideal bulk graphite [105]. Table 12.1 displays the conductivity σ , the geometry corrected conductivity σ_{gc} , the density ρ and the corresponding porosity Φ for different types of Aerographite.

In table 12.1 it can be seen that the conductivity scales in general with the density except the variant with a density of 3.79 mg/cm³. This can be attributed to the differences in the hybridization states of the carbon as discussed in 9. In comparison to the conductivity of bulk graphite the geometry corrected conductivity σ_{gc} is lower. This can be explained by the higher disorder in the layers of the graphitic structure of Aerographite as discussed in 9.

Table 12.1: Overview of the electrical conductivity σ and the corresponding density / porosity of different types of Aerographite structures.

density ρ (mg/cm^3)	porosity Φ	σ (S/m)	σ_{gc} (S/m)
0.18	0.99992	0.20	2511
1.82	0.99919	0.67	832
2.14	0.99905	0.60	634
3.10	0.99862	1.07	780
3.79	0.99832	0.51	304

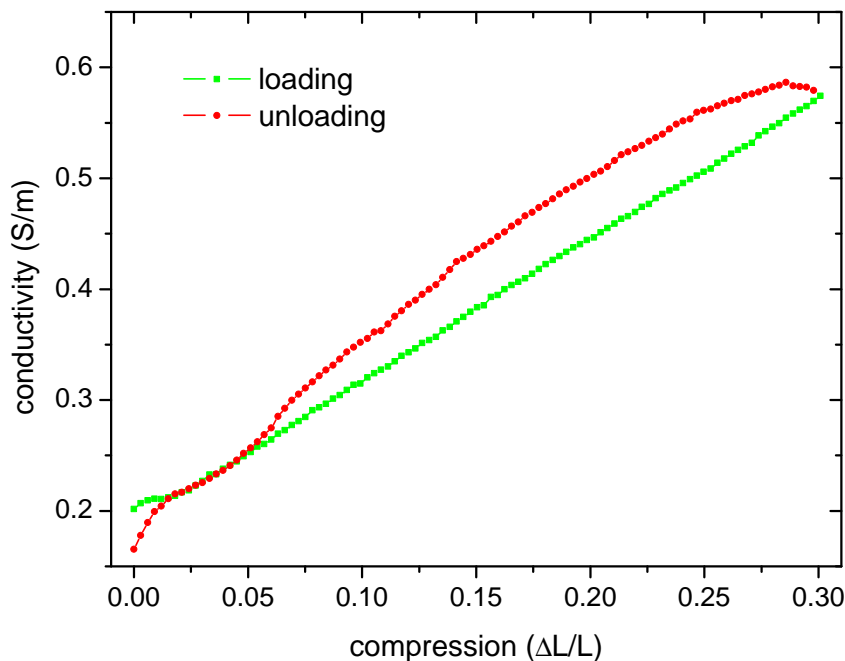


Figure 12.2: Electrical conductivity increase of an Aerographite network during compression.(density = $0.18 mg/cm^3$)

A typical example for the conductivity increase of an Aerographite network during compression is depicted in Figure 12.1. In the loading cycle the conductivity increases nearly linear with the compression (the change in the sample length was considered for the calculation of the conductivity). A linear increase of the conductivity implies that $R \propto 1/compression$ what can be explained by the change in porosity according to equation (12.2). The hysteresis in the unloading cycle can be

explained by the change in the contact resistance during the deformation cycle and the residual plastic deformation after the cycle. For higher compression states the conductivity reaches a saturation level.

12.2. Electrical In Situ Experiments at single Aerographite Structures

In the electrical in situ experiments a number of selected Aerographite tubes was contacted with two Gold tips (method described in chapter 6.3) and several current/voltage curves (IV curves) were recorded for each sample. Figure 12.3 shows a SEM micrograph of a single Aerographite tube which was contacted with two Gold tips and Figure 12.4a demonstrates the corresponding IV curve which has been measured at the virgin sample. The measurement started at 0 V and up to 4 V bias voltage the current measures less than $1\text{ }\mu\text{A}$. At a threshold voltage of $+4\text{ V}$ the current increases rapidly which can be related to some breakdown. The compliance of the sourcemeter was set to $10\text{ }\mu\text{A}$ and was reached at this point. For this reason the current was limited to $10\text{ }\mu\text{A}$ in this measurement by the sourcemeter. It can be seen, that after the application of $+4\text{ V}$ bias voltage the conductivity was significantly higher which supports the theory of a breakdown. The IV curve in Figure 12.4b was measured subsequently to the virgin IV curve but in a smaller voltage range. The higher conductivity in this measurement is most probably related to a change in the contact properties between the gold tips and the surface of Aerographite. It is very likely that during the first IV measurement an insulating or semiconducting passivation layer on top of the tube is penetrated by an electrical breakdown by exceeding the critical field strength. The non-ohmic character of the IV curve indicates a charge transport by hopping [106, 107]. One explanation for this contact behavior would be a electronic charge transport via localized sp^2 states [107, 108] while the majority of the carbon atoms at the surface is sp^3 hy-

bridized and acts as transport barrier [109]. Similar electrical properties have been studied for different reduction states of graphene oxide(GO) which electrical nature can vary from an electrical insulator to a graphene-like semimetal depending upon the ratio of sp^2 and sp^3 bonds [110].

To clarify if the whole surface of Aerographite possesses the same contact behavior and in order to exclude any contamination of the gold tips, the tube was contacted at several positions. These measurements showed the same characteristic threshold behavior, indicating the presence of an insulating surface layer. This layer might originate from residual organic cracking products from the toluene injection of the Aerographite conversion process. These residuals can condense on the surface of the Aerographite network during the cooling of the CVD reaction chamber.

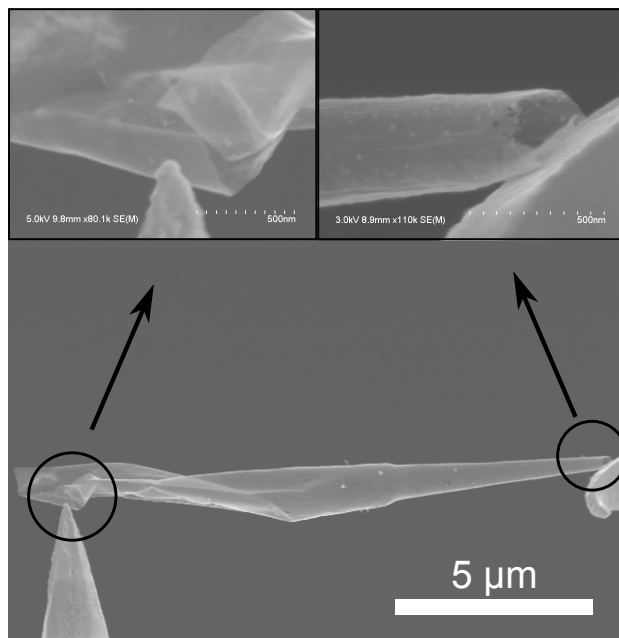


Figure 12.3: SEM micrograph of an individual Aerographite tube isolated from the network and contacted with two gold tips. The insets shows a magnified view of the contact points between gold tip and tube for the electrical measurements.

To avoid such an insulating surface layer on Aerographite, the CVD process can be modified. After the second toluene injection (see Figure 5.5), the CVD reaction chamber can be flushed with Argon while the temperature is kept constant at $800\text{ }^\circ\text{C}$

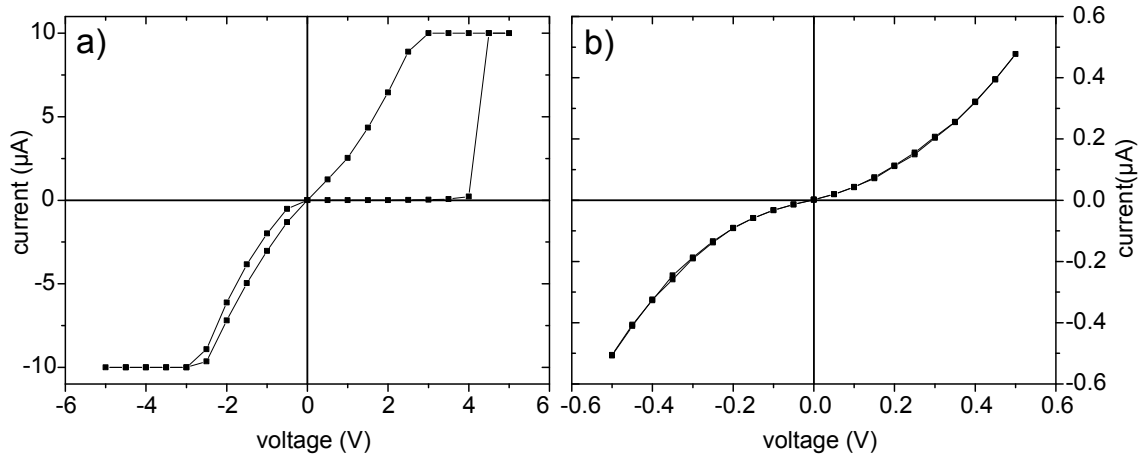


Figure 12.4: IV characteristic of the Aerographite tube from figure 12.3: a) IV response of the virgin Aerographite sample. At 4 Volts a significant drop in the resistance is observable. b) IV characteristic of the trained sample.

or even increased to 900 °C. This prevents the condensation of residual cracking products which are transported to the exhaust tube by the Argon flow. It can be expected that Aerographite samples which have been treated in such a manner, show a higher increase of electrical conductivity during compression. Tubes and tetrapods which get in contact to each other during the compression provide new electrical paths. This is not the case if the surface is of insulating nature.

13. Aerographite Electrodes

In this chapter two different applications of Aerographite as electrode material are presented. Like discussed in the experimental part, Aerographite was tested as electrode material in an electrical double-layer capacitor and also as cathode material in a lithium-sulfur battery after it has been infiltrated with sulfur. Further, a theoretical approximation of the specific surface area of Aerographite is introduced because its special interest for all kind of electrode applications.

13.1. Specific Surface Area of Aerographite

For applications like an electrical double-layer capacitor or battery electrodes the surface density of Aerographite is an important parameter. The specific surface area is defined as the ratio of freely accessible surface area A of a porous material and its mass m shown in *equation* (13.1).

$$\text{specific surface area} = \frac{A}{m} \quad (13.1)$$

The following derivation is an approximation and based on the assumption that the wall thickness of the Aerographite tubes is homogeneous in the entire volume of the sample. The density of the graphitic layers is assumed to be equal to the density of bulk graphite ($\rho = 2.26 \text{ g/cm}^3$). In a porous Aerographite network just a certain fraction of its volume is occupied by the volume of the graphitic layers. The total area A of this graphitic layers can be expressed like in *equation* (13.2) where m denotes the mass of the graphitic tubes, d denotes the thickness of the graphitic walls and ρ represents the density of the graphitic layers.

$$A = \frac{m}{d\rho} \quad (13.2)$$

By dividing *equation* (13.2) with the mass of the graphitic layers and multiplying the result by a factor of two (inner and outer surface), one achieves *equation* (13.3).

$$\frac{A}{m} = \frac{1}{d\rho} \quad (13.3)$$

The typical wall thickness of the closed shell variant of Aerographite measures $\approx 10\text{ nm}$ as measured by transmission electron microscopy. This results in a theoretical specific surface area of $\approx 90\text{ m}^2/\text{g}$.

13.2. Electrical Double-Layer Capacitor with Aerographite Electrodes

The measurements with the electrical double-layer capacitor with Aerographite electrodes proved the applicability of Aerographite as electrode material. An example of a discharge curve with a $1\text{ K}\Omega$ is shown in Figure 13.1. The highest measured capacity was determined to be 32 mF for a total electrode mass of 56.8 mg and an electrode volume of 2.2 cm^3 . This results in a specific capacity of 0.53 F/g if the pure electrode mass is considered. The maximum energy W stored in the capacitor depends on utilized solvent in the electrolyte because it must not be decomposed by electrolysis. The maximum charging voltage of the EDLC in the experiments was 1.6 V . According to *equation* (13.4) this results in a energy of 41 mJ and a specific energy of 0.72 J/g .

$$W = \frac{1}{2}CU^2 \quad (13.4)$$

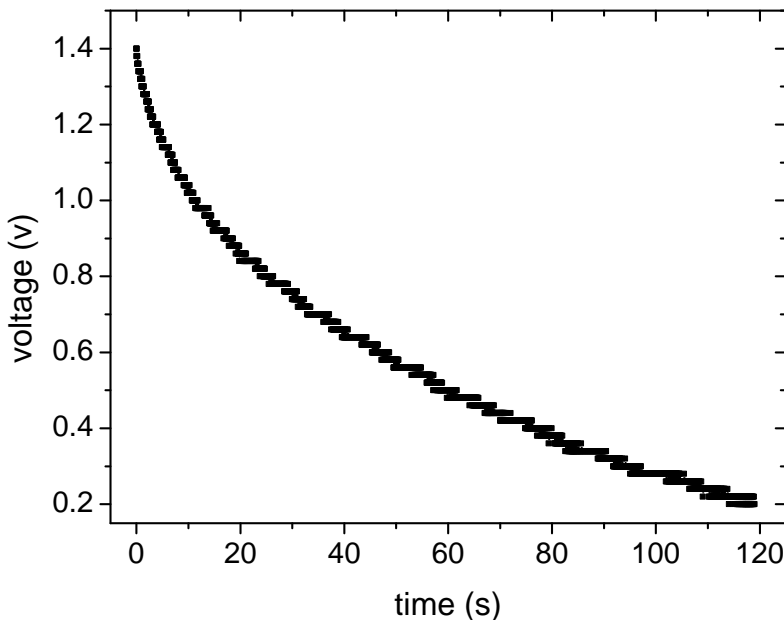


Figure 13.1: Discharge curve of an electrical double-layer capacitor with Aerographite electrodes over a $1\text{ K}\Omega$ resistor. The capacitor had a capacity of 32 mF for a total electrode mass of 56.8 mg and an electrode volume of 2.2 cm^3 . This results in a specific capacity of 0.53 F/g .

13.3. Sulfur-infiltrated-Aerographite-Cathodes for Lithium Batteries

The as prepared half cell with the sulfur-Aerographite cathode was subjected to cyclic voltammetry to examine the electrochemical processes at the electrodes and the capacity fading. The cycles 2-4 are depicted in Figure 13.2. The open circuit voltage of the as prepared half cell measured 2.7 V (at room temperature).

In the following, the third cycle will be discussed. This cycle is representative for the electrode processes because the formation of the solid electrolyte interface (SEI) takes place during the first two cycles. The SEI forms, because decomposition products of the electrolyte form a passivation layer on the surface of the electrodes and therefore the SEI has a significant influence on the peak positions in the cyclic voltammetry. For this reason the third cycle was selected for the discussion.

The cyclic voltammogram shows one peak during the lithiation and two peaks

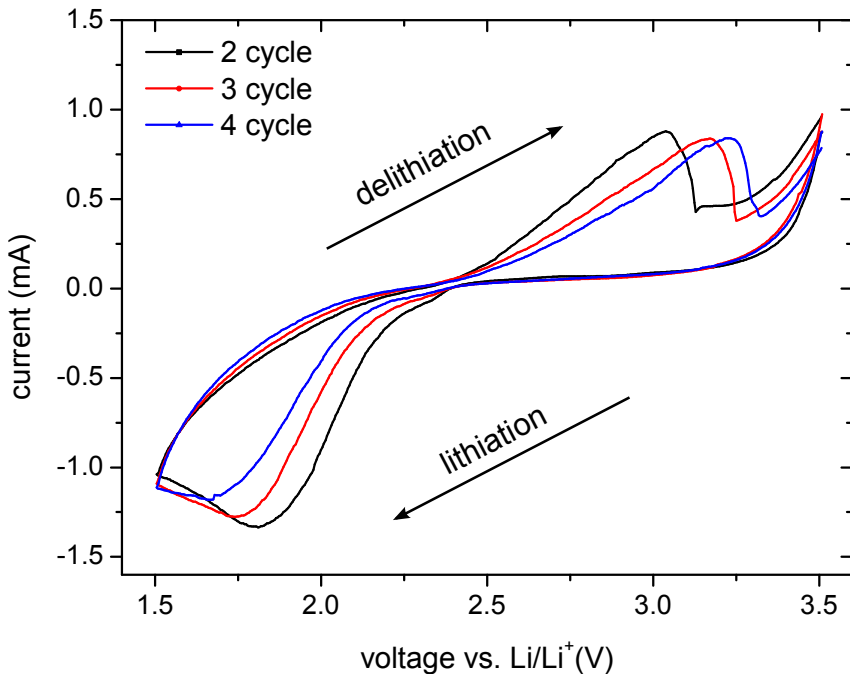


Figure 13.2: Cyclic voltammetry of a half cell with sulfur infiltrated Aerographite as active cathode material (sweep rate 0.1 mV/s).

during the delithiation. This corresponds to a reversible lithiation and delithiation which means that the test cell was successfully charged and discharged. It can be seen, that the lithiation peak shifts to lower voltages with the number of cycles while the delithiation peak is shifted to higher voltages. This means, that the lithiation is enhanced while the delithiation becomes inhibited.

During the reverse scan the lithiation of the sulfur takes place (discharge of the half cell). The reverse scan shows one peak at 1.74 V. This peak is most probably attributed to a one step formation of Li_2S or Li_2S_2 at the cathode which is supported by the literature [111, 112]. At 1.5 V the scan is reversed what should not be confused with a second peak.

During the forward scan the delithiation of the sulfur takes place, which means that lithium ions are removed from the Li_xS_y (charging of the half cell). The forward scan shows a first peak at 3.17 V. At the maximum voltage of 3.5 V a second peak is inhibited because the maximum voltage of the cyclic voltammetry was reached. The maximum voltage of the cyclic voltammetry was fixed to 3.5 V to protect the

solvent of the electrolyte from degradation. The first and the second peak correspond to a possible two step delithiation process. This means, that a step wise reduction from Li_2S to short polysulfides to elemental sulfur occurs which is also supported by the literature [111,112]. A peak shift is observed for the lithiation cycles as well as for the delithiation cycles. This peak shift is probably caused by polysulfides which seal the pores of the Aerographite and therefore inhibit the access of the lithium ions.

It can be seen, that the achieved currents on the lithiation side of the cycles decreases constantly from cycle 2 to 4. This indicates some capacity fading which can be attributed the so called polysulfide shuttle which is the major problem in current state lithium-sulfur batteries [84,85]. The polysulfide shuttle causes a loss of active sulfur material at the cathode and the formation of a passivation layer on the anode.

The half cell was subjected to a post mortem analysis. The half cell was disassembled and the separator membrane was visually checked. The separator showed a deep red/orange color which is attributed to the soluble polysulfides. These soluble polysulfides are unfavorable because they drive the polysulfide shuttle and cause the capacity fading. In order to achieve good cyclic stability of the lithium-sulfur battery, the polysulfide shuttle has to be inhibited. For this reason it is beneficial, if the polysulfides get immobilized in the separator membrane.

The cyclic voltammogram in Figure 13.2 proved the working principle of the sulfur infiltrated Aerographite cathodes in lithium batteries. However, still the cyclic stability has to be increased in order to achieve high quality lithium sulfur batteries with long lifetimes. This can be achieved by a reduction of pore size of the utilized Aerographite for example by a compression step because smaller pore sizes are beneficial for a better sulfur confinement in the cathode. Recently published researches [113] report about excellent cyclic stability of lithium sulfur batteries by applying the concept of the Aerographite synthesis (sacrificial ZnO templates) for the fabrication of this batteries.

Conclusion and Outlook

In this work, a novel 3D interconnected network material from graphitic carbon was established. This highly porous material called Aerographite was fabricated by a completely new synthesis method. Highly porous ZnO networks stemming from the flame transport synthesis (FTS) are set up by interconnected anisotropic structures and form the basis for the fabrication of Aerographite. In collaboration with the technical university of Hamburg these ZnO networks have been utilized as sacrificial templates and were converted to Aerographite in a modified CVD process. It was demonstrated that the morphology and surface structure of the sacrificial ZnO network templates is completely adopted by the Aerographite networks which allows a free control over the morphology of Aerographite.

The systematic tailoring of ZnO templates with porosities up to 97 % enabled the fabrication of a hierarchical Aerographite variant with a porosity of 99.99 % resulting in a minimum density of $180 \mu\text{g}/\text{cm}^3$. This makes Aerographite one of the lightest solid materials known in literature. Despite its low density Aerographite possesses a high electrical conductivity, is optically opaque and completely black.

The novel mechanical properties of bulk Aerographite were studied with a self built mechanical test setup and revealed highest specific moduli of $E/\rho^2 = 0.46 * 10^6 \text{ Pa}/(\text{kg}/\text{m}^3)^2$ respectively $E/\rho^3 = 2.57 * 10^6 \text{ Pa}/(\text{kg}/\text{m}^3)^3$ under tensile load. This makes Aerographite theoretically the first choice in an Ashby material selection map to obtain the minimum deflection of a free standing bar with free thickness and given mass.

In cooperation with the University of Latvia the intrinsic deformation mechanisms of Aerographite networks were studied by in situ experiments inside a scanning electron microscope. The stiffness of individual Aerographite tetrapod junctions were

measured. On the basis of these results an analytical model for the elastic deformation of bulk Aerographite networks was derived and validated by a quantitative comparison with experimental results from the mechanical bulk measurements.

During the mechanical characterization of bulk Aerographite it was found that the Aerographite network possesses surprisingly visco-elastic properties which is normally not expected from such type of material. In detailed in situ experiments first hints on the microscopic mechanisms were found and a novel model on the visco-elasticity in Aerographite was established. In this model it is stated, that the Van der Waals adhesion between individual tubes of the Aerographite network causes the viscous material properties which was strongly indicated by the findings from the in situ experiments.

The functional application of Aerographite was demonstrated by the construction of two prototypes. An electrical double-layer capacitor with Aerographite electrodes was built up and possessed a promising specific capacity of 0.53 F/g . By infiltration of sulfur into Aerographite a cathode material for a rechargeable lithium-sulfur battery was created and the capacity fading was studied by cyclic voltammetry.

Based on the results of this work, several aspects are found highly interesting for the future work. To increase the cyclic stability of the developed lithium-sulfur battery, smaller pore sizes of the Aerographite network can be advantageous to improve the sulfur confinement in the cathode. For this purpose additional experiments with pre-compressed Aerographite will be carried out at the chair for Functional Nanomaterials. The Aerographite synthesis concept of sacrificial ZnO templates which can be edged away was already adopted by other research groups and employed for the fabrication of lithium-sulfur batteries with exceptional cyclic stability [113].

In future work, the elastic model will be optimized in conjunction with Prof. Nicola Pugno from the university of Trento. In this collaboration the bending induced curvature of the tetrapod arms, the non-linear rotational rigidity of the junctions and the densification induced stiffening will be included in the elastic model. In

order to validate the proposed model for the visco-elasticity of Aerographite, more cyclic deformation experiments at elevated temperatures will be conducted to study the temperature dependence.

The range of available template morphologies will be extended by the flame transport synthesis of tin oxide and other metal oxides. Preliminary experiments with sacrificial tin oxide networks already proved their applicability as template material. Further, Aerographite itself can be utilized as template material for the growth of 3D semiconductor networks. One example for the free growth of gallium nitride nano- and micro crystals on the surface of Aerographite is presented in the appendix.

Bibliography

1. A. K. Geim und K. S. Novoselov, *Nature materials* 6(3), **2007**, 183–191
2. S. Iijima et al., *nature* 354(6348), **1991**, 56–58
3. S. Iijima und T. Ichihashi **1993**
4. S. F. Braga, V. R. Coluci, S. B. Legoas, R. Giro, D. S. Galvão und R. H. Baughman, *Nano Letters* 4(5), **2004**, 881–884
5. X. Xie, L. Ju, X. Feng, Y. Sun, R. Zhou, K. Liu, S. Fan, Q. Li und K. Jiang, *Nano letters* 9(7), **2009**, 2565–2570
6. H. W. Kroto, J. R. Heath, S. C. O'Brien, R. F. Curl und R. E. Smalley, *Nature* 318(6042), **1985**, 162–163
7. R. Pekala, J. Farmer, C. Alviso, T. Tran, S. Mayer, J. Miller und B. Dunn, *Journal of non-crystalline solids* 225, **1998**, 74–80
8. A. Rode, E. Gamaly und B. Luther-Davies, *Applied Physics A* 70(2), **2000**, 135–144
9. R. Saito, G. Dresselhaus, M. S. Dresselhaus et al., *Physical properties of carbon nanotubes*, Bd. 4, World Scientific, **1998**
10. K. S. Novoselov, A. K. Geim, S. Morozov, D. Jiang, Y. Zhang, S. Dubonos, I. Grigorieva und A. Firsov, *science* 306(5696), **2004**, 666–669
11. K. Novoselov, D. Jiang, F. Schedin, T. Booth, V. Khotkevich, S. Morozov und A. Geim, *Proceedings of the National Academy of Sciences of the United States of America* 102(30), **2005**, 10451–10453
12. M.-F. Yu, O. Lourie, M. J. Dyer, K. Moloni, T. F. Kelly und R. S. Ruoff, *Science* 287(5453), **2000**, 637–640
13. M. Treacy, T. Ebbesen und J. Gibson **1996**
14. A. Krishnan, E. Dujardin, T. Ebbesen, P. Yianilos und M. Treacy, *Physical Review B* 58(20), **1998**, 14013
15. N. Yao und V. Lordi, *Journal of Applied Physics* 84(4), **1998**, 1939–1943
16. F. Li, H. Cheng, S. Bai, G. Su und M. Dresselhaus, *Applied physics letters* 77(20), **2000**, 3161–3163

17. N. M. Pugno, *Journal of Physics: Condensed Matter* 18(33), **2006**, S1971
18. N. M. Pugno, *Acta Materialia* 55(15), **2007**, 5269–5279
19. N. M. Pugno, F. Bosia und A. Carpenteri, *Small* 4(8), **2008**, 1044–1052
20. J.-H. Chen, C. Jang, S. Xiao, M. Ishigami und M. S. Fuhrer, *Nature nanotechnology* 3(4), **2008**, 206–209
21. J. Zou, J. Liu, A. S. Karakoti, A. Kumar, D. Joung, Q. Li, S. I. Khondaker, S. Seal und L. Zhai, *Acs Nano* 4(12), **2010**, 7293–7302
22. X. Zhang, Z. Sui, B. Xu, S. Yue, Y. Luo, W. Zhan und B. Liu, *Journal of Materials Chemistry* 21(18), **2011**, 6494–6497
23. X. Zhang, J. Liu, B. Xu, Y. Su und Y. Luo, *Carbon* 49(6), **2011**, 1884–1893
24. Z. Han, Z. Tang, P. Li, G. Yang, Q. Zheng und J. Yang, *Nanoscale* 5(12), **2013**, 5462–5467
25. H. Hu, Z. Zhao, W. Wan, Y. Gogotsi und J. Qiu, *Advanced materials* 25(15), **2013**, 2219–2223
26. H. Sun, Z. Xu und C. Gao, *Advanced Materials* 25(18), **2013**, 2554–2560
27. S. Vinod, C. S. Tiwary, P. A. da Silva Autreto, J. Taha-Tijerina, S. Ozden, A. C. Chipara, R. Vajtai, D. S. Galvao, T. N. Narayanan und P. M. Ajayan, *Nature Communications* 5, **2014**
28. M. Matsumoto, S. Saito und I. Ohmine, *Nature* 416(6879), **2002**, 409–413
29. Z. Chen, W. Ren, L. Gao, B. Liu, S. Pei und H.-M. Cheng, *Nature materials* 10(6), **2011**, 424–428
30. R. Wang, Y. Hao, Z. Wang, H. Gong und J. T. Thong, *Nano letters* 10(12), **2010**, 4844–4850
31. M. Mecklenburg, A. Schuchardt, Y. K. Mishra, S. Kaps, R. Adelung, A. Lotnyk, L. Kienle und K. Schulte, *Advanced Materials* 24(26), **2012**, 3437–3437
32. Y. K. Mishra, S. Kaps, A. Schuchardt, I. Paulowicz, X. Jin, D. Gedamu, S. Freitag, M. Claus, S. Wille, A. Kovalev et al., *Particle & Particle Systems Characterization* 30(9), **2013**, 775–783
33. Y. K. Mishra, S. Kaps, A. Schuchardt, I. Paulowicz, X. Jin, D. Gedamu, S. Wille, O. Lupan und R. Adelung, *KONA Powder and Particle Journal* 31(0), **2014**, 92–110
34. D. Chung, *Journal of materials science* 37(8), **2002**, 1475–1489

35. R. Sengupta, M. Bhattacharya, S. Bandyopadhyay und A. K. Bhowmick, *Progress in Polymer Science* **36**(5), **2011**, 638–670
36. A. W. Hull, *Physical Review* **10**(6), **1917**, 661
37. J. Bernal, *Proceedings of the Royal Society of London. Series A, Containing Papers of a Mathematical and Physical Character* **1924**, 749–773
38. H. Lipson und A. Stokes, *Proceedings of the Royal Society of London. Series A, Mathematical and Physical Sciences* **1942**, 101–105
39. H. Lipson und A. Stokes, *Nature* **149**, **1942**, 328
40. L. Pauling, *Proceedings of the National Academy of Sciences of the United States of America* **56**(6), **1966**, 1646
41. W. Toy, M. Dresselhaus und G. Dresselhaus, *Physical Review B* **15**(8), **1977**, 4077
42. J. Slonczewski und P. Weiss, *Physical Review* **109**(2), **1958**, 272
43. J. McClure, *Physical Review* **108**(3), **1957**, 612
44. G. Jenkins, K. Kawamura und L. Ban, *Proceedings of the Royal Society of London. Series A, Mathematical and Physical Sciences* **1972**, 501–517
45. G. M. Jenkins und K. Kawamura, *Polymeric carbons–carbon fibre, glass and char*, Cambridge University Press, **1976**
46. E. Fitzer, K.-H. Kochling, H. Boehm und H. Marsh, *Pure and Applied Chemistry* **67**(3), **1995**, 473–506
47. G. Jenkins und K. Kawamura, *Nature* **231**, **1971**, 175–176
48. P. J. Harris, *Critical Reviews in Solid State and Materials Sciences* **30**(4), **2005**, 235–253
49. Ü. Özgür, Y. I. Alivov, C. Liu, A. Teke, M. Reshchikov, S. Doğan, V. Avrutin, S.-J. Cho und H. Morkoc, *Journal of applied physics* **98**(4), **2005**, 041301
50. C. F. Klingshirn, A. Waag, A. Hoffmann und J. Geurts, *Zinc Oxide: From Fundamental Properties Towards Novel Applications*, Bd. 120, Springer, **2010**
51. M. Shiojiri und C. Kaito, *Journal of Crystal Growth* **52**, **1981**, 173–177
52. K. Nishio, T. Isshiki, M. Kitano und M. Shiojiri, *Philosophical Magazine A* **76**(4), **1997**, 889–904

53. H. Iwanaga, M. Fujii und S. Takeuchi, *Journal of crystal growth* **134**(3), **1993**, 275–280
54. C. Ronning, N. Shang, I. Gerhards, H. Hofsäss und M. Seibt, *Journal of applied physics* **98**(3), **2005**, 034307
55. M. Ashby, *Materials Selection in Mechanical Design*, 2000, ISBN 0 7506 4357 9, Cambridge University Press, Cambridge, **1992**
56. “Young´s Modulus - Density selection map from Cambridge University Homepage”, http://www.doitpoms.ac.uk/tplib/optimisation-biomaterials/modulus_density.php
57. T. Porter, *Wood: identification & use*, Guild of Master Craftsman Pubns ltd, **2007**
58. T. Schaedler, A. Jacobsen, A. Torrents, A. Sorensen, J. Lian, J. Greer, L. Valdevit und W. Carter, *Science* **334**(6058), **2011**, 962–965
59. L. J. Gibson und M. F. Ashby, *Cellular solids: structure and properties*, Cambridge university press, **1999**
60. U. Wegst und M. Ashby, *Philosophical Magazine* **84**(21), **2004**, 2167–2186
61. J. C. Maxwell, *The London, Edinburgh, and Dublin Philosophical Magazine and Journal of Science* **27**(182), **1864**, 294–299
62. V. Deshpande, M. Ashby und N. Fleck, *Acta Materialia* **49**(6), **2001**, 1035–1040
63. C. Calladine, *International Journal of Solids and Structures* **14**(2), **1978**, 161–172
64. M. F. Ashby und R. M. Medalist, *Metallurgical Transactions A* **14**(9), **1983**, 1755–1769
65. R. S. Lakes, *Viscoelastic solids*, Bd. 9, CRC press, **1998**
66. M. S. Blanter, I. S. Golovin, H. Neuhäuser und H.-R. Sinning, *Internal friction in metallic materials: a handbook*, Bd. 90, Springer, **2007**
67. M. T. Shaw und W. J. MacKnight, *Introduction to polymer viscoelasticity*, John Wiley & Sons, **2005**
68. R. Christensen, *Theory of viscoelasticity: an introduction*, Elsevier, **1982**
69. W. Flügge, *Viscoelasticity*, Springer, **1967**

70. J. D. Waals, *Over de continuiteit van den gas-en vloeistoftoestand*, Dissertation, **1873**
71. F. London, *Trans. Faraday Soc.* **33**, **1937**, 8b–26
72. H. Hamaker, *physica* **4**(10), **1937**, 1058–1072
73. G. Feinberg und J. Sucher, *Physical Review A* **2**(6), **1970**, 2395
74. I. E. Dzyaloshinskii, E. Lifshitz und L. P. Pitaevskii, *Physics-Uspekhi* **4**(2), **1961**, 153–176
75. V. A. Parsegian, *Van der Waals forces*, Cambridge univ. press Cambridge etc., **2006**
76. A. Dalgarno und A. Kingston, *Proceedings of the Physical Society* **73**(3), **1959**, 455
77. R. Winterton, *Contemporary Physics* **11**(6), **1970**, 559–574
78. H. v. Helmholtz, *Annalen der Physik* **165**(6), **1853**, 211–233
79. V. V. Obreja, *Physica E: Low-dimensional Systems and Nanostructures* **40**(7), **2008**, 2596–2605
80. Y. Zhang, H. Feng, X. Wu, L. Wang, A. Zhang, T. Xia, H. Dong, X. Li und L. Zhang, *International journal of hydrogen energy* **34**(11), **2009**, 4889–4899
81. P. Sharma und T. Bhatti, *Energy Conversion and Management* **51**(12), **2010**, 2901–2912
82. W. Sugimoto, H. Iwata, Y. Murakami und Y. Takasu, *Journal of the Electrochemical Society* **151**(8), **2004**, A1181–A1187
83. S. S. Zhang, *Journal of Power Sources* **231**, **2013**, 153–162
84. Y. Diao, K. Xie, S. Xiong und X. Hong, *Journal of Power Sources* **235**, **2013**, 181–186
85. A. Manthiram, Y. Fu und Y.-S. Su, *Accounts of chemical research* **46**(5), **2012**, 1125–1134
86. H. Wang, Y. Yang, Y. Liang, J. T. Robinson, Y. Li, A. Jackson, Y. Cui und H. Dai, *Nano letters* **11**(7), **2011**, 2644–2647
87. M. Mecklenburg, "Ultra-hoch gefüllte orientierte CNT- und 3D-vernetzte Aerographit/Epoxyd Komposite: Synthese, Herstellung und Eigenschaften", Dissertation, Technical University of Hamburg-Harburg, **2015**

88. H. Iwanaga, M. Fujii und S. Takeuchi, *Journal of crystal growth* 183(1), **1998**, 190–195
89. I. Paulowicz, "Synthese, Charakterisierung und Anwendungen nanostrukturiertes 3D ZnO Netzwerke", Dissertation, University of Kiel, **2015**
90. D. Phokharatkul, A. Wisitsoraat, T. Lomas und A. Tuantranont, *Carbon* **2014**
91. K. Xu, *Chemical reviews* 104(10), **2004**, 4303–4418
92. M. Terrones, F. Banhart, N. Grobert, J.-C. Charlier, H. Terrones und P. Ajayan, *Physical review letters* 89(7), **2002**, 075505
93. L. L. Aranda, *Potentials, IEEE* 20(2), **2001**, 12–15
94. B. Warren, *The Journal of Chemical Physics* 2(9), **1934**, 551–555
95. R. E. Franklin, *Acta crystallographica* 4(3), **1951**, 253–261
96. R. E. Franklin, *Proceedings of the Royal Society of London. Series A. Mathematical and Physical Sciences* 209(1097), **1951**, 196–218
97. "Online data base for EELS spectra, Inner & Outer Shell Excitation Spectrum Repository", <http://pc-web.cemes.fr/eelsdb/index.php?page=home.php>
98. R. F. Egerton, *Electron energy-loss spectroscopy in the electron microscope*, Bd. 233, Springer, **1996**
99. L. Brazier, *Proceedings of the Royal Society of London. Series A* 116(773), **1927**, 104–114
100. M. Biancolini und C. Brutti, *Packaging Technology and Science* 16(2), **2003**, 47–60
101. M. Biancolini, *Composite structures* 69(3), **2005**, 322–328
102. Q. Zhang, Y. Lu, F. Du, L. Dai, J. Baur und D. Foster, *Journal of Physics D: Applied Physics* 43(31), **2010**, 315401
103. W. D. Hanna, D. J. Chang und G. L. Steckel, *NASA* (19980193166), **1998**
104. M. Falvo, G. Clary, R. Taylor, V. Chi, F. Brooks, S. Washburn und R. Superfine, *Nature* 389(6651), **1997**, 582–584
105. H. Marsh und F. Rodríguez-Reinoso, *Sciences of carbon materials*, Universidad de Alicante Alicante, **2000**

106. M. Pollak und B. Shklovskii, *Hopping transport in solids*, Elsevier, **1991**
107. G. Eda, C. Mattevi, H. Yamaguchi, H. Kim und M. Chhowalla, *The Journal of Physical Chemistry C* **113**(35), **2009**, 15768–15771
108. A. B. Kaiser, C. Gómez-Navarro, R. S. Sundaram, M. Burghard und K. Kern, *Nano letters* **9**(5), **2009**, 1787–1792
109. C. Mattevi, G. Eda, S. Agnoli, S. Miller, K. A. Mkhoyan, O. Celik, D. Mastrogiovanni, G. Granozzi, E. Garfunkel und M. Chhowalla, *Advanced Functional Materials* **19**(16), **2009**, 2577–2583
110. I. Jung, D. A. Dikin, R. D. Piner und R. S. Ruoff, *Nano Letters* **8**(12), **2008**, 4283–4287
111. B. H. Jeon, J. H. Yeon, K. M. Kim und I. J. Chung, *Journal of power sources* **109**(1), **2002**, 89–97
112. J. Shim, K. A. Striebel und E. J. Cairns, *Journal of the Electrochemical Society* **149**(10), **2002**, A1321–A1325
113. P. Strubel, S. Thieme, T. Biemelt, A. Helmer, M. Oschatz, J. Brückner, H. Althues und S. Kaskel, *Advanced Functional Materials* **2014**

Danksagung

An erster stelle möchte ich Prof. Dr. Rainer Adelung für die Möglichkeit danken, die Doktorarbeit in der Arbeitsgruppe für funktionale Nanomaterialien zu schreiben und an einem so spannenden Thema wie Aerographite forschen zu können. Besonders will ich mich auch für die vielen hilfreichen wissenschaftlichen Diskussionen bedanken, die wir während meines Studiums, der Bachelorarbeit, der Masterarbeit sowie der Promotion hatten und auch sicher in Zukunft noch haben werden.

Außerordentlicher Dank gebührt Sören Kaps, der mich während der gesamten Promotionszeit unterstützt hat und mir immer uneingeschränkt bei allen wissenschaftlichen Fragen geholfen hat. Einen wesentlichen Beitrag zu dieser Doktorarbeit hat auch Reimonds Meija von der Universität in Riga geleistet. Durch seine Hilfe und die Hilfe von Prof. Dr. Donats Erts wurden die *in situ* Messungen am Aerographite möglich und dafür möchte ich beiden außerordentlich danken.

Matthias Mecklenburg und Prof. Dr. Karl Schulte von der TUHH möchte ich für die gesamte Kooperation zum Thema Aerographite danken. Ohne diese Zusammenarbeit wäre die Synthese und die Veröffentlichung von Aerographite nicht möglich gewesen. Für das Korrektur lesen dieser Arbeit und die vielen Verbesserungsvorschläge bedanke ich mich sehr herzlich bei Dr. Xin Jin, Dr. Yogendra Kumar Mishra und Dr. Viktor Hrkac.

Für seinen Wissenschaftlichen Rat und die Diskussionen zur Viskoelastizität möchte ich vor allem auch Prof. Dr. Franz Faupel danken.

Prof. Dr. Nicola Pugno und Stefano Signetti möchte ich sehr für die Überprüfung des elastischen Modells und ihre Simulationen danken. Dr. Stephan Rautenberg hat durch sein großartiges Fachwissen die Programmierung des Mechanikmessstandes in LabView ermöglicht und damit einen großen Beitrag zu dieser Arbeit geleistet. Auch Sandra Nöhren und Dr. Enrique Quiroga Gonzalez möchte ich meinen besonderen Dank aussprechen für Ihre Hilfe bei den Batterie experimenten. Für die TEM Untersuchungen am Aerographite bedanke ich mich sehr bei Mao Deng, Dr. Andriy Lotnyk, Christin Szillus, Prof. Dr. Lorenz Kienle und dem gesamten Lehrstuhl für Synthese und Realstruktur.

Jorit Gröttrup, Daria Smazna und Sebastian Zabel haben mir riesig bei der Betreuung der Festkörperphysik Übungen geholfen. Für technische Unterstützung in

allen Belangen möchte ich sehr Christoph Ochmann, Stefan Rehders, Jörg Bahr, Dr. Jürgen Carstensen, Dr. George Popkirov, Mathias Hoppe, Wolfgang Taute, Peter Sommer, Rainer Kloß, Berndt Neumann, Matthias Burmeister und der zentralen Werkstatt der TF danken. Großer Dank gebührt auch Beathe Minden und Kärtin Brandenburg für ihre zuverlässige Unterstützung.

Sehr herzlich möchte ich mich bei Dr. Vladimir Zaporojtchenko, Kerstin Meurisch, Amit Kulkarni, Tommi Hrkac, Tilo Peter und Björn Gojdka bedanken die mich schon während meiner HiWi Zeit begleitet haben.

Während meiner Zeit an der technischen Fakultät hat mich vor allem begeistert, mit was für super Menschen ich meine Zeit teilen durfte. Die letzten vier Jahre wären ohne Iris Hölkens, Helge Hölkens, Stefan Freitag, Patrick Hayes, Dr. Ulrich Schürmann, Leonard Siebert, Dr. Dawit Menale Gedamu, Tim Reimer, Fabian Schütt, Victor Kaidas, Eric Woltermann, Laith Kadim, Cai Müller, Grit Köppel und Bastian Martin sicher nicht so eine großartige Zeit gewesen. Nach neun Jahren des gemeinsamen Studiums und der Promotion an der Technischen Fakultät will ich vor allem noch meinen Freunden Tönjes Koschine, Christian Ohrt, Dr. Julia Reverey, Ingo Paulowicz, Bodo Henkel und Dr. Mark-Daniel Gerngross für die super Zeit danken. Nicht unerwähnt bleiben darf Steve Fry, der mich bei der Arbeit zum Aeromagneten unterstützt hat und durch vielfältige Ablenkung (z.B. kochende Säure) für mein Seelenwohl gesorgt hat.

Zum Abschluss, möchte ich mich meiner Familie danken. Ohne diesen Rückhalt und diese gigantische Unterstützung wäre ich jetzt nicht hier.

List of Publications

1. D. Gedamu, S. Jebril, **A. Schuchardt**, M. Elbahri, S. Wille, Y. K. Mishra, R. Adelung, Examples for the integration of self organized nanowires for functional devices by a fracture approach, **Physica Status Solidi B 247, 2571-2580, (2010)**.
2. M. Mecklenburg, **A. Schuchardt**, Y. K. Mishra, S. Kaps, R. Adelung, A. Lotnyk, L. Kienle, K. Schulte, Aerographite: Ultra lightweight flexible nanowall carbon microtube-material with outstanding mechanical performance, **Advanced Materials 24, 3486-3490, (2012)**.
3. Y. K. Mishra, S. Kaps, **A. Schuchardt**, I. Paulowicz, X. Jin, D. Gedamu, S. Freitag, S. Wille, M. Claus, A. Kovalev, S. N. Gorb, R. Adelung, Fabrication of macroscopically and highly porous 3D semiconductor networks from interpenetrating nanostructures by simple flame transport approach, **Particle and Particle Systems Characterization 30, 775-783 (2013)**.
4. Y. K. Mishra, S. Kaps, **A. Schuchardt**, I. Paulowicz, X. Jin, D. Gedamu, S. Freitag, S. Wille, O. Lupan, R. Adelung, Large scale fabrication of complex shaped metal oxide nano-microstructures and their interconnected networks for multifunctional applications, **KONA Powder and Part. Journal 31, 92-110, (2014)**.

Supervised Bachelor and Master Theses

This is a list of the Bachelor and Master thesis which have been supervised during the work for this thesis:

1. Characterization of Aerographite, Bachelor thesis, Andreas W. Fischer, (2011)
2. Characterization of Aerographite and its suitability as electrode material for double-layer capacitors, Alexander Omelcenko, (2011)
3. Characterization of mechanical properties of Aeroraphite, Bachelor thesis, Christian Skawianczyk, (2012)
4. Untersuchung des Einflusses der n-Dotierung mit Aluminium und der Glüh-temperatur auf elektrische Eigenschaften des durch die Batch-Methode hergestellten Zinkoxids, Bachelorarbeit, Olga Dudko, (2012)
5. Untersuchungen der elektrischen und elektrochemischen Eigenschaften von Aerographit in Hinblick auf eine mögliche Anwendung als Elektrode in einem Lithium-Ionen-Akkumulator, Bachelorarbeit, Stefan Schröder, (2012)
6. Multifunktionale Komposite aus organischen und anorganischen Funktionswerkstoffen auf Basis von Aerographit, Masterarbeit, Stefan Freitag, (2013)

Appendix

Experimental Equipment

- scanning electron microscope at CAU: Zeiss Ultra Plus, Oxford X-act EDX detector
- scanning electron microscope at TUHH: Zeiss Supra 55
- scanning electron microscope at TUHH: Leo Gemini 1530
- scanning electron microscope at University of Latvia: Hitachi S-4800
- nano-manipulators: SmarAct SLC-1720 driven by SmarAct HCU-3DM control unit.
- atomic force microscopy cantilevers: Olympus BL-RC-150VB
- sub-femtoamp sourcemeter: Keithley 6430
- micro manipulator: Maerzhaeuser Wetzlar HS 6.3 driven by Tango PCI-Card
- precision balance: Kern PLE 310-3N
- source-meter: Keithley 6400
- muffle furnace: Nabertherm LE 2/11
- muffle furnace: Nabertherm L 3/12
- ceramic tubes: Friatec Degussit AL23
- digital oscilloscope: Agilent DSO1002A
- potentiostat: Etch and Technology Elypor 01

Additional Figures

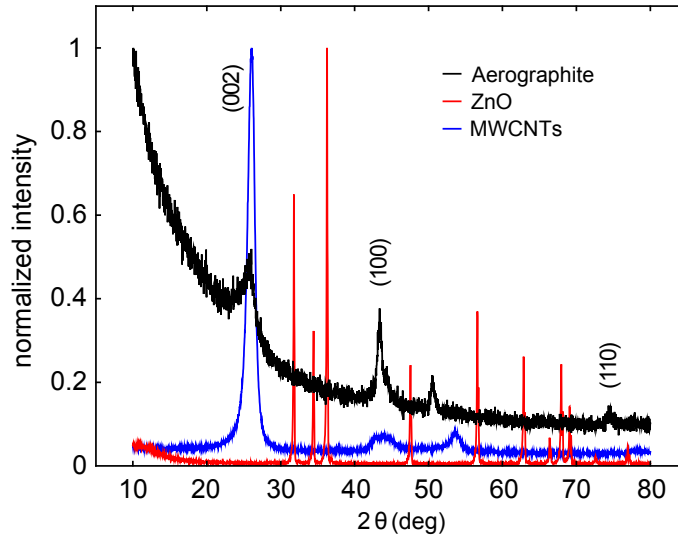


Figure 13.3: X-ray diffraction of Aerographite, ZnO template material and multiwalled carbon nanotubes (MWCNTs).

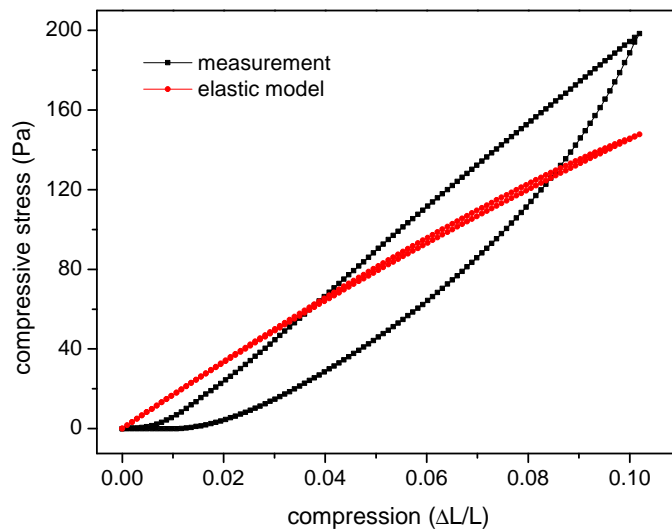


Figure 13.4: Compression measurements at a bulk Aerographite network with a density of 3.8 mg/cm^3 . Elastic model with an initial angle $\alpha_0 = 45^\circ$, spring constant $D = 2 \text{ pNm/rad}$, tetrapod interleaving factor $n = 3$, effective tetrapod arm length $|\vec{r}| = 15 \mu\text{m}$.

Growth of Gallium Nitride Nano- and Microstructures on Aerographite Networks by Hydride Vapor Phase Epitaxy

The as grown Aerographite networks have been utilized as templates for the growth of GaN nano- and microstructures in a hydride vapor phase epitaxy (HVPE) system with four temperature zone horizontal reaction chamber. Metallic gallium, ammonia (NH_3) gas, hydrogen chloride (HCl) gas and hydrogen (H_2) gas were employed as precursors. In the source zone, GaCl was formed as a result of the chemical reactions between the gaseous HCl and the liquid Ga at 850°C . The GaCl and NH_3 gas reacted with each other in the react zone at a temperature of 600°C for 10 min and initiated the nucleation of GaN on the surface of graphite. Subsequently the temperature was increased to 950°C for another 10 min, to produce GaN nano/micro-crystallites. In the process of the GaN growth, the HCl , NH_3 and H_2 flow rates were equal to 15 sml/min , 500 sml/min and 3600 sml/min , respectively. Figure 13.5 presents an overview of the GaN nano- and microstructures attached to the Aerographite template.

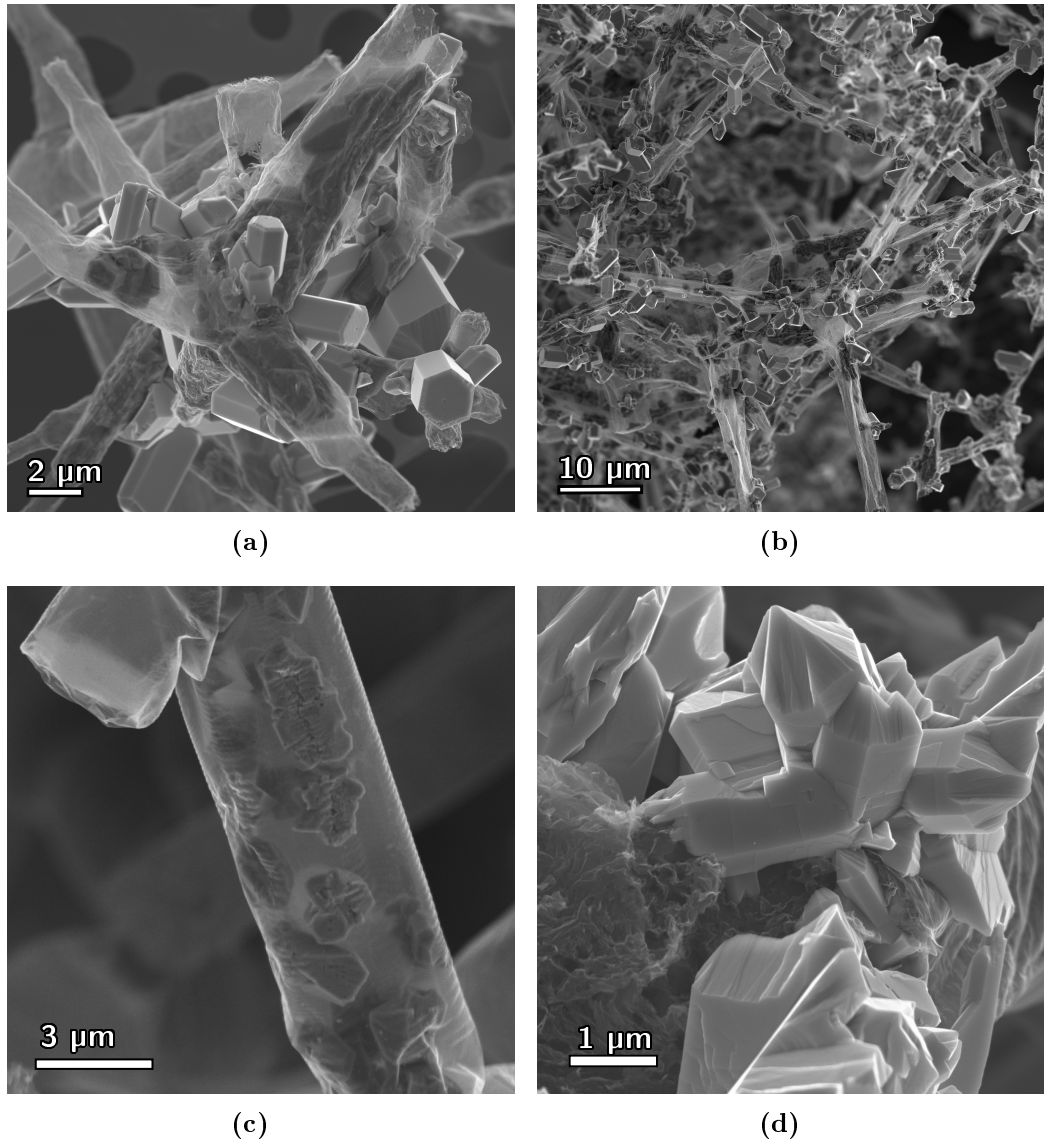


Figure 13.5: SEM images of an Aerographite network, loaded with hexagonal crystals of wurtzite type gallium nitride. a) Close up of an Aerographite tetrapod with GaN nano- and microstructures, grown on the inner and outer surfaces of the tetrapod. b) Overview of an network of Aerographite loaded with a high surface density of GaN crystalss. c) Magnified view on a hollow tube of Aerographite with pronounced growth of GaN crystals on the inner surface. d) Transition region between hexagonal GaN crystals and the underlying Aerographite substrate.

LabView Documentation of Mechanical Test Setup

Figure 13.6 shows a screenshot of the front panel and the block diagram of the LabView program which was developed for the mechanical test setup. This program allows the automated cyclic deformation of the Aerographite samples and the simultaneous measurement of the electrical conductivity.

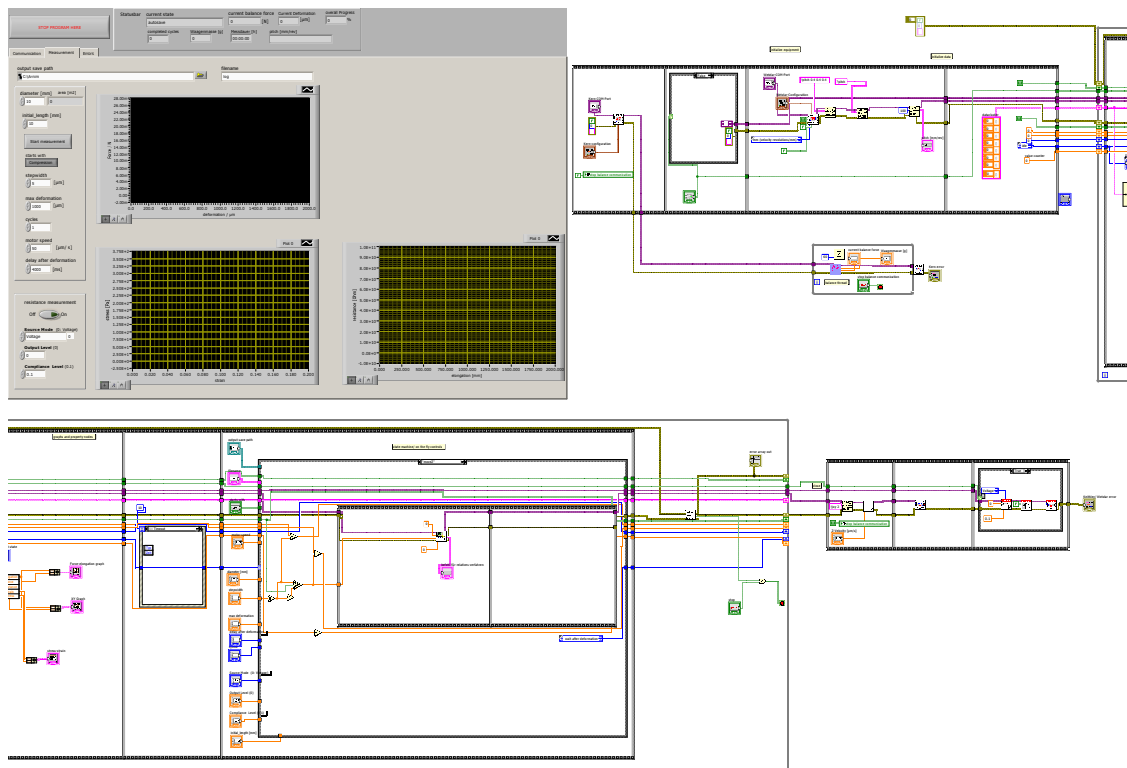


Figure 13.6

Eidesstattliche Erklärung

Ich erkläre, dass ich meine Dissertation "On the Mechanical Modeling, Visco-Elasticity and Application of Aerographite, a 3D Carbon Nano-Material" selbstständig und ohne Benutzung anderer als der angegebenen Hilfsmittel angefertigt habe und dass ich alle Stellen, die ich wörtlich oder sinngemäß aus Veröffentlichungen entnommen habe, als solche kenntlich gemacht habe. Die Arbeit hat bisher in gleicher oder ähnlicher Form oder auszugsweise noch keiner Prüfungsbehörde vorgelegen und entstand unter Einhaltung der Regeln guter wissenschaftlicher Praxis der Deutschen Forschungsgemeinschaft.